# Optical Fiber Sensors for Liquid Refractive Index and Evaporation Dynamics


Mário Rúben Lousada Alves
Master in Engineering Physics
Department of Physics and Astronomy
Faculty of Sciences of University of Porto and
Faculty of Engineering of University of Porto

2025

# Optical Fiber Sensors for Liquid Refractive Index and Evaporation Dynamics

Mário Rúben Lousada Alves
Dissertation carried out as part of the Master in Engineering Physics
Department of Physics and Astronomy
2025

**Supervisor**
Dra. Susana Novais, Assistant Researcher, INESC TEC

**Co-supervisor**
Dra. Susana Silva, Assistant Researcher, INESC TEC

INESCTEC
TECHNOLOGY & SCIENCE
ASSOCIATE LABORATORY
PORTUGAL

“Caminhante, não há caminho. Faz-se caminho ao andar.”

António Machado

"I can accept failure. Everyone fails at something. But I can't accept not trying."

Michael Jordan

# Acknowledgements

First and foremost, I would like to express my sincere gratitude to my supervisors: Orlando Frazão, Susana Silva, and Susana Novais, for their continuous support, guidance, and encouragement throughout this work. Their willingness to help, combined with a warm and friendly relationship, made this journey much more rewarding.

I would also like to thank my laboratory colleagues and friends: Vinícius Piaia, Ana Teixeira, Paulo Robalinho, and Beatriz Soares. With them, I shared not only meaningful work but also engaging conversations and plenty of laughter.

My appreciation goes to CAP and all its students and associates for warmly welcoming me into their community and making me feel at home.

On a more personal note, I am deeply thankful to my cherished faculty friends for the unforgettable moments and the incredible time we spent together over the past five years.

I am especially grateful to my close family for their unwavering support. Finally, I would like to thank my mother, who has always been a role model in life and character, and my father, whose support has been a constant presence throughout my academic journey and beyond.

# Resumo

Este trabalho reúne quatro linhas de investigação complementares no domínio da fotónica e dos sensores. São apresentados estudos refratométricos com diferentes configurações de cabeças sensoras, incluindo fibras monomodo, multimodo, microestruturadas e redes de Bragg, explorando aplicações específicas em função da precisão e da gama de índices de refração. Em paralelo, analisam-se fenómenos de evaporação através da comparação de desempenhos de várias fibras, avaliando parâmetros como profundidade inicial, velocidade de retirada e dinâmica em líquidos distintos. O estudo inclui ainda simulações de propagação em fibras microestruturadas de núcleo retangular, com otimização estrutural orientada para aplicações refratométricas. Por fim, investiga-se uma rede de Bragg cortada, cujo espetro de reflexão se aproxima ao efeito Fano, destacando-se o seu potencial como dispositivo de deteção de variações de temperatura, índice de refração e processos de evaporação.

Palavras-chave: [Índice de refração, dinâmica de evaporação, fibra microestruturada, rede de Bragg em fibra ótica, fibra multimode, fibra monomodo]

# Abstract

This work brings together four complementary lines of investigation in the field of photonics and sensors. Refractometric studies are presented using different sensor head configurations, including single-mode fibers, step-index and graded-index multimode fibers, microstructured fibers, and Bragg gratings, exploring specific applications according to the required precision and the range of refractive indices considered. In parallel, evaporation phenomena are analyzed through the performance comparison of various fibers, assessing parameters such as initial depth, withdrawal speed, and dynamics in different liquids. The study also includes simulations of propagation modes in microstructured fibers with rectangular cores, accompanied by structural optimization aimed at refractometric applications. Finally, a cut Bragg grating is investigated, whose reflection spectrum resembles the Fano effect, highlighting its potential as a device for detecting variations in temperature, refractive index, and evaporation processes.

Keywords: [Refractive Index, Evaporation dynamics, microstructured fiber, fiber Bragg grating, multimode fiber, monomode fiber]

# Table of Contents

# List of Tables

# List of Figures

# List of Abbreviations

| | |
|---|---|
| **FBG** | FIBER BRAGG GRATING |
| **FEM** | FINITE ELEMENT METHOD |
| **FFT** | FAST FOURIER TRANSFORM |
| **FFPI** | FIBER FABRY-PÉROT INTERFEROMETER |
| **HCF** | HOLLOW CORE FIBER |
| **IPA** | ISOPROPYL ALCOHOL |
| **MMF** | MULTI-MODE FIBER |
| **NA** | NUMERICAL APERTURE |
| **OFS** | OPTICAL FIBER SENSOR |
| **OSA** | OPTICAL SPECTRUM ANALYZER |
| **PLT** | PELTIER COOLER |
| **RI** | REFRACTIVE INDEX |
| **SCF** | SOLID CORE FIBER |
| **SFBG** | SLICED FIBER BRAGG GRATING |
| **SMF** | SINGLE-MODE FIBER |
| **TIR** | TOTAL INTERNAL REFLECTION |
| **OPM** | OPTICAL POWER METER |

# 1. Introduction

## 1.1. Motivation

Optical Fiber Sensor (OFS) have attracted increasing attention from both scientists and engineers in recent years, as they enable measurements that would be difficult or even impossible to achieve with conventional sensors. In practical applications, optical and traditional sensors are often used in combination, thereby leveraging the strengths of each technology [1].

Over the past few decades, optical sensors have evolved to the point where they can be applied to a wide range of measurements, including acoustics, vibration, electric and magnetic fields, acceleration, rotation, temperature, pressure, linear and angular position, strain, humidity, viscosity, chemical analysis, and many other sensing applications [1]. Nonetheless, these sensors still require considerable advancement, as they are currently more costly and less well-known to end users compared to conventional detection methods [2].

Optical sensors are widely appreciated in medicine and biochemistry for their exceptional ability to measure refractive index (RI) changes. Events such as DNA hybridization, antibody–antigen interactions, chemical reactions, and shifts in concentration alter the RI of the surrounding medium that are crucial for accurate biomarker detection [3–5].

While the RI is a key property of a medium, it alone does not provide a complete picture, therefore, complementary optical fiber-based techniques, such as absorption and Raman spectroscopy, are often employed to achieve more comprehensive material characterization [6,7]. Moreover, fiber-tip configurations have facilitated the investigation of droplet evaporation dynamics, a process relevant to various domains, including the assessment of fuel combustion efficiency [8], inkjet-printing [9,10], DNA microarray fabrication [11], disease transmission [12] and microfluids [13] among others [14].

## 1.2. Objectives

This work has three main objectives. The first objective is to examine existing refractometric sensors and evaluate their capabilities across different RI ranges, identifying which performs best. The second objective is to make the evaporation study of a liquid droplet identifying the best sensor for the purpose and how to optimize the process. The third objective is to project and study new fiber sensors that should provide better measurement capabilities for one or two of the physical parameters measured.

## 1.3. Dissertation structure

This dissertation is divided into different chapters, each with a given objective:

- **Chapter 1** outlines the motivations and objectives underlying the present work, provides a chapter-by-chapter summary, and highlights the contributions achieved.
- **Chapter 2** introduces the fundamental theory of optical fibers and sensors in general, with particular emphasis on optical fiber sensors and fiber-tip-sensors. It's also reviewed the current state-of-the-art in fiber-tip sensors for RI measurements.
- **Chapter 3** presents the study of refractometric sensors, including the calculation of sensitivities and the application of various methods for data acquisition and analysis. The sensors investigated comprise single mode fiber, step index multimode fiber, graded-index multimode fiber, solid-core microstructured fiber, and a fiber-tip Bragg grating.
- **Chapter 4** focuses on evaporation study, identifying the most suitable sensor. among single mode fiber, step-index multimode fiber and solid-core microstructured fiber, tested with water and isopropyl alcohol. A comprehensive analysis of evaporation dynamics for both solutions is provided, along with an assessment of factors influencing variations in the evaporation process.
- **Chapter 5** reports on modal simulations of a novel large-area solid-core photonic crystal fiber.
- **Chapter 6** investigates the newly proposed Fano-like Bragg sensor, exploring its potential applications as a temperature sensor, a refractive index sensor, and, finally, an evaporation sensor.
- **Chapter 7** presents the overall conclusions of the work, together with recommendations for future research in this area.

## 1.4. Scientific outputs

- M. R. Alves, S. Silva, and O. Frazão, "Modelling and Simulation of a Rectangular Large Mode Area Photonic Crystal Fiber," EOS Annual Meeting (EOSAM 2025), Delft, The Netherlands, 2025 – **Poster presentation.**
- V. Piaia, M. R. Alves, P.Robalinho, S.Silva and O. Frazão, "Fano Resonance of Sliced Fiber Bragg Grating for Liquid Sensing" **- under review in IEEE Journal of Lightwave Technology**.

# 2. Literature review

## 2.1. Historical context

The history of optical fibers may begin with Euclid, circa 300 BC, who made the first documented study of light [15]. At the end of the 13th century, Al-Farisi and Theodoric of Freiberg, independently, explained the appearance of rainbows because of total internal reflection of light within the water droplets in the atmosphere [16,17]. After this point several improvements on light theory were made, with the important mark from Snellius (creator of Snell's law), until in 1842, Colladon and Babinet published the results of a "lighted laminar water fountain" [18,19].

Years later, in 1854, John Tyndall explained optical wave guiding by a ray-tracing approach [20].

The mastery of total internal reflection, intrigued scientist and engineers to explore its potential; William Wheeling patented "light pipping" for illumination; Roth and Reuss, medical doctors, in 1880, employ bent glass rods to illuminate body cavities; as a communication channel, in 1933, first television signals were optically transmitted over glass rod [21,22].

In 1962, Elias Snitzer fabricates a single mode fiber and 4 years later, Charles Kao and George Hockam published an article with the purpose of implying impurities are the main cause of optical loss and proposed a theorized glass capable of transmission losses below 20dB/Km, 4 years later it was made on practice [32-36]. After this breakthrough there was a boom, with great investments on the improvement of optic fibers and its usages: first diode end-pumped fiber laser (1973), wave mixing in optical fibers (1974), first telephone call using optical fibers in Long Beach California (1977), the appearing of single polarization optical fibers and Bragg gratings (1978), first transatlantic telephone cable goes into operation(1988), appearance of the first photonic band gap fiber(1995), first photonic crystal fiber (1996), first photonic crystal optical fiber-based supercontinuum generation (2000) and optical fiber laser exceeds an output power of 30 KW [22,33].

Throughout history, optical fibers have continued to evolve, so its usages, as of today optical fibers are used in various applications including communications, medicine, energy, manufacturing and tools for scientific inquiry [34].

This chapter is divided into two sections. The first provides an overview of optical fibers, highlighting their various architectures and distinguishing features. The second focuses on optical fiber sensors, discussing their different designs and operating principles.

## 2.2. Optical fibers

An optical fiber is a cylindrical waveguide primarily designed to confine electromagnetic energy in the form of light and guide it along its axis [35]. Optical fibers have two main applications: telecommunications and sensing.

Optical fiber sensors (OFS) play a significant role, primarily in biomedical applications. This is due to several advantages, such as biocompatibility, chemical inertness, flexibility, and compactness, along with their ability to be machined and functionalized [36,37].

Further developments in photonics, chemistry, biology, and other fields have enabled the use of OFS in medicine, where their compactness and flexibility allow integration with medical catheters and needles. OFS are also being implemented in the oil and gas industry, as well as in environmental monitoring [38].

The most basic optical fibers are generally constituted by the core, cladding and a coating, as shown in Figure 2.1.

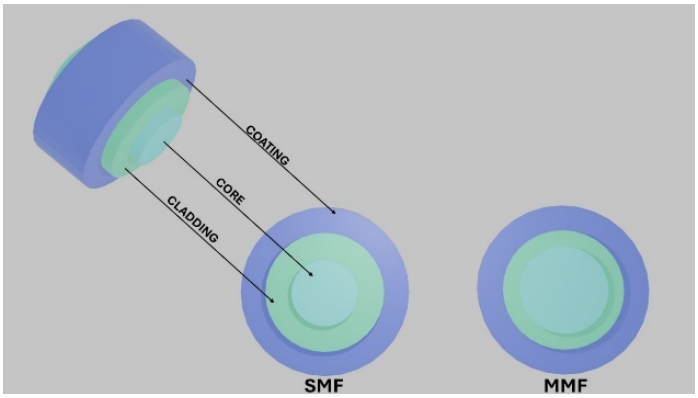


Figure 2.1: Schematic of the standard optical fiber structure, adapted from [39].

The fiber core consists of pure silica glass ($SiO_2$) doped with germanium to increase its refractive index, while the cladding is typically made of pure silica glass. This refractive index contrast enables light confinement within the core through Total Internal Reflection (TIR). The function of the cladding is not only to confine light within the core, but also to minimize dispersion losses arising from dielectric discontinuities at the core surface. In addition, it enhances the mechanical strength of the fiber and shields the core from external contaminants. To further improve its mechanical robustness, protective coating is applied [35].

TIR occurs when light travels from one medium with a higher refractive index to another with a lower refractive index, and the angle of incidence exceeds a certain critical value. In this case, all the light is reflected into the original medium. This phenomenon is explained and systematized by the Snell–Descartes law. Given a refractive index $n_1$ greater than $n_2$, it is possible to derive the critical angle $\theta_c$ by rearranging Snell's equation as follows [35]:

$$\theta_c = arcsin\left(\frac{n_2}{n_1}\right) \tag{2.1}$$

Given Equation (2.1), the minimum angle for TIR propagation inside the fiber is established. To ensure that the propagating rays satisfy the TIR condition, the concept of Numerical Aperture (NA) was introduced. This parameter defines the angular range, or acceptance cone, within which light rays can enter the fiber and still propagate through it via TIR, as illustrated in Figure 2.2. The NA is given by [35]:

$$NA = nsin\,(\theta) = \sqrt{n_c^2 - n_{cl}^2} \tag{2.2}$$

*n* represents the RI outside the fiber, $nc$ is the core's RI, $ncl$ is the cladding's RI, $\theta$ is the maximum acceptance angle.

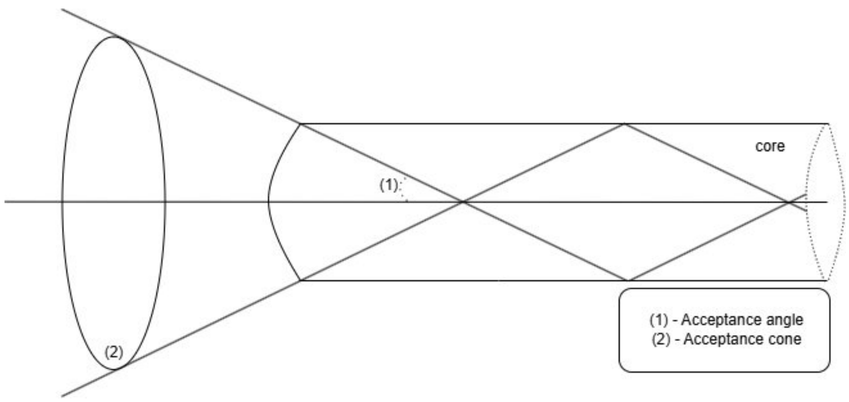


Figure 2.2: Schematic of the fiber core, acceptance angle and acceptance cone, adapted from [40].

From a ray optics perspective, as illustrated in Figure 2.2, light can be viewed as propagating along discrete ray paths, each traveling at a specific angle that satisfies the condition defined by Equation (1.1). Each individual angle corresponds to a distinct optical path. For every unique optical path, we define a mode. These modes differ in their propagation times despite having the same phase velocity, which leads to the association of different effective refractive indices with each mode. However, due to the limitations of the ray optics model, especially in describing interference and diffraction, it is often more accurate to adopt the wave optics perspective, in which Maxwell's equations are solved to obtain distinct solutions, i.e., modes. In this framework, modes are classified by order, which corresponds to the number of zeros (nodes) in the transverse electric field distribution. Lower-order modes are more tightly confined to the core region. A planar waveguide representation of these modal distributions is shown in Figure 2.3.

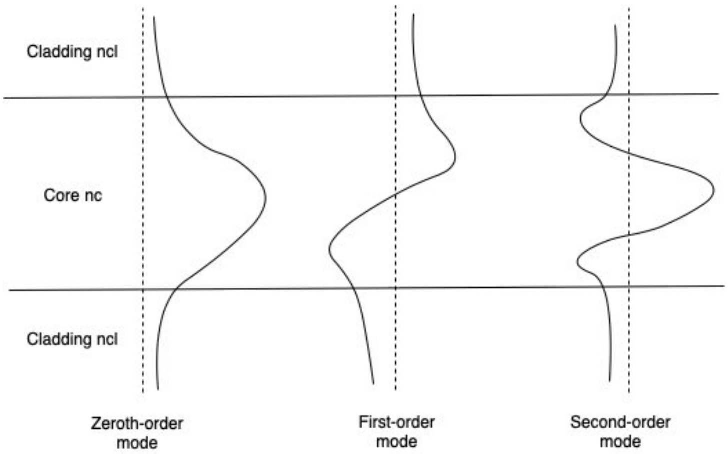


Figure 2.3: Lower order modes of a planar waveguide, adapted from [35].

The planar waveguide represents the simplest case for determining the modes of a waveguide. Despite its simplicity, it provides reasonably accurate results, since, when viewed transversally, the modal behavior in planar and cylindrical waveguides (such as optical fibers) is fundamentally similar. In the wave optics framework, modes are not strictly confined to the core. Instead, part of the electromagnetic field extends into the cladding, decaying exponentially. Within the core, the mode exhibits a harmonic variation of the field. It is possible to correlate the ray and wave optics perspectives: steeper propagation angles in the ray model correspond to higher-order modes in the wave model. Another key characteristic of a mode is its propagation constant, denoted by $\beta = nk$, where *n* is the effective refractive index and *k* is the wave number. For a mode to be considered guided, its propagation constant must satisfy the following condition [35]:

$$kn_{cl} < \beta < kn_c \tag{2.3}$$

*k* corresponds to the wave number, $ncl$ and $nc$ correspond to the RI of the core and the cladding respectively. There are some modes with $\beta < kn_{cl}$, but they're partially confined, these are leaky modes [35].

Another parameter associated with modes is the V-number which is defined by [35]:

$$V = \frac{2\pi a}{\lambda}(n_c^2 - n_{cl}^2)^{1/2} = \frac{2\pi a}{\lambda}NA \quad (2.4)$$

a is the core's radius, λ is the light's wavelength and NA is the numerical aperture. To ensure mode guidance inside a waveguide, the V-number must be equal to or greater than 2.405. This parameter can be used to calculate the number of modes.

Optical fibers can be divided into two main categories based on the number of supported propagation modes: Single Mode Fiber (SMF) and Multimode Fiber (MMF). As the name suggests, a SMF supports only one propagating mode, Figure 2.4. This condition corresponds to a V-parameter (also known as the normalized frequency) of 2.405. In this regime, it is typically assumed that the light beam propagates nearly parallel to the fiber axis, minimizing modal dispersion.

Figure 2.4: Light propagation in SMF, adapted from [39].

A schematic of a SMF is shown in Figure 2.4. This type of fiber features a small core, typically ranging from 7 to 12 $\mu m$, surrounded by a cladding with a diameter of approximately 125 $\mu m$ [35,41]. The RI of the core, at a wavelength of 1550 nm, is typically around 1.456, while the cladding has an RI of approximately 1.444 [41].

MMF are optical fibers that support the propagation of multiple modes. Depending on how these modes travel through the fiber, MMFs are typically divided into two categories.

The first type is the step-index MMF, in which the core's RI remains constant across its radius. This results in light rays following straight-line trajectories, as illustrated in Figure 2.5.

The core diameter of step-index MMFs typically ranges from 50 to 200 $\mu m$, while the cladding diameter varies from 125 to 400 $\mu m$ [35,42].

At a wavelength of 632.8 nm, the core RI is approximately 1.457, and the cladding RI is around 1.439 [42].

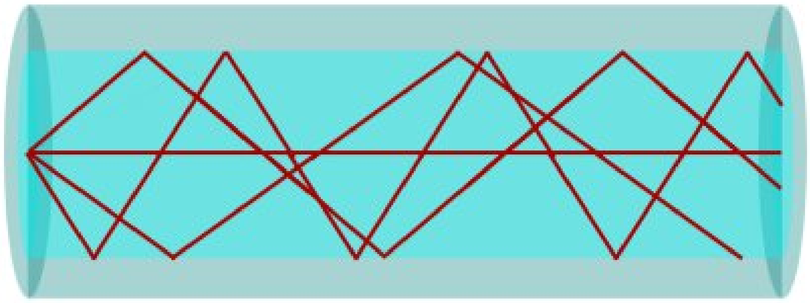

Figure 2.5: Light propagation in a Step-Index MMF, adapted from [39].

The second type of MMF is the graded-index MMF, in which the core's refractive index decreases non-linearly from the center of the core toward its periphery.

This gradual change in RI causes light rays to follow curved trajectories, as illustrated in Figure 2.6. Graded-index MMFs typically have different dimensional ranges compared to step-index MMFs. The core diameter usually ranges from 50 to 100 $\mu m$, while the cladding diameter varies from 125 to 140 $\mu m$ [35,43].

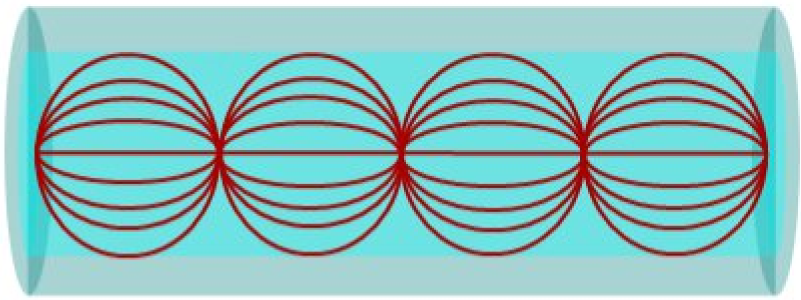

Figure 2.6: Light propagation in a Graded-Index MMF, adapted from [39].

Another, and more recent, optical fiber is the microstructured fiber, originally created by Russel and his team at the end of the last century [31]. Microstructured fiber has more versatile geometry when compared to traditional fibers. This fiber is characterized as being made of silica glass with an array of holes that extend to the hole fiber's length. Typically, there are two main geometries: the first is Solid Core Fiber (SCF), as the name implies there's a solid core and several holes around it, in this geometry light moves by TIR. The other geometry is characterized by having a hole as a core and silica around it, this served to name it Hollow Core Fiber (HCF). In this, light propagates by Photonic Band Gap (PBG) [44].

## 2.3. Sensors

Sensors are devices that detect changes in specific physical properties and convert them into measurable signals. These attributes typically include temperature, mass, speed, pressure, and others [45].

In the 21st century, a wide range of sensor architectures has emerged, each tailored to specific applications and physical phenomena. These include:

- **Electrical sensors**, which operate based on electrical signals. Measurements are derived from changes in voltage, current, resistance, or frequency [46].
- **Optical sensors**, which use light as the sensing medium. These sensors detect variations in phase, polarization, intensity, or wavelength [47].
- **Chemical sensors**, which rely on chemical reactions to generate measurable signals. The resulting outputs can be **electrical**, such as impedance [48], voltage [49], or current [50, 51]; or **optical**, based on photonic mechanisms such as localized surface plasmon resonance [52].

### 2.3.1. Optical fiber sensors

Optical fiber sensors (OFS) utilize optical fibers as a medium for photon transmission. This characteristic offers several advantages over traditional electrical sensors. Unlike electrons, photons are less susceptible to external electromagnetic interference, making OFS more robust in noisy environments. Additionally, optical fibers provide compactness and flexibility while offering superior sensitivity and resolution compared to their electrical counterparts. OFS also support multiplexing, enabling multiple measurements along a single fiber. Their chemical inertness and ability to propagate signals over long distances make them ideal for monitoring in extreme or hazardous environments [53,54]. Another key advantage is their compatibility with hybrid sensor architectures, for instance, systems that combine optical and electrical signal processing [55].

A typical experimental setup for OFS (see schematics in Figure 2.7) consists of a light source, either a broadband source or a laser, an optical fiber to guide the light, and a detection system tailored to the specific parameter being measured. For instance:

- The optical intensity is typically quantified using a photodetector coupled to an oscilloscope, enabling the temporal acquisition of the signal.
- The spectral characterization, in terms of wavelength, is carried out by means of an Optical Spectrum Analyzer (OSA), which provides high-resolution spectral measurements.

- The determination of the state of polarization of optical radiation is performed with a polarimeter, allowing for an accurate assessment of the polarization parameters.

This modular configuration allows to adapt the setup based on the sensing mechanism and desired output, ensuring flexibility and precision in experimental design.

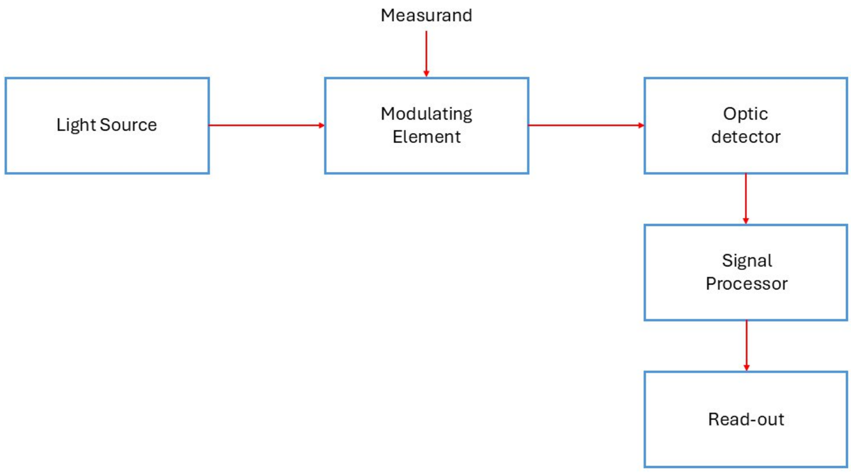


Figure 2.7: Generic block diagram of an optical fiber sensor, adapted from [56].

OFS can be used to measure a wide range of physical parameters, including temperature [57], curvature [58], RI [59], pressure [60], strain [61], magnetic field [62], among others. These sensors can operate in two main configurations. In **reflection mode**, the fiber tip is directly exposed to the measurand, allowing light to interact with it upon reflection. In **transmission mode**, the measurand interacts with a designated section of the fiber along its length, affecting the transmitted signal. Lastly, optical fibers used in sensing applications rely on several distinct working principles. Four major categories include: (1) Loss-related mechanisms, such as fiber attenuation, bending loss, or end coupling [63,64]; (2) Evanescent field interactions, including tapered fibers and surface plasmon resonance [65]; (3) Grating-based structures, such as Bragg gratings and Long Period Gratings [66]; (4) Interferometric configurations, including Fabry–Pérot, Mach–Zehnder, Michelson, and Sagnac interferometers [66].

#### *2.3.1.1. Sensors based on SMF or MMF*

This is the simplest type of OFS, using either SMF or MMF as the sensing element.

The SMF only has one mode, so the measurement is considered as a simple Fresnel's reflection as presented in Equation (2.5).

$$\frac{R_r}{R_i} = \left(\frac{n_f - n}{n_f + n}\right)^2 \tag{2.5}$$

$R_r$and $R_i$ are the powers of the reflected and incident rays respectively, $n_f$ is the fiber's RI and n is the measuarand's RI.

Another approach used is to measure the reflectance obtained in a known medium, such as air, and then compare the value of a certain unknown analyte with the known one, resulting in the following formula [67]:

$$\frac{R_{r,\,med}}{R_{i,air}} = \frac{K_{att}\left(\frac{n_f - n}{n_f + n}\right)^2}{K_{att}\left(\frac{n_f - n_a}{n_f + n_a}\right)^2} \tag{2.6}$$

$K_{att}$ is an attenuation coefficient that represents all losses in the system and $n_a$ is the air's RI.

On the other hand, MMF has several propagation modes, which disables Equation (2.5) as a valid approximation. There are three approximations for multimodal power distributions. The first approximation is the uniform distribution, which assumes that all modes carry the same power. The second is the Gaussian distribution, which assumes the light source is a Gaussian beam. Considering that the beam's center is aligned with the propagation axis, the following equation for power distribution is used [67]:

$$P_i(\alpha) = e^{-0.5\left(\frac{\alpha}{\sigma}\right)} \tag{2.7}$$

$P_i$ is the power distribution for each mode, $\alpha$ is the angle the mode makes with the propagation axis, and $\sigma$ is the standard deviation of the source's energy distribution [76]. The last approximation is the equilibrium mode distribution, which accounts for the mode coupling phenomenon. This model considers that coupling is typically caused by fiber bending or microscopic imperfections in the core, which lead to wave scattering and energy transfer between modes. The equation describing the evolution of power at a given angle is [67]:

$$\frac{\partial P(\alpha,z)}{\partial z} = -A(\alpha)P(\alpha,z) + \frac{\delta\alpha^2}{\alpha}\frac{\partial}{\partial\alpha}\left(\alpha C(\alpha)\frac{\partial P(\alpha,z)}{\partial\alpha}\right) \tag{2.8}$$

P($\alpha$,$z$) is the power inside the fiber at a distance z and at a certain angle $\alpha$, $C(\alpha)$ and A($\alpha$) are the coupling coefficient and the modal attenuation.

After traveling a certain distance, light reaches a stable state in which the energy distribution no longer changes. Once this state is reached, and neglecting attenuation losses (assuming the light travels short distances), the unpolarized light, based on a Gaussian input, is described as [67]:

$$P_i(\alpha) = J_0\left(2{,}405\frac{\alpha}{\alpha_{max}}\right) \quad (2.9)$$

$J_0$ is the Bessel function of the first kind and integer order zero, $\alpha_m$ is the maximum incidence angle [67].

After a couple of considerations of the reflected power, the expression Equation (2.10) is obtained for the $R_r/R_{r,air}$ [67].

$$\int_{\lambda_1}^{\lambda_2}\int_0^{\alpha_m} 0.5P_i(\alpha,\lambda)\frac{\left(K_{\perp,med} + K_{\parallel,med}(\alpha,\lambda)\right) sin(\alpha)\, d\alpha d\lambda}{\int_{\lambda_1}^{\lambda_2}\int_0^{\alpha_m} 0.5\ P\_i\,(\alpha,\lambda)\,(\left(K_{\perp,med} + K_{\parallel,med}(\alpha,\lambda)\right) sin(\alpha)\ d\alpha\ d\lambda} \quad (2.10)$$

In this equation an integral between two wavelengths is made, because it's considered the light source isn't monochromatic, so it may inject more than one wavelength, affecting the final result, because the refractive index is wavelength sensitive. $K_{\perp,ir}$ and $K_{\perp,med}$ are Fresnel power coefficients for perpendicular polarization, at interfaces fiber/air and fiber/ medium respectively, the same is applied for parallel polarization. Because of mode coupling, MMF creates an interference pattern that is sensitive to external changes, opening a new way to use this fiber as a sensor.

#### 2.3.1.2. *Evanescent Field Sensor*

In a standard fiber, light is guided inside the core by TIR. At each reflection, a small portion of energy transfers to the cladding, forming evanescent waves [68]. These waves exhibit exponential decay in the cladding region, with a penetration depth given by [68]:

$$d_p = \frac{\lambda}{2\pi\sqrt{n_{core}^2 sin^2(\theta_i) - n_{cladding}^2}} \quad (2.11)$$

$\theta_i$ is the incident angle of the light rays at interface core/cladding, $n_{core}$ is the core's RI and $n_{cladding}$ is the cladding's RI [68].

A taper is a fiber that has been elongated to a certain length, creating a region with a very thin diameter, as shown in Figure 2.8.

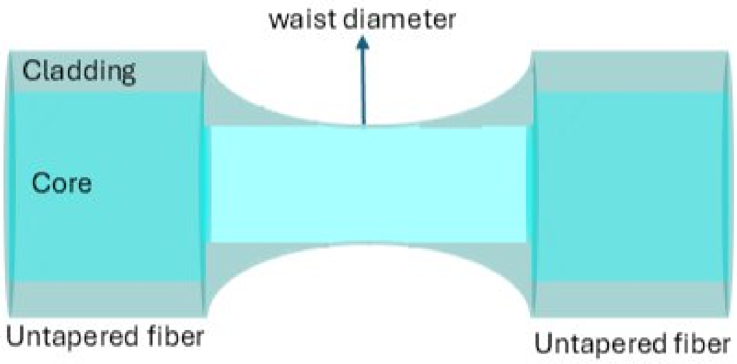


Figure 2.8: Representation of a fiber taper, adapted from [69].

When a SMF is tapered, the core diameter decreases, which causes the core's V-number to drop below 1. Meanwhile, the cladding's V-number increases beyond 2.405, allowing light to propagate within the cladding. This creates a new RI contrast between the cladding and the external medium, resulting in a new V-number defined by [68]:

$$V_p = \frac{2\pi a}{\lambda}\sqrt{n_{cladding}^2 - n_{external}^2} \quad (2.12)$$

a(z) is the radius of the fiber waist and $n_{external}$ is the RI of the external medium.

As this configuration forces light to propagate in the outer region of the fiber, it alters the penetration depth of the evanescent waves in the tapered zone [70].

$$d_p = \frac{\lambda}{2\pi\sqrt{n_{cladding}^2 sin^2(\theta_i) - n_{external}^2}} \quad (2.13)$$

Equation (2.13) shows that the penetration depth depends on the RI of the external medium. Consequently, variations in the transmitted light can be monitored and correlated with changes in the external medium's RI [66].

#### 2.3.1.3. *Fiber Grating Sensors*

A **Fiber Bragg Grating** (FBG) is formed by a periodic modulation of the refractive index in the fiber core along the propagation axis, acting as a wavelength-selective mirror [71], as illustrated in Figure 2.9. While most electromagnetic waves are transmitted through the fiber, those whose wavelengths satisfy Bragg's law (Equation 2.14) are reflected.

$$\lambda_B = 2\, n_e \Lambda \quad (2.14)$$

$\lambda_B$ represents the Bragg wavelength. $n_e$ is the core's refractive index and $\Lambda$ is the grating period.

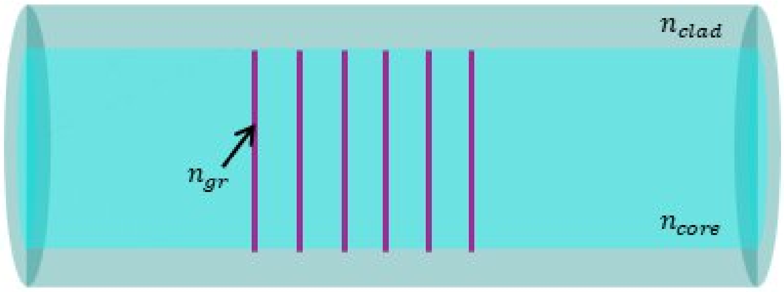


Figure 2.9: Representation of a Bragg grating, adapted from [66].

The simplest configuration is the uniform grating, in which the refractive index modulation in the fiber core is periodic with constant spacing. The reflectance spectrum of such gratings exhibits a peak around the Bragg wavelength, with reflectivities of approximately 10% and 90% for FBGs of 3 mm and 10 mm in length, respectively [72].

FBGs enable sensing applications because variations in the external medium induce changes either in the grating period or in the effective refractive index ($n_e$), leading to a shift in the Bragg wavelength. This configuration can operate in both reflection and transmission modes [71].

Another grating configuration is the **Long-Period Grating** (LPG), which is similar to the FBG but has a much larger period, typically in the millimeter range (0.1–1 mm), significantly greater than the wavelength of light [73].

In this type of OFS, core modes are coupled to forward-propagating cladding modes. As a result, the grating segment removes the wavelengths that satisfy the phase-matching condition with the grating period, which appear as attenuation bands (minima) in the transmission spectrum. Coupling wavelengths are determined by the phase matching expression [74]:

$$\lambda_i = (n_{eff,core} - n^i_{eff,\,cladding})\,\Lambda \tag{2.15}$$

$n_{eff,core}$ is the effective refractive index of the core, $n^i_{eff,cladding}$ is the effective refractive index of the cladding, $\lambda_i$ is the wavelength associated to the $i^{th}$ core mode and $\Lambda$ is the gratting's period [74]. This only works in transmission.

#### *2.3.1.4. Interferometric sensors*

An interferometric sensor operates by means of the interference between two light beams that travel along different optical paths. An interferometric fiber is typically composed of a beam splitter and a beam combiner [75]. Perturbations are detected through measurable variations in wavelength, intensity, phase, bandwidth, or frequency [76].

The **fiber Fabry-Pérot interferometer** (FFPI) is a traditional optical fiber with two reflectors separated by a certain distance [77]. These reflecting surfaces may be localized inside or outside the fiber [78], thus forming an intrinsic or extrinsic FP cavity, respectively (see Figure 2.10). In this OFS, maxima and minima appear in succession in the reflection and transmission spectra, because of the two interfering beams with two different optical paths being in or out of phase. The optical phase difference is given by [64]:

$$\varphi = \frac{2\pi}{\lambda_0} 2nL_{cav} \tag{2.16}$$

$\lambda_0$ is the wavelength in free space, $n$ is the refractive index of the cavity's material, and $L_{cav}$ is the length of the cavity [64].

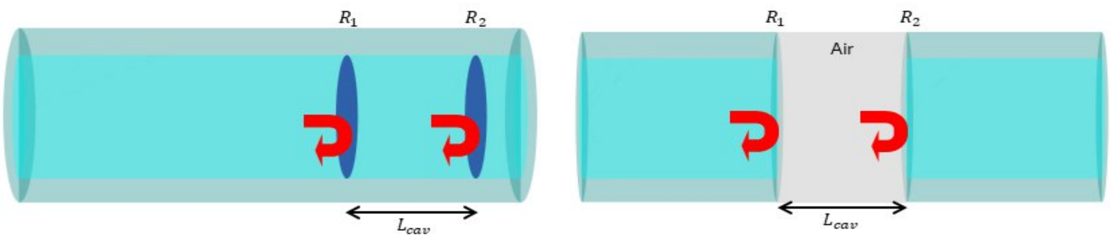


(a) Intrinsic Fabry-Pérot cavity.

(b) Extrinsic Fabry-Pérot cavity.

Figure 2.10: Representation of the fiber Fabry-Pérot interferometer: a) Intrinsic and b) extrinsic configurations. $R_1$ represents the first reflective facet and $R_2$ is the second one, while $L_{cav}$is the cavity length. Images adapted from [66].

From a sensing perspective, variations in the external medium change the properties of the Fabry–Pérot cavity, thereby modifying the optical path length. This results in shifts in the interference fringe pattern observed in the reflection or transmission spectrum [79,80].

The **Fiber Mach-Zehnder Interferometer** (Figure 2.11) is the fiber counterpart of the Mach Zehnder Interferometer. Light enters an initial fiber and then splits into two arms, one reference arm and one sensing arm, creating optical path interference. The two light beams then recombine and produce interference fringes in the transmission spectrum [81].

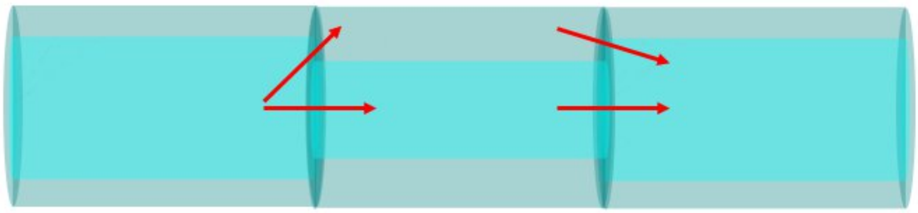

Figure 2.11: Representation of a fiber Mach-Zehnder interferometer, adapted from [66].

The fiber-optic **Mach–Zehnder Interferometer** (Figure 2.11) is the fiber-based counterpart of the traditional Mach–Zehnder interferometer. In this configuration, light entering the input fiber is split into two arms, one serving as a reference arm and the other as a sensing arm, where distinct optical paths are established. Upon recombination, the two beams interfere, producing interference fringes in the transmission spectrum [81].

The **Fiber-Optic Sagnac Interferometer** is composed of three-terminal couplers, two polarization controllers, and an optical fiber loop where two counterpropagating light beams with different polarization states travel. As in the previous interferometers, light propagates in a fiber and then splits into two beams that enter a sensing loop made of birefringent fiber to maximize the polarization dependence of the interferometer. At the end of the loop, both light beams return to the coupler. The phase of the interference is derived by [82]:

$$\varphi_{sa} = \frac{2\pi}{\lambda_0} BL \tag{2.17}$$

$B$ is the birefringent coefficient of the sensing fiber, given by $B = |n_f - n_s|$, where $n_s$ and $n_f$ are the effective RI of the slow and fast modes, and $L$ is the length of the loop [82].

#### 2.3.1.5. *Surface Plasmon Resonance*

Fiber-optic sensors based on surface plasmon resonance use the technique Surface Plasmon Resonance to detect changes in the external medium (analyte). Surface plasmons are a collective of oscillation modes that occur when an external electromagnetic field crosses the interface of a thin metal film with a dielectric analyte, making this technique very sensitive to RI. Generally, to create this sensor topology, the Kretschmann Raether prism geometry is implemented [83]. In the given geometry, p-polarized light is launched into a glass prism and then reflected from a thin metal (gold or silver) film deposited on the fiber end-face. This prism, with careful selection of the light wavelength and incident angle, aligns the phase of the incident light wave with a plasmonic wave at the metal/dielectric interface [84].

The propagation constant of a surface plasmon wave propagating at the interface between the metal and the contact medium is presented as follows [85]:

$$Q_{SP} = \frac{\omega}{c}\left(\frac{\epsilon_m \epsilon_s}{\epsilon_m + \epsilon_s}\right)^2 \tag{2.18}$$

$Q_{SP}$ is the propagation constant, $\epsilon_m$ and $\epsilon_s$ are the dielectric constants of the metal and dielectric, respectively, $\omega$ is the frequency of the incident light, and $c$ is the speed of light [85].

It is also possible to compute the propagation constant of the evanescent wave [85]:

$$Q_{ev} = \frac{\omega}{c}\sqrt{\epsilon_p} sin\,(\theta) \tag{2.19}$$

were $\theta$ is the angle of the incident light, and $\epsilon_p$ is the dielectric constant of the prism. Surface plasmons are only excited when the evanescent wave vector equals the plasmon wave vector at a particular angle, called the resonant angle, expressed by equating Equation (2.18) and Equation (2.19), considering the angle to be the resonant angle [85]:

$$\frac{\omega}{c}\left(\frac{\epsilon_m \epsilon_s}{\epsilon_m + \epsilon_s}\right)^2 = \frac{\omega}{c}\sqrt{\epsilon_p} sin\,(\theta_{res}) \tag{2.20}$$

This equation shows that changes in the refractive index of the analyte alter the equality condition of Equation (2.20), leading to variations in the reflected spectrum.

### 2.3.2. Fiber tip sensors

Fiber tip sensors refer to reflection-based sensors where a cleaved fiber end is placed in the material to be measured.

A typical fiber-tip OFS, considering RI measurements, consists of a broadband source connected to the first port of an optical circulator, as depicted in Figure 2.12. The second port of the circulator leads to the sensor head, where light is reflected and returns to the circulator. From there, light is directed to a device that processes the signal (through port 3), such as an OSA or an Optical Power Meter (OPM). Table 2.1 summarizes the fiber-tip based sensors reported in the literature since 2019.

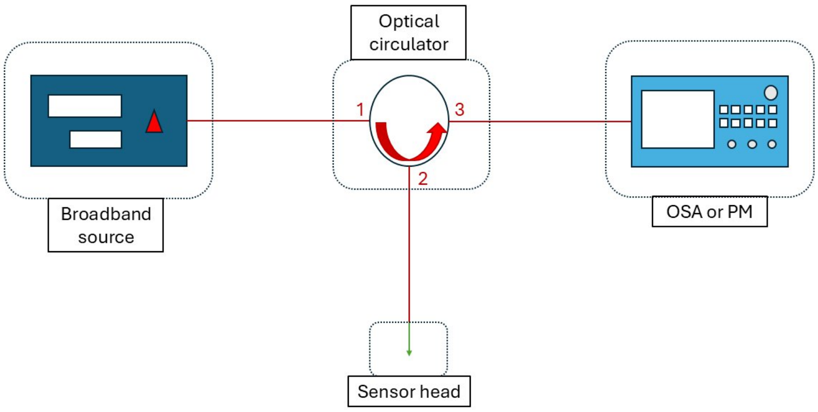


Figure 2.12: Schematics of a typical fiber-tip apparatus

Table 2.1: Reported literature on fiber-tip sensors.

| Publication Year | Sensor Mechanism | Configuration | Measurand | Range | Sensitivity | References |
|---|---|---|---|---|---|---|
| 2019 | Fabry Pérot (FP) + FBG | SMF + PCF MMF | RI, temperature | RI: 1.3315 −1.3708<br>temperature:<br>30-120ºC | RI: 9.13 dB/RIU<br>temperature (FBG): 11.46 pm/ºC temperature (PCF + FP): 8.62 pm/ºC | [86] |
| 2019 | FP | HCF + pyramidal polished SMF + SMF | RI,<br>temperature | RI: 1.3344-1.3418 temperature:<br>40-80ºC | RI: 1124.7 nm/RIU temperature: −9.6 pm/ºC | [87] |
| 2019 | SPR | MMF + SMF coated with Au | RI,<br>temperature, liquid level | RI: 1 −1.3761 temperature: 24-37ºC, liquid level (theorical): 0-8 mm | RI: 11.44 $RIU^{-1}$<br>temperature: -<br>2.58 ºC$^{-1}$<br>liquid level:<br>0.04 $mm^{-1}$ | [88] |
| 2019 | Axicon fiber-tip | SMF | RI | RI: 1.33 - 1.43 | 56%/RIU | [89] |
| 2021 | SMF | SMF | RI | RI: 1.31-1.36 | - | [67] |
| 2021 | MMF | MMF | RI | RI: 1.31-1.36 | - | [67] |
| 2022 | FBG | SMF + FBG + SMF | RI | RI: 1.333-1.471 | −590.625<br>dB/RIU at the<br>RI of 1.466<br>Remote<br>sensing:<br>−134.174 dB/RIU at the RI of 1.466 | [90] |
| 2022 | SPR-PCF | PCF with outside coated with Au | RI | RI: 1.35-140 | Wavelength:<br>10000 nm/RIU<br>Amplitude:<br>1115 $RIU^{-1}$ | [91] |
| 2022 | FFFPI | FFPI onto cleaved end of a SMF | Lysozyme concentration | 50-1000 ppb | x polarization: 15.1 nm/RIU y polarization: 14.4 nm/RIU | [92] |

| | | | | | | |
|---|---|---|---|---|---|---|
| 2022 | FBG | FBG with a core side hole fiber | RI | RI: 1.333-1.340 | x polarization: 15.1 nm/RIU y polarization: 14.4 nm/RIU | [93] |
| 2023 | Michelson Interferometer | | RI | RI: 1.3095-1.3439 | −128.7 dBm/RIU | [94] |
| 2023 | - | - | RI | - | 622dB/RIU | [95] |
| 2023 | GIF | SMF + GIF | RI | - | - | [96] |
| 2023 | Whispering Gallery Mode | SMF | RI | RI:1.33-1.35 | 25 nm/ RIU | [**97**] |
| 2024 | SPR | MMF (600 $\mu$m) coated with Au | RI, thrombin concentration | RIU: 1.3329-1.3605 concentration:2-100 nM | RI (wavelength): 2150 nm/RIU RI (amplitude): 7.136 a.u./RIU | [98] |

## 2.4. Concluding Remarks

In this chapter, the fundamental components and operating principles of optical fibers were introduced. Regarding fiber types, the three most basic and widely used classifications were presented. Subsequently, the concept of sensors was outlined, accompanied by an overview of several existing sensor technologies. In line with the focus of this work, particular attention was devoted to OFS, emphasizing their advantages and operating principles. A range of OFS architectures was discussed, beginning with the simplest configurations employing standard SMF or MMF fibers, followed by tapered fibers and fiber gratings, and culminating in interferometric sensors such as Fabry–Pérot, Mach–Zehnder, Michelson, and Sagnac. The surface plasmon resonance technique was also briefly introduced. Finally, the specific sensor type employed in this work, fiber-tip sensors, was described, including the materials used and a simplified schematic representation. The chapter concluded with a review of the state of the art in fiber-tip sensors across different architectures, with particular emphasis on RI measurement.

# 3. Refractometric Fiber Tip Sensors

## 3.1. Introduction

Refractometric sensors are designed to measure the RI of the surrounding medium and can be implemented in a variety of configurations, as outlined in the previous chapter. This chapter focuses on fiber-tip sensors, starting with the simplest design based solely on SMF. Following, more complex structures employing MMFs are studied, including both step index and graded-index profiles. In addition, more advanced fiber types are considered, such as microstructured fibers operating under TIR conditions, and cut FBGs, where the cutting process allows cladding modes to couple into the core, thereby enhancing sensitivity to refractive index variations. At the end of the chapter, the experimental results are reviewed, and a comparative analysis between the different sensor configurations is presented.

## 3.2. Experimental apparatus and methodology

The experimental apparatus used in this study was assembled using materials available in the laboratory. A broadband source (Photonetics 3627 IN) served as the light source. The light was guided through a SMF to a 50:50 coupler, from which it was directed toward the sensor head. The reflected light was then routed back either to the optical spectrum analyzer (OSA, Yokogawa AQ6370C) or to the power meter (Agilent 8163B).

To improve measurement stability, the fiber tip was held in place by a custom-built positioning device developed by the research institute. This device was responsible for raising, lowering, and maintaining fiber at a fixed position during the experiments. The experimental apparatus is visible in Figure 3.1.

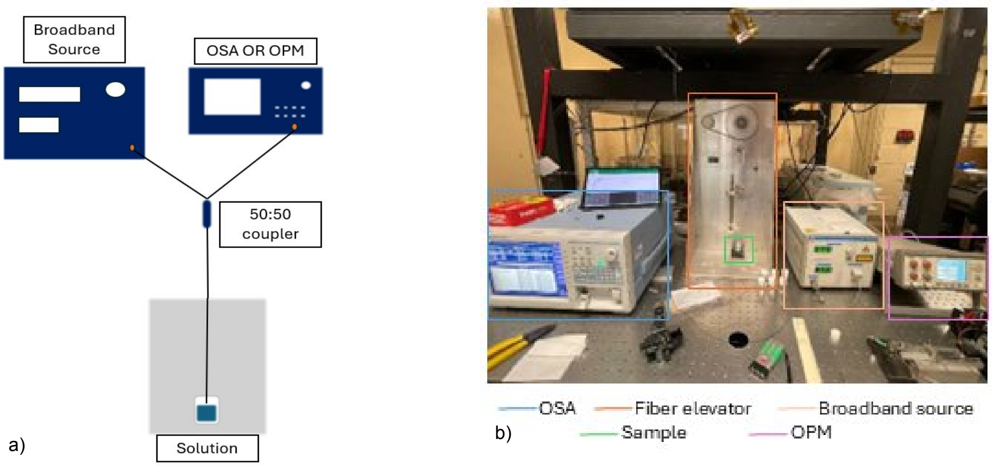


Figure 3.1: a) Schematics and b) picture of the experimental apparatus used for the RI study.

To obtain reliable results, the measurement procedure was carried out using a consistent and repeatable approach. The methodology adopted is detailed below.

First, the output of the broadband source was activated, and the pump current was adjusted to approximately 102.6 mA, yielding an output power of 40 mW. The source was then connected directly to the OSA. On the OSA side, the analyzed spectrum channel was normalized, the resolution was maintained at 2 nm, and the wavelength range was narrowed to 1530–1570 nm.

The test solutions consisted of mixtures of distilled water and Isopropyl alcohol (IPA). These mixtures were prepared so that the RI values, measured using an Abbe refractometer (ATAGO DR-A1), were approximately evenly spaced.

Once all materials were prepared, a sensing head was spliced to a SMF and positioned using the leveling machine. Initially, the reflection power and spectrum in air were recorded. Subsequently, the same two measurements were carried out for each prepared mixture, first following an ascending RI sequence, and then a descending one. After completing the first round of measurements, a second round was conducted, excluding the air reference.

## 3.3. SMF-based tip sensor

The fiber sensor was based on SMF, the SMF28 model (0.14 NA, Thorlabs, featuring a core diameter of 8.2 µm and a cladding diameter of 125 µm. After cleaving the fiber tip, the sensing region became a flat surface perpendicular to the fiber axis, allowing direct interaction with the surrounding medium. When light reaches the interface between the fiber and the analyte, a portion of it is reflected, while the remainder is transmitted through the boundary (Figure 3.2), following the principles described by Fresnel reflection (Equation 2.5). Under normal conditions, approximately 4% of the incident light is reflected at the interface, resulting in an intensity-modulated sensor in which changes in the reflected power correlate with variations in the refractive index of the surrounding medium.

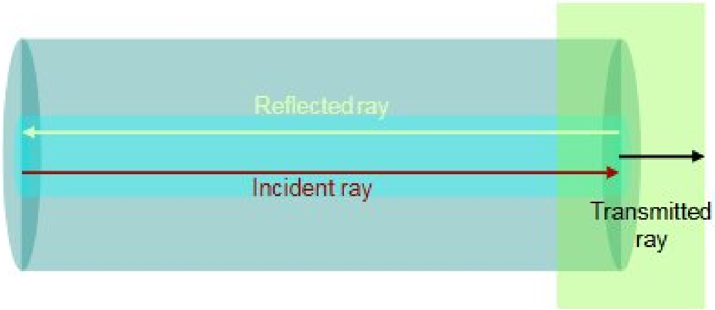


Figure 3.2: Representation of light propagation when the cleaved tip is in contact with the external medium.

Figure 3.3 represents the reflected optical power, measured in microwatts (µW), obtained from the interaction between the cleaved fiber tip and various RI mixtures.

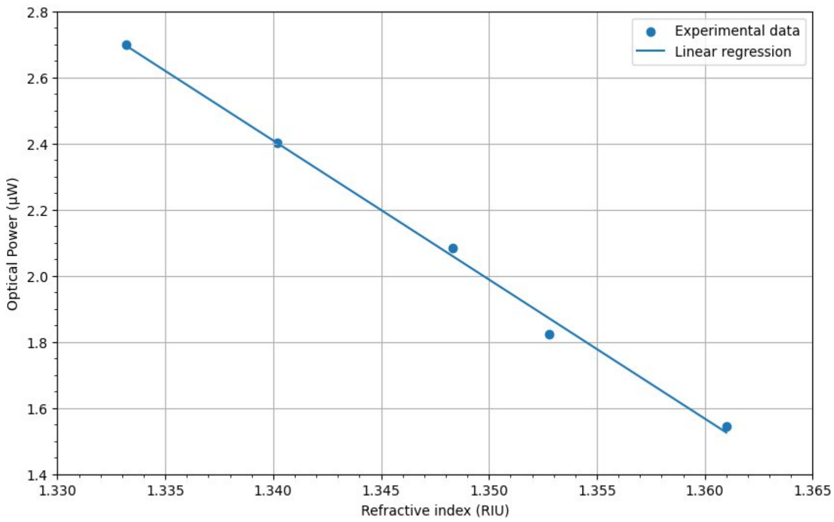


Figure 3.3: Optical power variation of the SMF-tip sensor as a function of RI.

The obtained values display a clear linear trend, demonstrating that the sensor's intensity sensitivity remains consistent throughout the entire experimental dataset.

The sensitivity of a sensor is defined by Equation (3.1), which expresses the ratio between the variation in the sensor's output and the corresponding change in the input stimulus. In practice, sensitivity is often determined by performing a linear regression over a specific operating region.

$$sens = \frac{\Delta measurand}{\Delta input} \tag{3.1}$$

In this case, the measured sensitivity was −42 ± 2 µW/RIU with a power-intercept of 59 ± 2 µW, with a correlation coefficient of $R^2 = 0.9954$, confirming a strong linear relationship between the reflected intensity and the refractive index of the tested mixtures.

## 3.4. Step-index MMF-based tip sensor

This sensor configuration consists of a step-index MMF, specifically the FG105LCA model from Thorlabs, with a core diameter of 50 μm, a cladding diameter of 125 μm, and a length of 6 cm. The sensing head is spliced to a SMF, forming a hybrid structure that enables efficient light delivery and reflection-based sensing. This setup is illustrated in Figure 3.4.

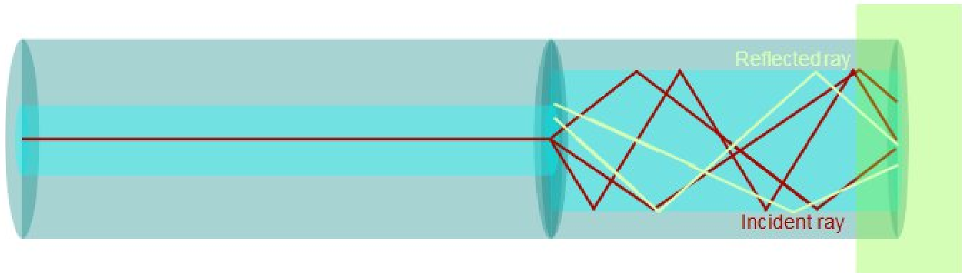


Figure 3.4: Representation of the step-index MMF used in the experiment.

In this sensor configuration, light propagates from the SMF into the MMF, where it is shattered into multiple propagation modes. These modes undergo Fresnel reflection at the cleaved fiber tip, and a portion of the reflected light is recoupled back into the SMF. The interference between these reflected modes generates a reflection spectrum, which is sensitive to changes in the RI of the external medium. This spectral response can be used to detect and quantify variations in the surrounding environment.

As with the previous sensor, there is a clear correspondence between the reflected optical power and the RI of the mixture, as shown in Figure 3.5. A quadratic regression was applied to the data because it was the regression that fitted the best the data behavior. The resulting fit originated the parameters 190 ± 60 μW/RIU$^2$, 500 ± 200 μW/RIU and 400 ± 100 μW yielding a correlation coefficient of $R^2$ = 0.9919, indicating excellent agreement between the experimental data and the regression model.

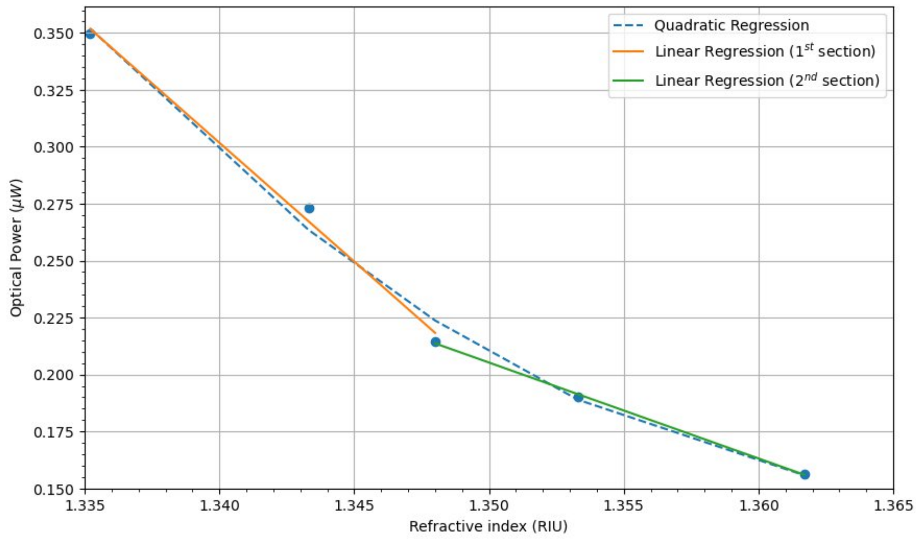


Figure 3.5: Optical power variation of the step-index MMF-tip sensor as a function of RI. Experimental data obtained with the OPM.

For the sensitivity analysis, given the quadratic nature of the results, the data were divided into two distinct regions: one corresponding to lower RI values, ranging from 1.3352 to 1.348, and another corresponding to higher RI values, ranging from 1.348 to 1.3617. The sensitivities obtained for each RI range and the corresponding correlation coefficients are depicted in Table 3.1.

| RI Range | Sensitivity (μW/RIU) | Power-intercept (μW) | $R^2$ |
|---|---|---|---|
| **1.3352 − 1.3480** | -10.4 ± 0.8 | 14 ± 1 | 0.9940 |
| **1.3480 − 1.3617** | -4.2 ± 0.2 | 5.9 ± 0.2 | 0.9984 |

Table 3.1: Sensitivities obtained for each RI range and the corresponding correlation coefficients. Experimental data of the step-index MMF-tip sensor obtained with an OPM.

For each mixture, the reflection spectrum was also analyzed using the OSA, as shown in Figure 3.6. The spectral window was set between 1530 nm and 1570 nm, since regions outside this range primarily contain noise from the broadband source. The resulting spectra exhibits multiple peaks and valleys, characteristic of multimodal interference within the fiber structure. Notably, the overall spectral shape remains consistent across different mixtures, with only slight shifts in the wavelength positions of the interference features, reflecting subtle changes in the RI of the external medium.

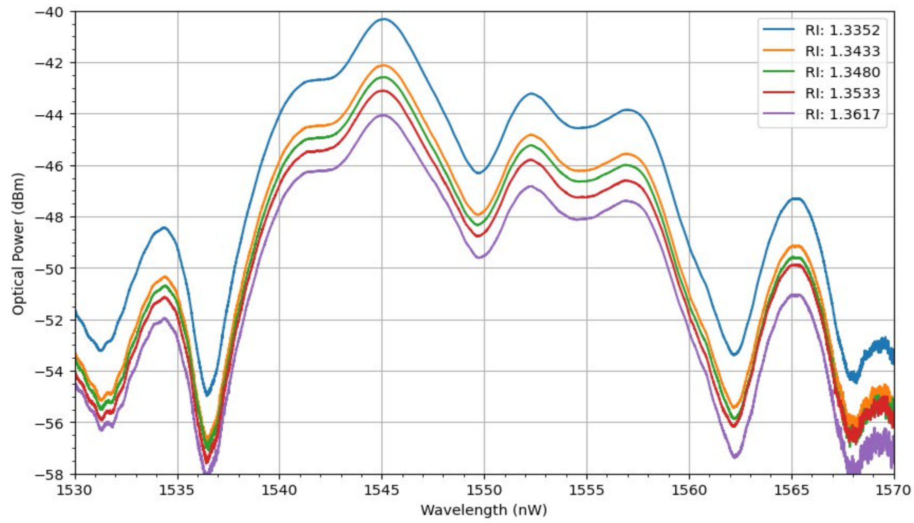


Figure 3.6: Observed spectrum when the step-index MMF-tip sensor is in contact with distinct RI mixtures.

Also, in Figure 3.6, variations in the reflected optical power are clearly visible, reflecting the influence of different Fresnel reflection coefficients associated with each RI mixture.

Given these conditions, the wavelength 1556.99 nm was selected as a reference point across all spectra. The reflected optical power at this wavelength was extracted and correlated with the corresponding RI values of the mixtures. The same analytical procedure previously applied to the OPM data was then replicated, enabling a direct comparison between spectral and intensity-based sensing approaches.

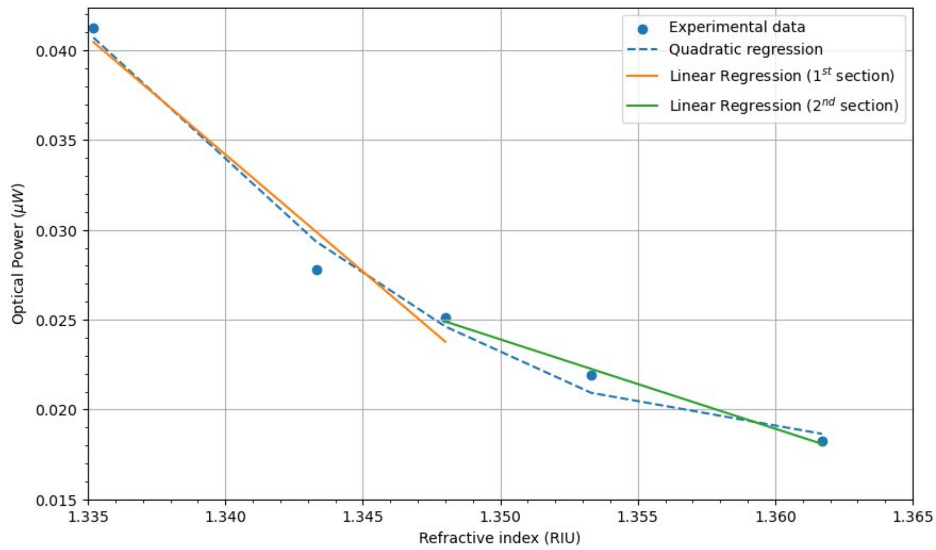


Figure 3.7: Optical power variation of the step-index MMF-tip sensor as a function of RI. Experimental data obtained with the OSA.

Figure 3.7 illustrates the relationship between reflected optical power and the RI of the external medium. A quadratic regression was applied to the data obtaining the regression terms 31 ± 8 μW/RIU$^2$, -80 ± 20 μW/RIU and 60 ± 10 RIU yielding a correlation coefficient of $R^2$ = 0.9866. Also, a linear regression was performed to estimate the sensor's sensitivity, focusing on a specific region of the data where the response approximates linear behavior. The results obtained from this analysis are summarized in Table 3.2, providing a comparative overview of the sensor's performance across different RI ranges.

Table 3.2: Sensitivities obtained for each RI range and the corresponding correlation coefficients. Experimental data of the step-index MMF-tip sensor obtained with an OSA.

| RI Range | Sensitivity (μW/RIU) | Power-intercept (μW) | $R^2$ |
|---|---|---|---|
| **1.3352 - 1.3480** | -1.30 ± 0.30 | 1.8 ± 0.4 | 0.9535 |
| **1.3480 - 1.3617** | -0.50 ± 0.05 | 0.70 ± 0.06 | 0.9917 |

To compare the performance of both analytical approaches, the reflected power values were normalized, allowing for a direct comparison. The corresponding normalized data is presented in Table 3.3.

| RI Range | Sensitivity ($RIU^{-1}$) | $R^2$ |
|---|---|---|
| **1.3352 − 1.3480 - OPM** | -3.90 ± 2.9 | 0.9940 |
| **1.3480 − 1.3617 - OPM** | -12.0 ± 0.5 | 0.9984 |
| **1.3352 − 1.3480 - OSA** | -32.0 ± 7.0 | 0.9535 |
| **1.3480 − 1.3617 - OSA** | -17.0 ± 2.0 | 0.9917 |

Table 3.3: Sensitivities obtained for each RI range and the corresponding correlation coefficients. Normalized values of the step-index MMF-tip sensor acquired from the OPM and OSA.

An alternative analysis was conducted by fixing the optical power and identifying the wavelength at which each spectrum reached that power for a given RI. The spectral range between 1537 nm and 1541 nm was selected, as it contains stable features suitable for this evaluation. The mean power of the spectrum corresponding to the lowest RI (−48.348 dBm) was calculated and used as a reference threshold. To determine the wavelength at which this power level occurred in each spectrum, polynomial regressions were applied to segmented portions of the data, as illustrated in Figure 3.8.

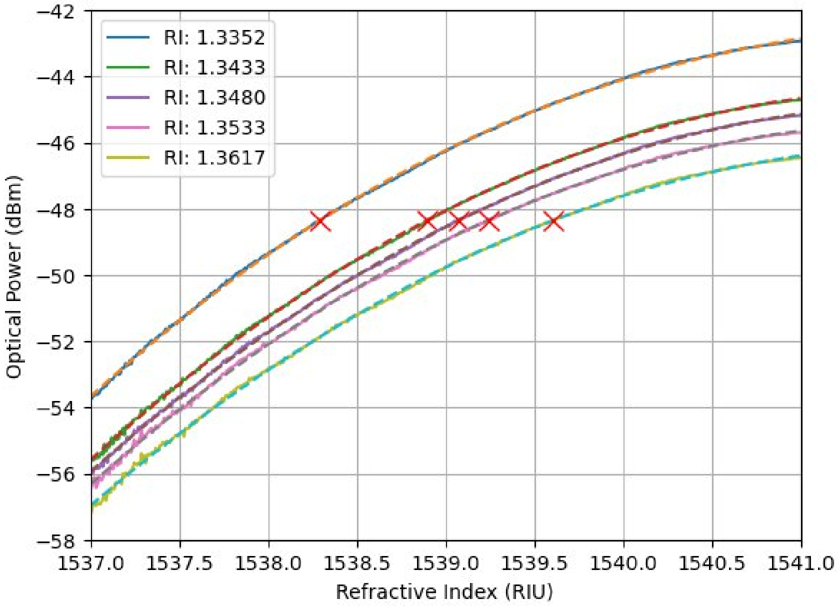


Figure 3.8: Spectral window with the various spectra chosen for analysis, and red crosses indicating the mean point corresponding to the minimum RI.

Following this approach, multiple wavelengths were extracted and plotted in Figure 3.9, representing RI as a function of wavelength. The data were segmented into two regions, lower RI values (1.3352 to 1.348) and higher RI values (1.348 to 1.3617), to maintain consistency with the previous sensitivity analysis.

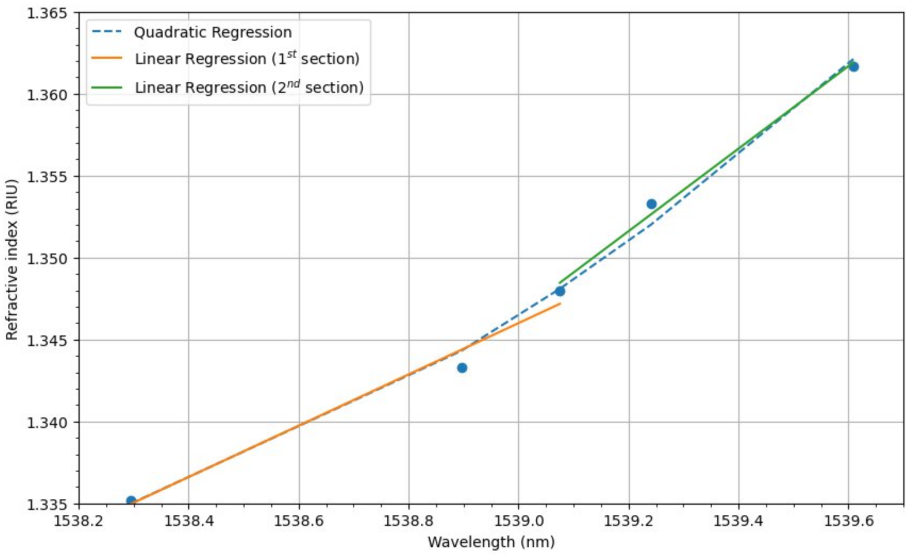


Figure 3.9: Refractive index variation of the step-index MMF-tip sensor as a function of wavelength. Experimental data obtained with the OSA.

The results of the linear regressions are summarized in Table 3.4, demonstrating the viability of this approach and its consistency with the previously discussed intensity-based methods.

| RI Range | Sensitivity (RIU/nm) | RI-intercept (RIU) | $R^2$ |
|---|---|---|---|
| **1.3352 - 1.3480** | 0.015 ± 0.002 | -23 ± 4 | 0.9774 |
| **1.3480 - 1.3617** | 0.025 ± 0.002 | -37 ± 3 | 0.9928 |

Table 3.4: Sensitivities obtained for each RI range and the corresponding correlation coefficients. Experimental data of the step-index MMF-tip sensor obtained with an OSA.

## 3.5. Graded-index MMF-based tip sensor

To assemble the MMF-based sensor, an 8 cm-long graded-index fiber (GIF625, Thorlabs), was spliced to a SMF, as illustrated in Figure 3.10. As in the previous case, at the splicing region the light divides into several modes, which reflect independently at the fiber/analyte interface.

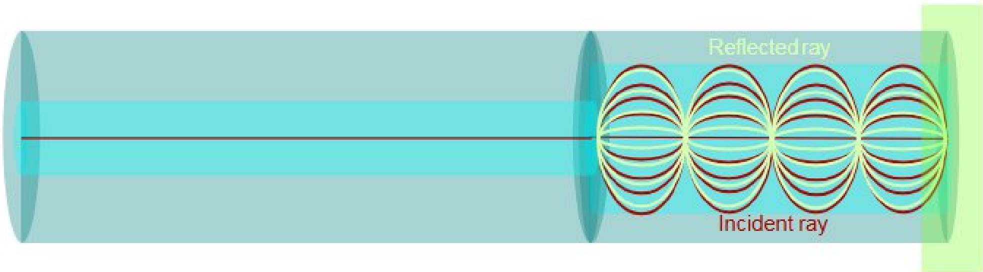


Figure 3.10: Representation of the Graded-Index MMF used in the experiment.

As with all the previous sensors, this fiber is sensitive to the percentage differences in Fresnel reflections caused by contact with different analytes. The results obtained by reading the reflected power with the optical power meter are presented in Figure 3.11. As in the previous case, a quadratic regression was applied to the data, regression terms obtained are 1300 ± 400 μW/RIU$^2$, -4000 ± 1000 μW/RIU and 2400 ± 800 μW, yielding a correlation coefficient of $R^2$ = 0.9730, which indicates a reasonably good fit to the experimental data.

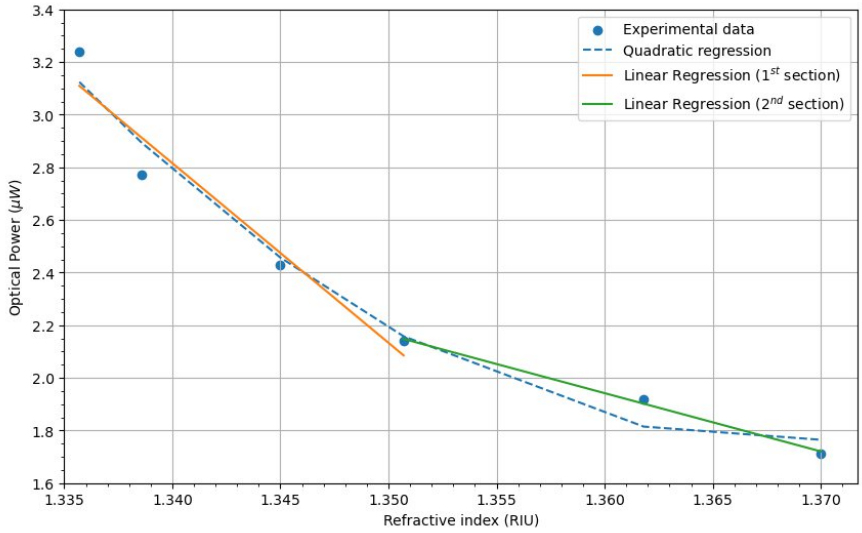


Figure 3.11: Optical power variation of the graded-index MMF-tip sensor as a function of RI. Experimental data obtained with the OPM.

Figure 3.11 also shows the linear regressions used to calculate sensitivity. In this case, the first region (lower RI), shown as the blue line in the figure, spans from 1.3357 to 1.3507, while the second region (higher RI), shown as the orange line, covers the range from 1.3507 to 1.3700. The obtained sensitivities and associated correlation coefficients are presented in Table 3.5.

| RI Range | Sensitivity (μW/RIU) | Power-intercept (μW) | $R^2$ |
|---|---|---|---|
| **1.3352 - 1.3480** | -70 ± 10 | 90 ± 20 | 0.9373 |
| **1.3480 - 1.3617** | -22 ± 2 | 32 ± 2 | 0.9947 |

Table 3.5: Sensitivities obtained for each RI range and the corresponding correlation coefficients. Experimental data of the graded-index MMF-tip sensor obtained with the OPM.

The spectral analysis of this sensor is presented in Figure 3.12. It is possible to observe a lack of peaks and valleys in the spectra, which occurs due to the way the modes propagate inside the fiber, preventing modal interference. As a result, only variations in the reflected power are visible.

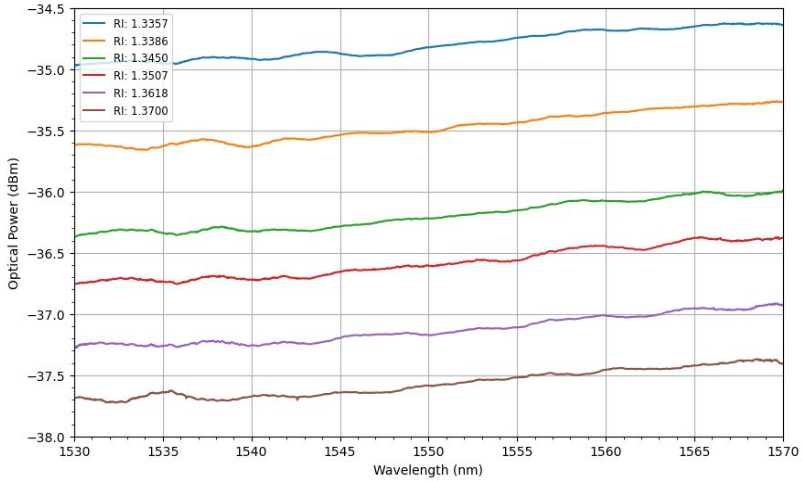


Figure 3.12: Spectra obtained for the graded-index MMF-tip sensor when immersed in distinct RI mixtures.

The absence of peaks and valleys only allows for the analysis of the optical power differences between spectra. To process this data, a narrow spectral window between 1546.6 nm and 1546.8 nm was selected to obtain a flat horizontal region. A fixed point within this window, 1546.6 nm, was chosen to evaluate the reflected power for each spectrum at that wavelength. After correlating the power values with the corresponding RI analogous to the data obtained from the OPM, two linear regressions were performed over the same RI ranges, resulting in the plot shown in Figure 3.13.

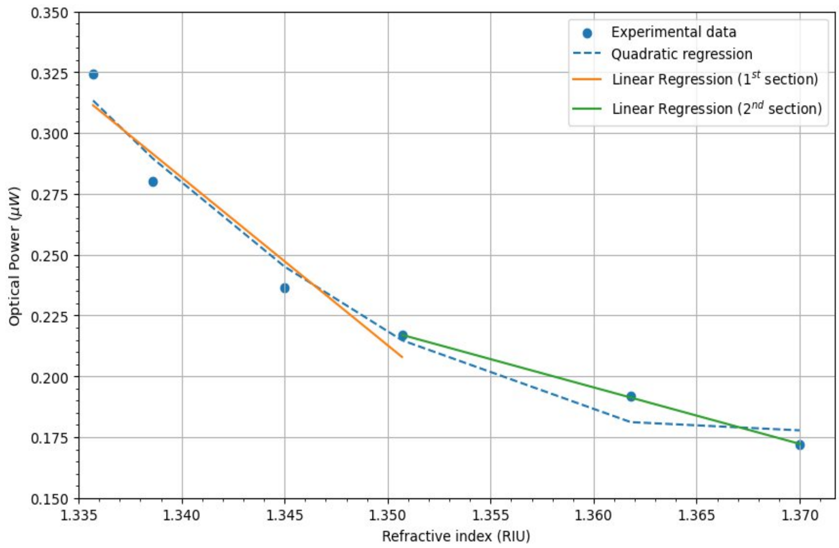


Figure 3.13: Optical power variation of the graded-index MMF-tip sensor as a function of RI. Experimental data obtained with the OSA.

With these two linear regressions, it was possible to calculate the sensitivities in the two RI ranges, which are presented in Table 3.6.

| RI Range | Sensitivity (μW/RIU) | Power-intercept (μW) | $R^2$ |
|---|---|---|---|
| **1.3357 – 1.3507** | -7.00 ± 1.00 | 9 ± 2 | 0.9292 |
| **1.3507 – 1.3700** | -2.32 ± 0.05 | 3.35 ± 0.06 | 0.9996 |

Table 3.6: Sensitivities obtained for each RI range and the corresponding correlation coefficients. Experimental data of the graded-index MMF-tip sensor obtained with the OSA.

As the optical power scales are much smaller for spectral optical power than for integrated optical power, both datasets were normalized, and the regressions were repeated to compare sensitivity across both approaches.

| RI Range | Sensitivity ($RIU^{-1}$) | $R^2$ |
|---|---|---|
| **1.3357 – 1.3507 - OPM** | -21.0 ± 4 | 0.9373 |
| **1.3357 – 1.3507 - OSA** | -21.0 ± 4 | 0.9292 |
| **1.3507 – 1.3700 - OPM** | -6.8 ±0.5 | 0.9947 |
| **1.3507 – 1.3700 - OSA** | -7.1 ±0.1 | 0.9996 |

Table 3.7: Sensitivities obtained for each RI range and the corresponding correlation coefficients. Normalized values of the graded-index MMF-tip sensor acquired from the OPM and OSA.

## 3.6. Microstructured MMF-based tip sensor

The sensor head used consists of 8 cm of the microstructured fiber shown in Figure 3.14, a fiber manufactured by IPHT (Jena, Germany) with reference 184b3a. This fiber has an outer diameter of 127.0 μm, spliced to a SMF, and a core diameter of 79.0 μm. It features two rings of holes with diameters of 4.1 μm and 2.2 μm, respectively.

Figure 3.14: Picture of the microstructured MMF, image not in scale.

As the core diameter of the microstructured fiber is larger than that of the SMF (8.2 μm), light propagates in multiple modes, like what occurs in step-index MMF, as illustrated in Figure 3.4. This fiber, due to its similarities with the step-index MMF, can detect differences in Fresnel reflections when the fiber tip encounters different analytes. Figure 3.15 presents the experimental data along with a quadratic regression, with regression parameters 170 ± 50 μW/RIU², -500 ± 100 μW/RIU and 300 ± 100 μW yielding a correlation coefficient of $R^2$ = 0.9834, which provides a reasonably good fit to the data.

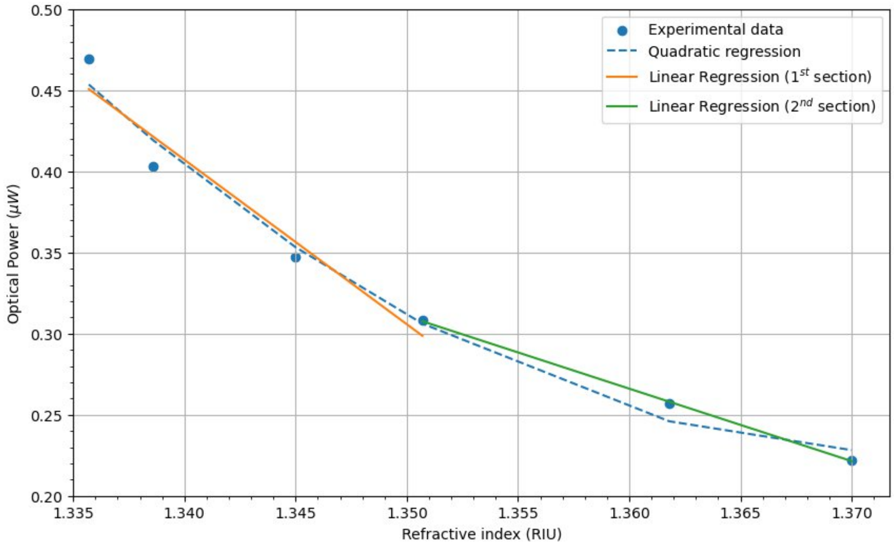


Figure 3.15: Optical power variation of the microstructured MMF-based tip sensor as a function of RI. Experimental data obtained with the OPM.

To evaluate this sensor, data were divided into two regions: one for lower RI values, ranging from 1.3357 to 1.3507, and another for higher RI values, ranging from 1.3507 to 1.3700. The calculated sensitivities are presented in Table 3.8.

| RI Range | Sensitivity (μW/RIU) | Power-intercept (μW) | $R^2$ |
|---|---|---|---|
| **1.3357 − 1.3507** | -10.00 ± 2.00 | 14.00 ± 2.00 | 0.9425 |
| **1.3507 − 1.3700** | -4.46 ± 0.09 | 6.30 ± 0.10 | 0.9996 |

Table 3.8: Sensitivities obtained for each RI range and the corresponding correlation coefficients. Experimental data of the microstructured MMF-based tip sensor obtained with the OPM.

Another laboratory study involved connecting the apparatus to an OSA to perform spectral analysis, as shown in Figure 3.16. The first noticeable feature is the presence of peaks and valleys, characteristic of multimodal interference. The second is the preservation of the overall spectral shape, with variations in reflected optical power caused by differences in reflection coefficients. The third, more visually striking in the valley between 1535 nm and 1540 nm, is a subtle wavelength shift. These last two features enable two distinct analytical approaches: the first involves fixing a wavelength and observing the optical power across all spectra; the second fixes the optical power level and tracks the corresponding wavelength shifts.

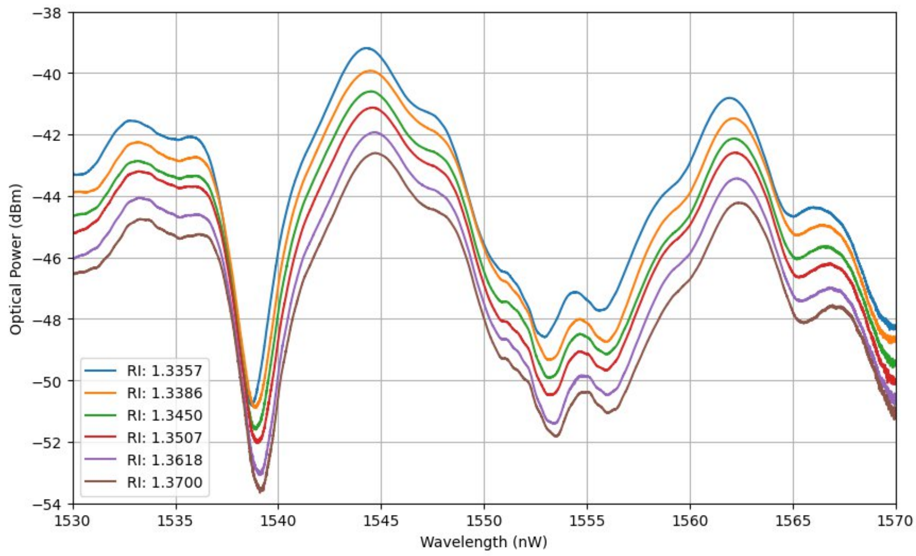


Figure 3.16: Spectral Response of the microstructured MMF-based tip sensor.

By maintaining a constant wavelength at 1544.28 nm, the reflected optical power for each spectrum was analyzed. The resulting data were then divided into the same two regions as defined in Table 3.8. The outcomes of the corresponding regressions are presented in Table 3.9.

| RI Range | Sensitivity (µW/RIU) | Power-intercept (µW) | $R^2$ |
|---|---|---|---|
| **1.3357 − 1.3507** | -2.80 ± 0.50 | 3.9 ± 0.7 | 0.9291 |
| **1.3507 − 1.3700** | -1.19 ± 0.02 | 1.68 ± 0.03 | 0.9997 |

Table 3.9: Sensitivities obtained for each RI range and the corresponding correlation coefficients. Experimental data of the microstructured MMF-based tip sensor obtained with the OSA.

Since the scales differ significantly between the two methods used to measure optical power, the following table presents linear regressions of normalized values for each group of data points, as shown in Table 3.10.

Table 3.10: Sensitivities obtained for each RI range and the corresponding correlation coefficients. Normalized values of the microstructured MMF-based tip sensor acquired from the OPM and OSA.

| RI Range | Sensitivity ($RIU^{-1}$) | $R^2$ |
|---|---|---|
| **1.3357 − 1.3507 - OPM** | -22.0 ± 4.0 | 0.9425 |
| **1.3357 − 1.3507 - OSA** | -23.0 ± 4.0 | 0.9291 |
| **1.3507 − 1.3700 - OPM** | -9.5 ± 0.2 | 0.9996 |
| **1.3507 − 1.3700 - OSA** | -9.9 ± 0.2 | 0.9997 |

By fixing a specific optical power level, wavelength shifts across the spectra can be observed, as shown in Figure 3.18. For this analysis, a spectral window between a valley and a peak, from 1540 nm to 1545 nm, was selected. In the spectrum corresponding to the lowest RI value, the mean point between the minimum and maximum was calculated as −42.502 dBm, and this optical power level was fixed (indicated by red crosses in Figure 3.17).

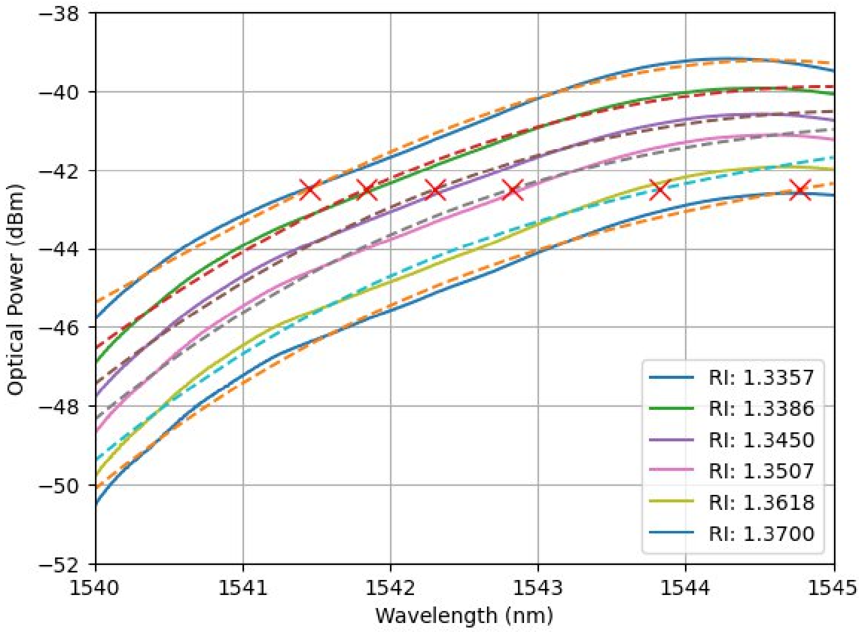


Figure 3.17: Spectral window with the various spectra chosen for analysis, and red crosses indicating the mean point corresponding to the minimum RI.

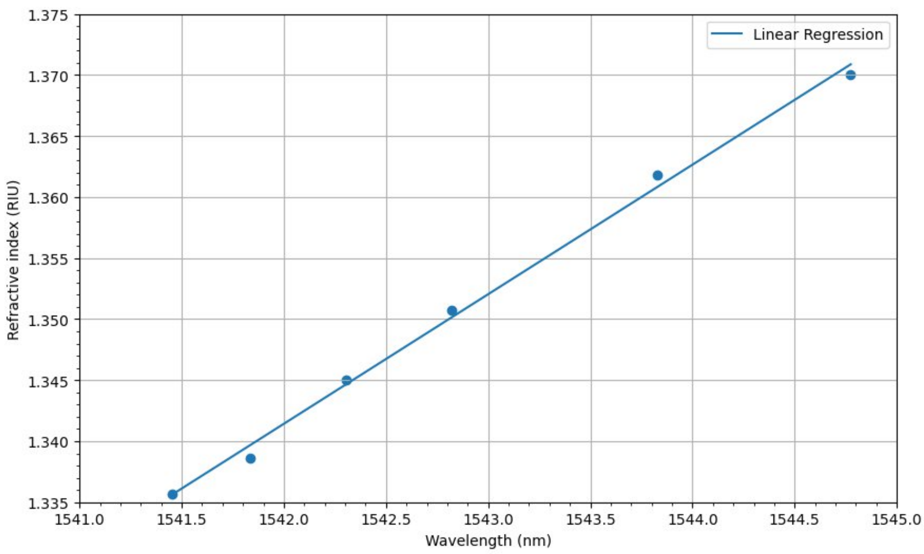


Figure 3.18: Refractive index variation of the microstructured MMF-based tip sensor as a function of wavelength. Experimental data obtained with the OSA.

Since this exact optical power value did not occur in all spectra, polynomial regressions were applied to each spectrum to approximate the corresponding wavelength. These values enabled the calculation of the relationship between wavelength and the RI of the mixture, as presented in Figure 3.18. Since the data show minimal deviation between the two RI zones, a single linear regression was applied to the entire dataset.

Looking at the plot, it’s possible to see the linear regression adjusts very well to the data, the obtained sensitivity is 0.0107 ± 0.0003 RIU/nm with a $R^2$ of 0.9963.

## 3.7. FBG-based tip sensor

This sensor is composed of a cleaved FBG written in a standard SMF. This process preserves the FBG peak while allowing the grating to be positioned at the fiber tip. In this configuration, light travels from the SMF passing by the FBG. When it encounters the grating, light at a specific wavelength, determined by Bragg’s law (Equation 2.14), is reflected. Light at other wavelengths passes through the grating and is reflected by Fresnel reflections at the fiber/analyte interface. Differences in the reflection coefficient arise from variations in the RI of the analyte. The sensor’s scheme is illustrated in Figure 3.19.

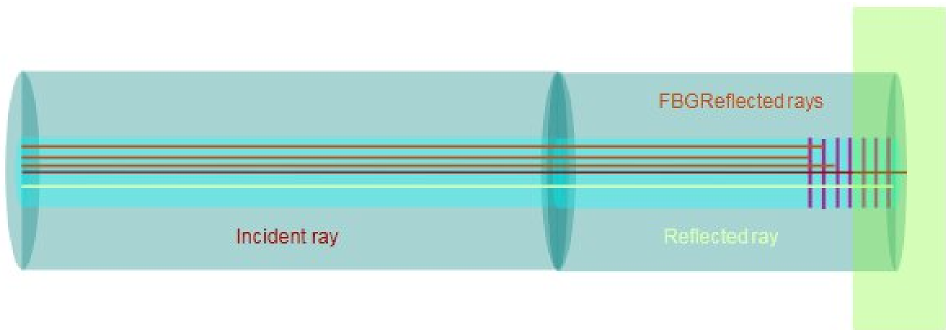


Figure 3.19: Representation of the FBG-based tip sensor, image not in scale.

An initial study was conducted by reading the integrated optical power using an OPM, with the fiber tip in contact with different mixtures of water and IPA. The experimental data is presented in Figure 3.20. A clear correlation was observed between the reflected optical power and the RI of the mixtures: as the refractive index increases, the reflected optical power decreases. A quadratic regression was applied to this dataset to model the decay in reflected light, yielding a correlation coefficient of $R^2$ = 0.9881, indicating a strong fit.

As with the previously tested sensors, the data were divided into two regions: one for lower RI values (1.3357 to 1.3507) and another for higher RI values (1.3507 to 1.3700).

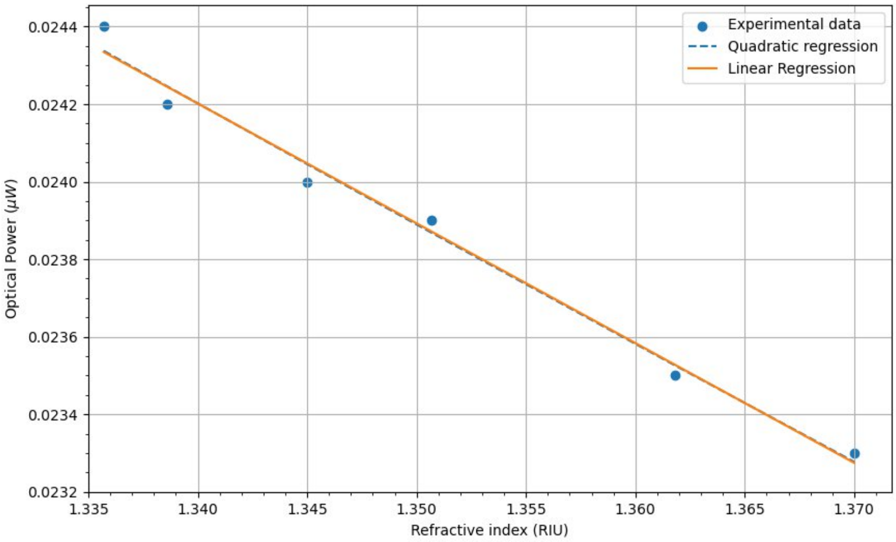


Figure 3.20: Optical power variation of the FBG-based tip sensor as a function of RI. Experimental data obtained with the OPM.

Due to its linear behavior across all ranges, contrary to other sensor heads, it was made a linear regression. It was obtained a sensitivity of -0.032 ± 0.002 $\mu$W/RIU and power-intercept of 0.066 ± 0.002 $\mu W$ was also verified for normalized data obtaining a sensitivity of -1.27 ± 0.07 $RIU^{-1}$ with $R^2$ = 0.9876.

The second study involved spectral analysis by connecting the system to an OSA. The results are shown in Figure 3.21.

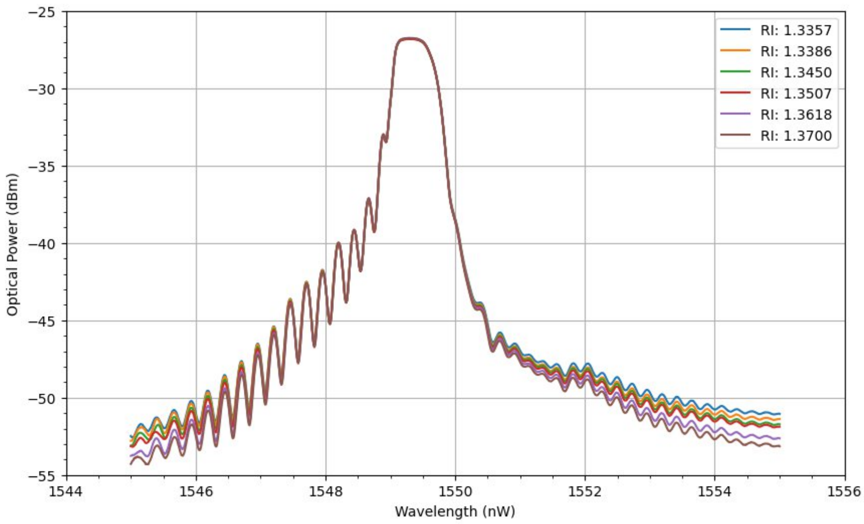


Figure 3.21: Spectral response of the FBG.

The obtained spectra exhibit the characteristic Bragg peak, with a maximum optical power in a wavelength range between 1549 nm and 1549.5 nm. On the left side of the spectra, features resembling interference fringes are visible, most likely caused by cladding modes coupling into the core. In terms of optical power response, the Bragg peak shows no sensitivity, whereas the fringes demonstrate increasing sensitivity with distance from the peak, as discussed in Appendix A.

Based on the findings in Appendix A, only the left side of the spectra was analyzed. A narrow spectral window between 1545.6 nm and 1545.8 nm was selected to isolate a single peak. The maximum optical power was identified in the spectrum corresponding to the lowest RI value, and the associated wavelength was recorded. This wavelength was then used to determine the reflected optical power for each spectrum.

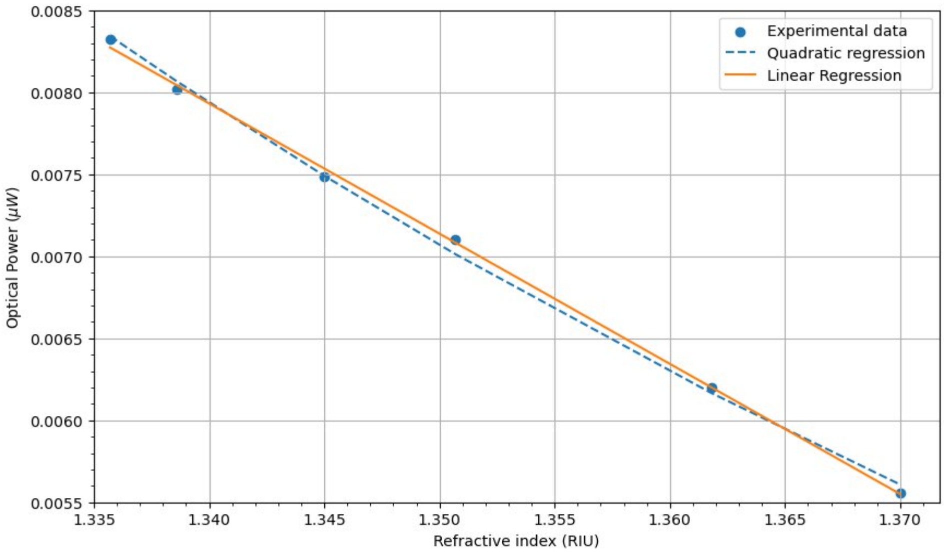


Figure 3.22: Optical power variation of the FBG-based tip sensor as a function of RI. Experimental data obtained with the OSA.

The linear regression, in Figure 3.22, reveals the sensitivity of the sensor, which was determined to be 0.079 ± 0.001 μW/RIU, with a power intercept of 0.115 ± 0.002 μW coefficient of determination $R^2$= 0.9990, for the normalized data it obtained a sensitivity of -9.5 ± 0.2 with a $R^2$= 0.9990.

## 3.8. Concluding Remarks

In this chapter, sensor heads made from SMF, step-index MMF, graded-index MMF, solid-core microstructured fiber, and FBG were studied. The general analysis of all fiber tips was conducted by measuring the integrated reflection optical power using the OPM. The results are presented in Table 3.11.

Table 3.11: Summary of the sensitivities attained with the OPM, and for the developed sensor heads.

| Sensors | Low RI range (RIU) | High RI range (RIU) |
|---|---|---|
| **SMF** | -42 ± 2 (5 %) | |
| **STEP-INDEX** | -10.4 ± 0.8 (8%) | -4.2 ± 0.2 (5%) |
| **GRADED INDEX** | -70 ± 10 (14%) | -22 ± 2 (9%) |
| **Microstructured** | -10 ± 2 (20%) | -4.46 ± 0.09 (2%) |
| **FBG** | -0.032 ± 0.002 (6%) | |

Based on the data, the most suitable sensor depends on the intended application. If the goal is to measure a wide range of RI, the best choice is the SMF sensor head, as it exhibits linear behavior across the range with high sensitivity, -42 μW/RIU, and a relatively small error of 2 (5%) μW/RIU.

For measurements in the lower RI range (up to 1.35 RIU), where large variations are expected, the graded-index fiber is the most appropriate. It offers the highest overall sensitivity, -70 μW/RIU, but also presents an error proportional to its scale. Conversely, if detecting very small changes is critical, the step-index fiber may be more suitable. Although its sensitivity is lower, it provides a small error of just 0.8 μW/RIU (8%).

In the higher RI range (1.35 to 1.37 RIU), the SMF sensor remains the best option for detecting large changes. However, for subtle variations, the microstructured fiber sensor head may yield better results due to its minimal error of 0.09 μW/RIU (2%).

On the other hand, if it is possible to use an OSA, it can also be used to obtain the reflected optical power, which generally reveals better sensitivity compared to the OPM. This is because the OPM detects light including noise in the reflected spectrum, which can be ignored in spectral analysis. The results are presented in Table 3.12, which does not include data from the SMF sensor.

Table 3.12: Summary of the sensitivities attained with the OSA, and for the developed sensor heads (excluding SMF sensor).

| Sensors | Low RI range (RIU) | High RI range (RIU) |
|---|---|---|
| **STEP-INDEX** | -1.3 ± 0.3 (23%) | -0.5 ± 0.05 (10%) |
| **GRADED INDEX** | -7.0 ± 1 (14%) | -2.32 ± 0.05 (2%) |
| **Microstructured** | -2.8 ± 0.5 (18%) | -1.19 ± 0.02 (2%) |
| **FBG** | -0.079 ± 0.001 (1%) | |

In this final section, it is shown that the measured values are generally comparable to those obtained using the OPM, apart from the microstructured fiber, which provided better overall results compared to the step-index fiber. This indicates that the microstructured fiber is highly sensitive to external factors such as curvature.

The last analysis focuses on spectral shifts due to variations in RI, which only occurs in the presence of multimodal interference. This phenomenon was observed exclusively in the step-index and microstructured fibers. For the step-index MMF, a sensitivity of 0.015 ± 0.002 RIU/nm was obtained for the lower RI range, and 0.025 ± 0.002 RIU/nm for the higher range. For the microstructured fiber, which operated in a linear configuration, the sensitivity was 0.0107 ± 0.0003 RIU/nm. The microstructured fiber proves to be a better sensor when measurements span a wide range.

Finally, caution is advised when working with microstructured fiber, as its internal holes tend to retain liquid, making it highly susceptible to hysteresis effects, as demonstrated in Appendix B.

# 4. Study of evaporation dynamics with optical fiber sensors

## 4.1. Introduction

Material characterization constitutes a fundamental aspect of contemporary science and technology, with applications extending across a wide spectrum of fields. A particularly relevant domain is quality control, which is indispensable in industries such as food, beverages, medicine, pharmaceuticals, petroleum, and several others [99].

A diverse set of analytical techniques has been employed for this purpose, including infrared spectroscopy [100], thermography [101], gas chromatography [102], ion flow tube mass spectrometry [103], as well as image processing methodologies designed to monitor the behavior of liquid droplets during evaporation [104-106].

OFS have emerged as highly promising tools, owing to their rapid response times and high-resolution capabilities [107]. Initially conceived as RI sensors, OFS have subsequently demonstrated considerable potential for the investigation of evaporation dynamics [99].

In this chapter, several studies were conducted to investigate evaporation dynamics using optical fiber sensors. Initially, a comparative analysis was performed to identify the most suitable sensor for evaporation monitoring. Three types of fibers were tested: SMF, Step-Index MMF, and microstructured fiber, using both water and isopropyl alcohol (IPA) as test liquids. A follow-up investigation using the microstructured fiber to assess the influence of initial fiber immersion depth and pulling velocity on the spectral response, focusing exclusively on water. Finally, a comprehensive study of evaporation dynamics was carried out using the step-index MMF for both water and isopropyl alcohol.

## 4.2. Evaporation techniques with optical fiber sensors

When employing a fiber tip as an evaporation dynamics sensor, a liquid droplet is deposited on the fiber end face. As light propagates through the fiber and reaches the fiber–liquid interface, it undergoes partial reflection and transmission in accordance with Fresnel's laws. The transmitted portion enters the liquid and, upon reaching the liquid–air interface, a fraction is reflected into the liquid and subsequently re-coupled into the fiber, as illustrated in Figure 4.1.

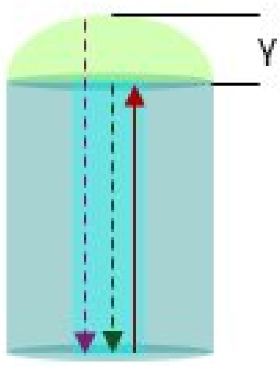


Figure 4.1: Representation of a liquid droplet on a fiber tip. The incident ray (red) is partially reflected at the fiber–liquid interface, forming the green reflected ray. Another portion of the light is transmitted into the droplet, where it reflects at the liquid–air interface (dark red ray) and returns to the fiber. Inside the fiber, the green and yellow rays interfere. This interference can be constructive or destructive, depending on the droplet thickness, γ.

Within the fiber, the beams resulting from the first and second reflections interfere. Depending on the droplet thickness, this interference may be constructive or destructive, generating a pattern analogous to that of a FFPI.

When analyzing the interference pattern, the phase change between two fringe maxima is considered. This phase shift is associated with a change in the thickness of the droplet, as described by Equation (4.1).

$$\Delta\gamma = \frac{\lambda}{2n_{liq}} \tag{4.1}$$

$\Delta\gamma$ represents the change in droplet thickness, $\lambda$ is the free-space wavelength, and $n_{liq}$ denotes the refractive index of the liquid analyte [99].

This approach assumes quasi-state evaporation, a linear relationship between the droplet thickness and a unidimensional equivalent to evaporation rate over time (Ω), shortened only to evaporation rate, possible to apply when there is a small radius of curvature and light ray has a radius sufficiently small to not detect differences in curvature, as shown in Equation (4.2).

$$\gamma(t) \propto -\Omega t \tag{4.2}$$

Rearranging Equation (4.2), it’s possible to calculate evaporation rate [108] as follows:

$$\Omega = -\frac{\Delta\gamma}{\Delta \mathrm{t}} = -\Delta\gamma \times \nu \tag{4.3}$$

where $\nu$ represents the frequency of the change in the cavity [108]. This equation allows for straightforward calculation of the evaporation rate when the frequency is extracted using a Fast Fourier Transform (FFT). In the case of a pure liquid, only one evaporation rate is expected. This technique also enables the identification of different components within a mixture.

Considering external factors, such as movements of the fiber tip, the evaporation rate may vary over time. To study this behavior, the electromagnetic wave resulting from the interference of the two reflected rays (illustrated in Figure 4.1) can be modeled as the sum of the phases of both rays, as described in Equation (4.4).

$$y_{int} = Asin\left(\theta(t) + \theta(t-\tau) + \theta_0\right) \quad (4.4)$$

The parameter *θ(t)* represents the phase of the signal reflected at the surface of the fiber tip, while $\theta\,(t-\tau)$ corresponds to the phase of the signal reflected at the surface of the droplet. $\theta_0$ is the constant phase of the signal, and *A* is its amplitude [108].

To determine the instantaneous phase of this signal, a Hilbert transform is applied. This operation introduces a phase shift of $\pi/2$ to the original signal. By contracting the phase notation to Θ (t), the signal after applying the Hilbert transform becomes [108]:

$$H(y_{int}) = Acos\left(\Theta(t)\right) \quad (4.5)$$

allowing the following [108]:

$$\Theta(t) = arctan\left(\frac{y_{int}}{H(y_{int})}\right) = kn_{liq}2\gamma(t) = \frac{4\pi}{\lambda}n_{liq}\gamma(t) \quad (4.6)$$

where *k* is the propagation constant in the fiber, and γ(t) represents the instantaneous thickness of the droplet.

The phase presented in Equation (4.6) allows the use of an alternative version of Equation (4.3) to determine the unidimensional equivalent to instantaneous evaporation rate, as described in Equation (4.7) [108].

$$\Omega(t) = -\frac{\partial\gamma}{\partial t} = -\frac{\lambda}{4\pi n_{liq}}\frac{d\Theta(t)}{dt} \quad (4.7)$$

Given that the instantaneous thickness of the droplet is known, its mass can also be estimated. For this calculation, it is assumed that droplets formed at the fiber tip have a hemispherical shape. The volume is then multiplied by the liquid’s density, resulting in the expression shown in Equation (4.8).

$$M(t) = \frac{2\pi}{3}\rho_{liq}[\gamma(t)]^3 \tag{4.8}$$

where $\rho_{liq}$ is the density of the measured liquid [108]. To obtain the initial droplet's mass, the most practical approach is to average the evaporation rate values, Equation (4.9).

$$M = \frac{2\pi}{3}\rho_{liq}[T\Omega]^3 \tag{4.9}$$

Ω is the mean evaporation rate and T is the total evaporation time; this multiplication forms the initial droplet's thickness [108].

### 4.2.1. Evaporation study sensors

Several fiber architectures have been developed to study evaporation dynamics. Most of the studies use SMF, they put a droplet at the tip as described [99,108]. Microstructured fiber also takes its place using and several architectures are used, for example a caterpillar-like microstructured fiber [109] and with doped cladding [110]. Another example found is an evaporation sensor made with suspended-core optical fibers, a fiber with nanowire-like cores inside an air hole [111].

## 4.3. Experimental apparatus and methodology

In this experiment, two different setups were used. The first consists of an Erbium-Doped Source (Photonetics 3627 IN), which acts as a broadband source, a 50:50 coupler, and a sensor head connected to the coupler coupler arm, and the OSA (Yokogawa AQ6370C) connected to the other output arm, see Figure 4.2a).

The second setup includes a wavelength-tunable laser (Thorlabs TL200C) set to 1550.12 nm, a 50:50 coupler, a sensor head spliced to the coupler output arm, and a photodetector (Thorlabs PDA10CS-EC) connected to an oscilloscope (GW INSTEK GDS-2304A) in the other arm, see Figure 4.2b). In both setups, a motorized stage was used to move the sensor head up and down.

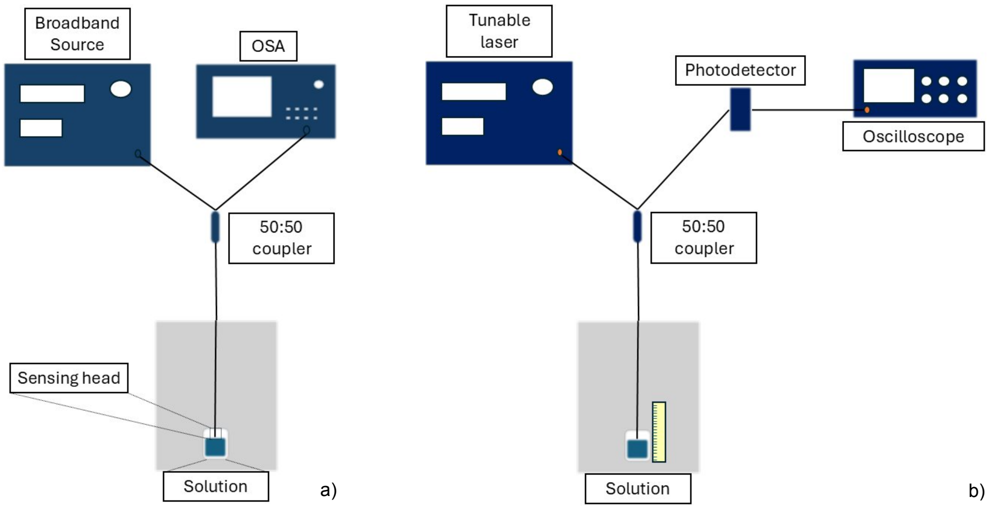


Figure 4.2: Schematics of the experimental setup used to study evaporation dynamics: a) with an OPM, and b) an OSA.

The experiment was divided into two main parts:

In the first part, the objective was to identify the most suitable sensor for studying evaporation dynamics. The OSA was configured to High 1 sensitivity, with a resolution of 0.5 nm. Averaging was adjusted throughout the process to fine-tune the sweep timing. The sensor head was then coupled to the apparatus, and the fiber was cut to ensure sufficient reflected optical power. Using this setup, the fiber tip was immersed in a liquid: either water or IPA. This procedure was performed once for each sensor head. Immersion depths and raising velocities were randomly selected. Prior to each measurement, the RI of the liquid was measured using a refractometer (ATAGO DR-A1).

The second part focused on investigating the factors influencing evaporation dynamics. A microstructured fiber with arbitrary length was used to control the reflected optical power. Specific immersion depths were selected: 0.5, 1.0, 1.3, 1.5, 1.7, 2.0, and 2.2 cm. For each depth, the following velocities were applied: 1.007, 1.497, 1.998, and 2.506 mm/s. Each experimental condition was repeated twice to ensure repeatability. The photodetector was configured to operate within a range of approximately 10-20 dB. Water was used as the liquid solution throughout this phase.

## 4.4. Evaporation measurements

The first sensor analyzed is the SMF (SMF 28) sensor head. The temporal change of the reflected power is in Figure 4.3 and is divided into four distinct regions.

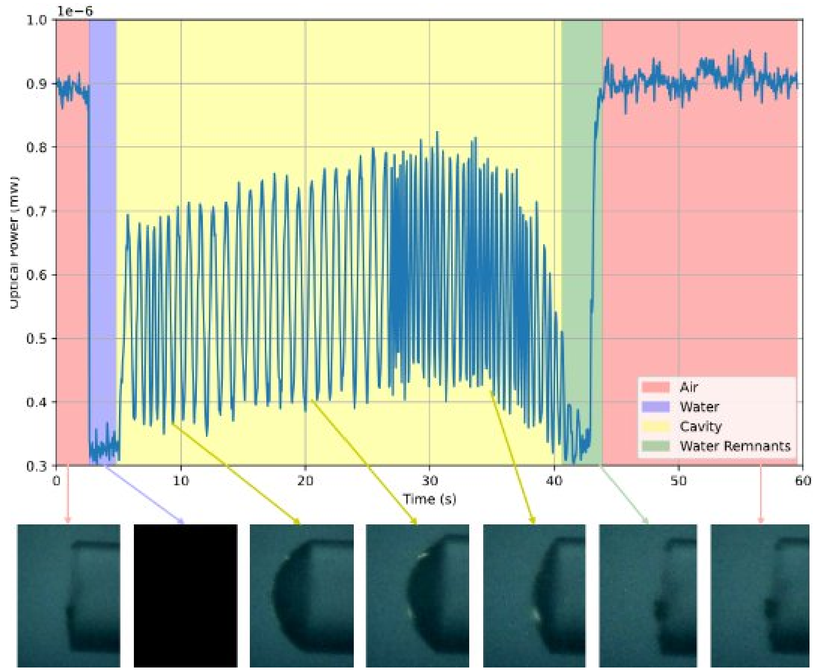


Figure 4.3: Reflected power variation of the SMF-tip sensor in water, divided into four zones: red for air readings; purple for submerged fiber, where the optical power significantly lowers due to the RI increase of the surrounding medium; yellow for visible FP cavity formation as the water droplet is present at the fiber tip; green for the residual water that remains at the fiber tip although no cavity is visible in microscopic images. Final red section is related to the reflected power when there's no cavity.

The first region corresponds to a stable phase where the fiber is in contact with air (red). The second region (purple) represents another stable phase, this time with the fiber submerged in water where the optical power significantly lowers due to the RI increase of the surrounding medium (from air to water). The third region (yellow) occurs when a water droplet is present at the fiber tip, producing a low-finesse Fabry-Pérot-like behavior. The fourth region (green) indicates the presence of water remnants, although no cavity is visible in microscopic images, residual water remains at the fiber tip. Finally, the system returns to the initial state when the fiber tip loses the liquid droplet, and it gets in full contact with air (red).

An analogous analysis was performed using a solution of IPA (Figure 4.4). The graph was also divided into the same four regions, although no images are presented for these zones, as they closely resemble each other.

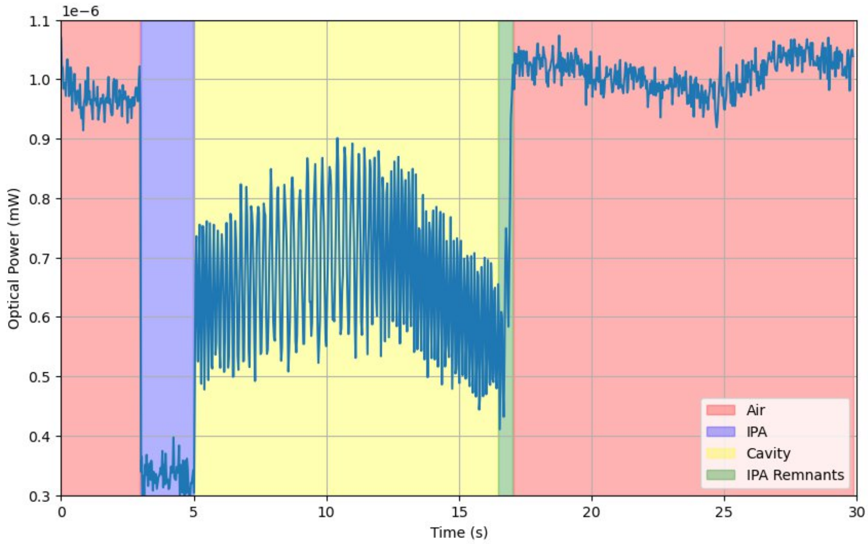


Figure 4.4: Reflected power variation of the SMF-tip sensor in IPA, divided into four zones: red for air readings; purple for submerged fiber, where the optical power significantly lowers due to the RI increase of the surrounding medium; yellow for visible FP cavity formation as the water droplet is present at the fiber tip; green for the residual water that remains at the fiber tip although no cavity is visible in microscopic images. Final red section is related to the reflected power when there's no cavity.

To assess the impact of noise on the signal, a FFT was performed in the cavity region for both solutions: Figure 4.5 for a) water and b) IPA, respectively.

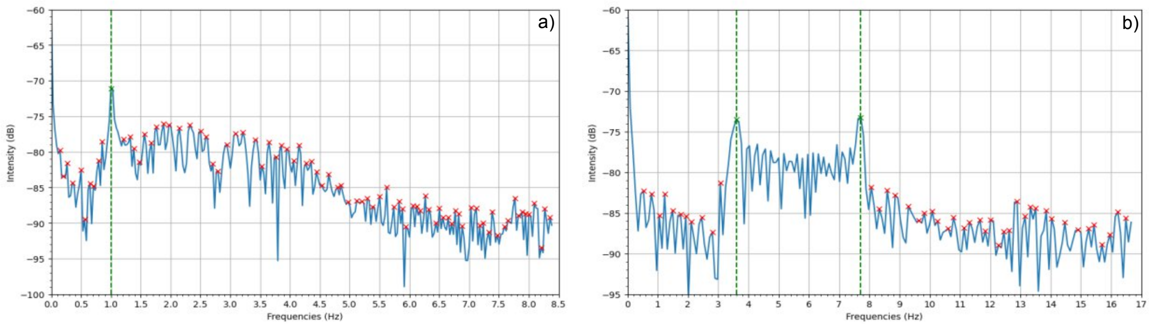


Figure 4.5: FFT of the data from the SMF-tip sensor submerged in a) water and b) IPA. Red crosses indicate noise peaks, and the dashed green line represent the data peaks.

In Figure 4.5a), only one peak is observed, with the remaining components treated as noise. In Figure 4.5b), two prominent peaks are present, these are the analyzed peaks, while additional components between them are considered instantaneous variations in the cavity thickness variation's frequency. Outside this region, specifically beyond 3.6 Hz and 7.7 Hz, all other peaks are classified as noise.

For both datasets, the difference between each signal peak and the surrounding noise peaks was measured. The median value, chosen for its robustness against outliers, was calculated. In cases where more than one signal peak was present, the mean value of the calculated medians was used. For water, the difference between signal and noise peaks was 13.9 dB, while for IPA, it was 12.7 dB.

The second sensor analyzed is the Step-Index MMF (FG105LCA, Thorlabs). Measurements were conducted using both water (Figure 4.6) and IPA (Figure 4.7), respectively.

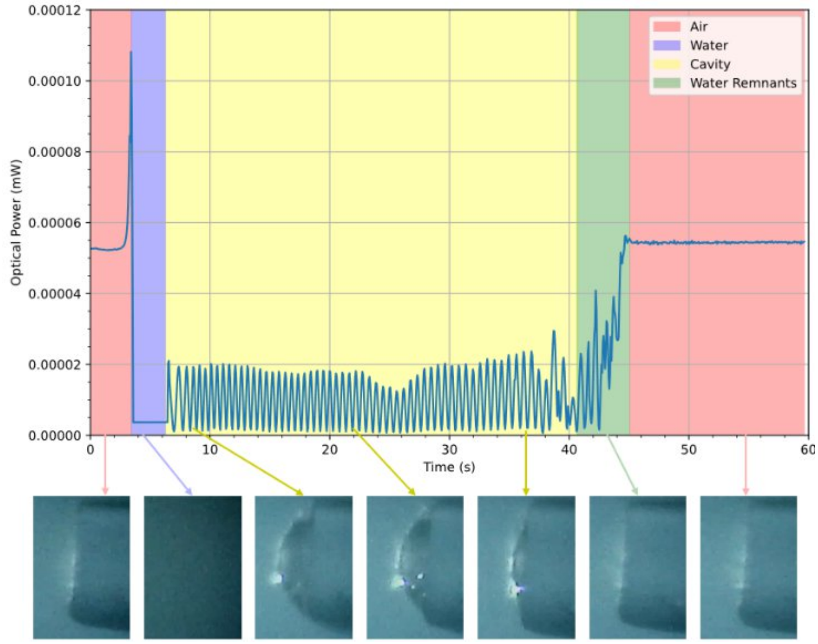


Figure 4.6: Reflected power variation of the step-index MMF-tip sensor in water, divided into four zones: red for air readings; purple for submerged fiber, where the optical power significantly lowers due to the RI increase of the surrounding medium; yellow for visible FP cavity formation as the water droplet is present at the fiber tip; green for the residual water that remains at the fiber tip although no cavity is visible in microscopic images. Final red section is related to the reflected power when there’s no cavity.

Figure 4.6 represents reflected power temporal variation during water measurements. It is divided into four regions: the red region corresponds to a stable state where the fiber tip is in contact only with air; the second region occurs when the fiber is submerged in water, resulting in a change in optical power due to Fresnel reflection coefficients. The third region appears when the fiber is lifted from the water and only a droplet remains, this phase displays a series of fringes. The fourth region occurs when no cavity is visible in microscopic images, yet the reflected optical power remains lower than in air, and some fringes persist, possibly due to external factors such as motor noise.

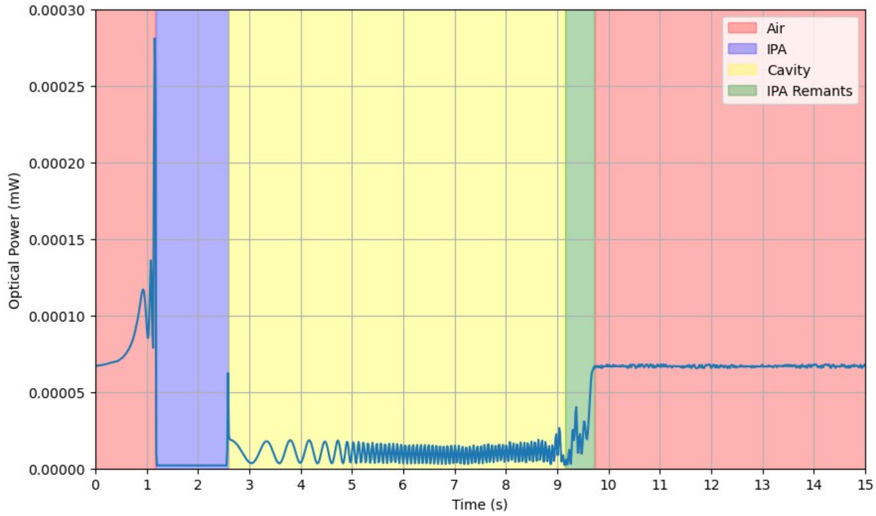


Figure 4.7: Reflected power variation of the step-index MMF-tip sensor in IPA, divided into four zones: red for air readings; purple for submerged fiber, where the optical power significantly lowers due to the RI increase of the surrounding medium; yellow for visible FP cavity formation as the water droplet is present at the fiber tip; green for the residual water that remains at the fiber tip although no cavity is visible in microscopic images. Final red section is related to the reflected power when there's no cavity.

Figure 4.7 is also divided into distinct regions: the stable air region, the stable IPA region, the cavity region where a droplet is present at the fiber tip, and the region with non-visible IPA remnants.

A portion of the cavity power variation was selected after the first peak, corresponding to the interval where the fiber tip is out of the liquid until the last major maximum. Beyond this point, the results become unstable. This instability may be attributed to the fiber's higher susceptibility to external influences such as bending and motor vibrations.

Figure 4.8a) shows the FFT spectrum obtained from the water dataset. Three major peaks are visible and considered true evaporation signals, marked with green crosses and vertical lines. Additional peaks, marked with red crosses, are classified as noise. For each signal peak (green cross), the intensity difference relative to the noise spectrum was measured. The median of all differences was calculated, and since multiple signal peaks were present, the mean value of these medians was used. The result obtained is 17.8 dB.

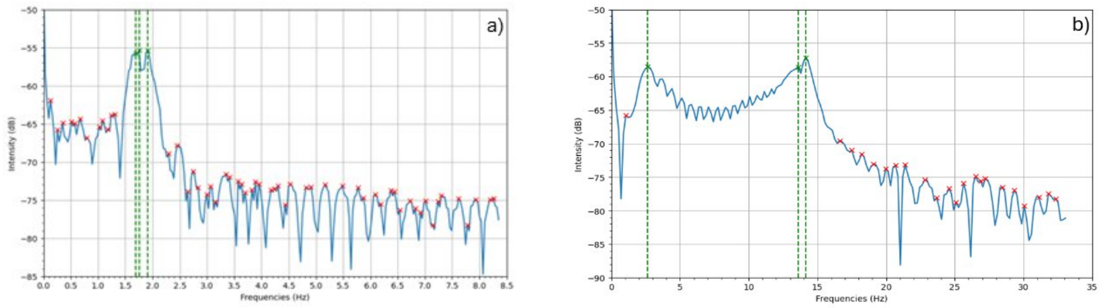


Figure 4.8: FFT of the data from the step-index MMF-tip sensor submerged in a) water and b) IPA. Red crosses indicate noise peaks, and the dashed green line represent the data peaks.

Figure 4.8b), the FFT of the IPA spectrum is presented. Like the case with the SMF, two major peaks are observed, along with several minor peaks between them, which are considered to represent variations in the spectrum's wavelength. Peaks outside the range of approximately 2.5 to 16 Hz are classified as noise. Three data peaks were analyzed, including the one at approximately 13.5 Hz, which has an amplitude comparable to the major peaks. The result obtained is 17.4 dB.

The third sensor analyzed is the microstructured fiber tip (184b3a, IPHT), for which measurements were conducted using both water and IPA. The power change with time resulting from evaporation of water is shown in Figure 4.9.

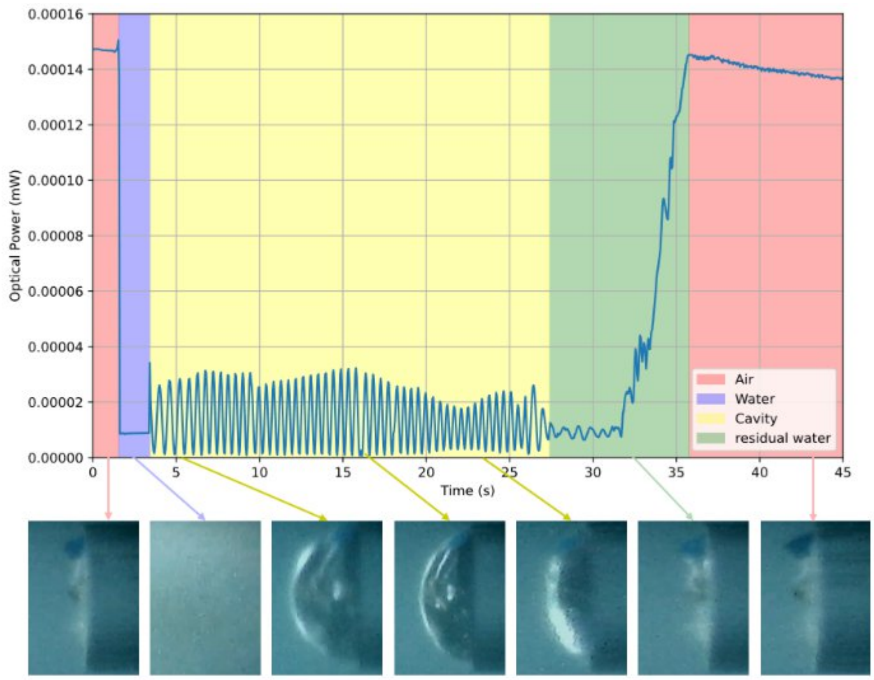


Figure 4.9: Reflected power variation of the microstructured fiber-tip sensor in water, divided into four zones: red for air readings; purple for submerged fiber, where the optical power significantly lowers due to the RI increase of the surrounding medium; yellow for visible FP cavity formation as the water droplet is present at the fiber tip; green for the residual water that remains at the fiber tip although no cavity is visible in microscopic images. Final red section is related to the reflected power when there's no cavity.

Similar to the previously analyzed sensors, the reflected power variation can be divided into four distinct regions. The **red region** corresponds to the period when the fiber is in contact only with air. The **purple region** represents the interval during which the fiber is submerged in water. The **yellow region** indicates the moment when the fiber is removed from the liquid but still retains a droplet at its tip. Finally, the **green region** denotes the presence of residual water. In this last region, a stable signal is observed as the remaining liquid penetrates the fiber's microstructures even after the droplet has visually disappeared.

The same data acquisition and processing procedure was applied to IPA. The reflected temporal graph is shown in Figure 4.10, and the same four regions were defined using the same criteria: the red region corresponds to the fiber tip in contact with air; the purple region represents the submerged state in IPA; the yellow region indicates the presence of a droplet at the fiber tip; and the green region reflects the phase where IPA remnants remain, even though the droplet is no longer visible.

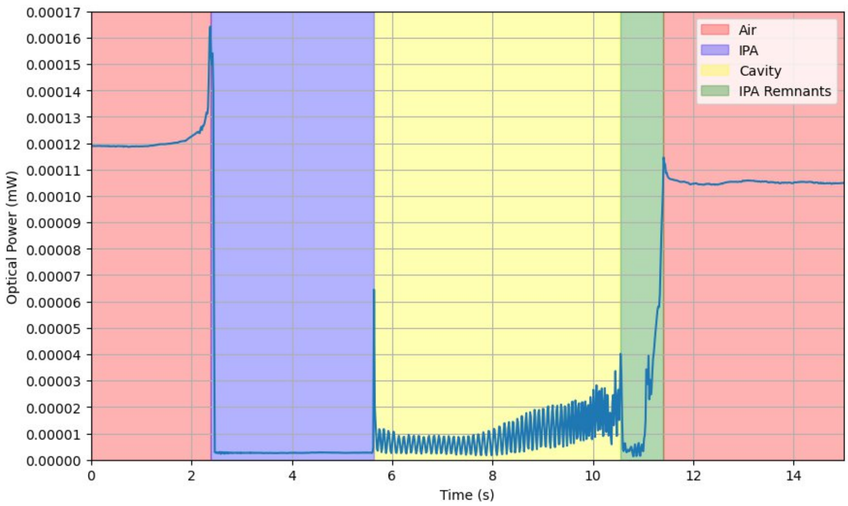


Figure 4.10: Reflected power variation of the microstructured fiber-tip sensor in IPA, divided into four zones: red for air readings; purple for submerged fiber, where the optical power significantly lowers due to the RI increase of the surrounding medium; yellow for visible FP cavity formation as the water droplet is present at the fiber tip; green for the residual water that remains at the fiber tip although no cavity is visible in microscopic images. Final red section is related to the reflected power when there's no cavity.

To perform the FFT, a portion of the cavity region was selected: from the second peak to the last largest peak for water, and from the second peak to the second highest peak for IPA. The FFT results for the water spectrum are shown in Figure 4.11a). In this spectrum, a prominent peak is visible, like that observed in the SMF spectrum, along with two additional large peaks surrounding it. These three peaks are considered signal and are marked with green crosses and vertical lines.

An analysis similar to the previous cases was conducted. To compare the intensity of each signal peak with the noise peaks, the median of the differences was calculated. Since three signal peaks were present, the mean value of the three medians was used. The result obtained is 19.4 dB.

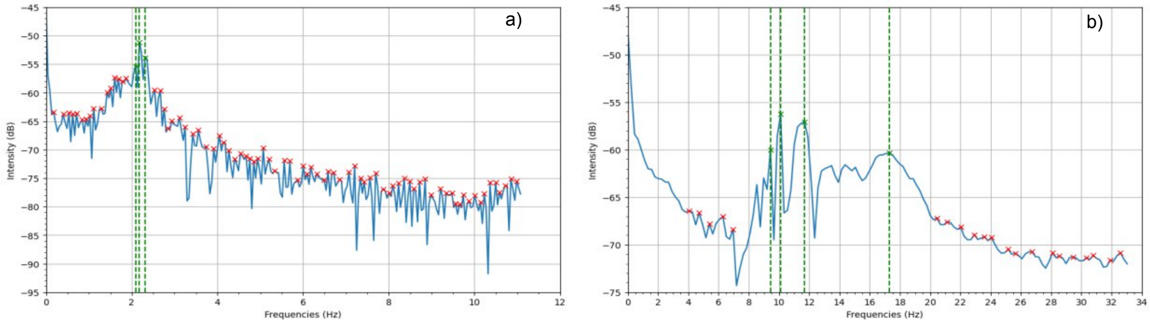


Figure 4.11: FFT of the data from the microstructured fiber-tip sensor submerged in a) water and b) IPA. Red crosses indicate noise peaks, and the dashed green line represent the data peaks.

Figure 4.11b) presents the FFT of the cavity temporal variation for IPA. Unlike the previous two cases, the signal spectrum does not display two major peaks with smaller peaks between them. However, within the range of 8 to 18 Hz, several peaks are identified as signal peaks, while the remaining ones are classified as noise.

The four analyzed signal peaks are marked with green crosses and vertical lines, and the noise peaks are marked with red crosses. Applying the same analysis method as before, the final value obtained is 10.8 dB.

While performing the task, it was observed that some occurrences did not go as expected, for example for a 1.5cm-depth and a pulling velocity of 1.5 mm/s presented in Figure 4.12a), whereas others were more successful, such as 2.2 cm-depth and pulling velocity of 2 mm/s presented in Figure 4.12b).

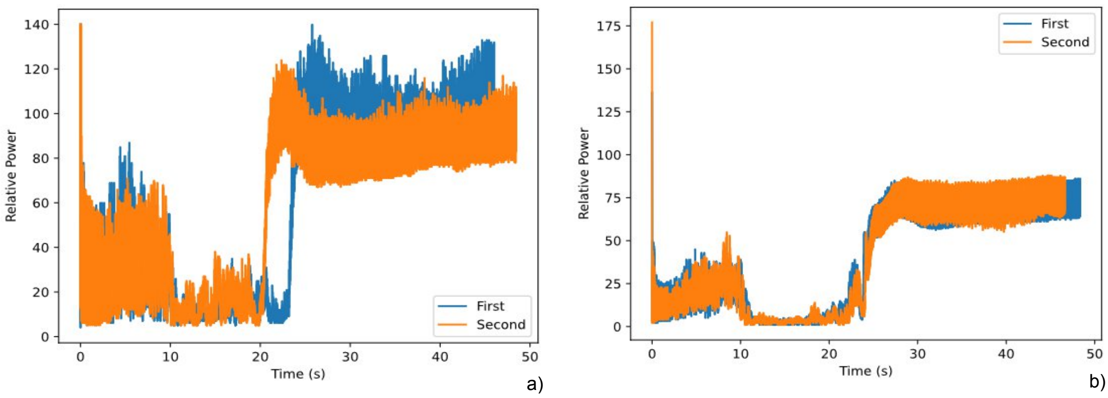


Figure 4.12: Comparative reflected power temporal variation of the microstructured fiber-tip sensor for a) 1.5 cm-depth and 1.5 mm/s pulling velocity; b) for 2.2 cm-depth and 2 mm/s pulling velocity.

For each data point, three parameters were measured. First, the time interval from the first major peak to the last prominent peak just before reaching a stable state was recorded. Then, a FFT was performed in a manner analogous to the sensor study, and the frequency of the most intense peak was identified.

To analyze the data, the mean value of points within each set of depth and velocity was calculated. It was initially expected that greater immersion depth would result in a larger droplet and, consequently, a longer evaporation time. However, this trend could not be fully confirmed by the data, likely due to inaccuracies in depth measurement. As a result, the mean value across all depths was used to investigate the general behavior of evaporation time as a function of pulling velocity, as shown in Figure 4.13.

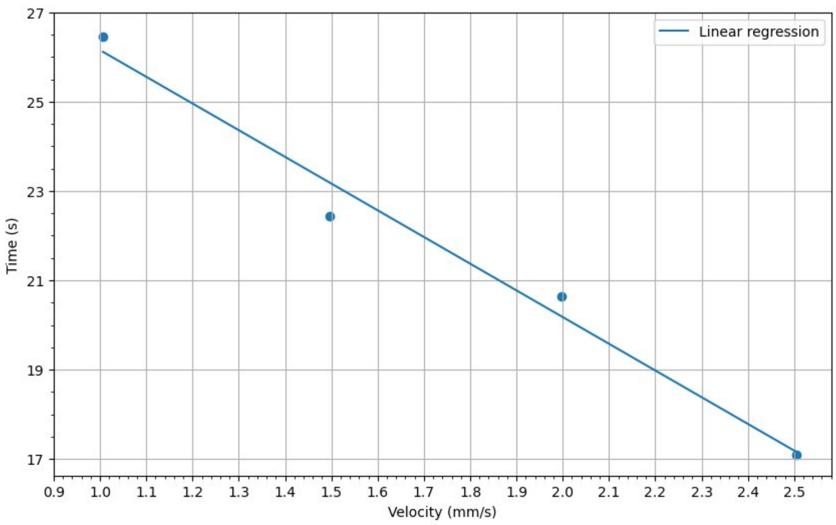


Figure 4.13: Dependence of the pulling velocity with time.

As expected, the evaporation time decreases as the pulling velocity increases. A linear regression was performed, yielding a rate of change of −6.0±0.6 $s^2/mm$ with a coefficient of determination $R^2$=0.9803.

A similar analysis was conducted using the maximum velocity, this time associating it with the evaporation rate via Equation (4.3). The resulting graph, shown in Figure 4.14, shows a rising trend, indicating that the evaporation rate increases with pulling velocity. A linear regression was also applied, producing a rate of change of 0.145 ± 0.006 $\mu m/mm$ with $R^2$=0.9962.

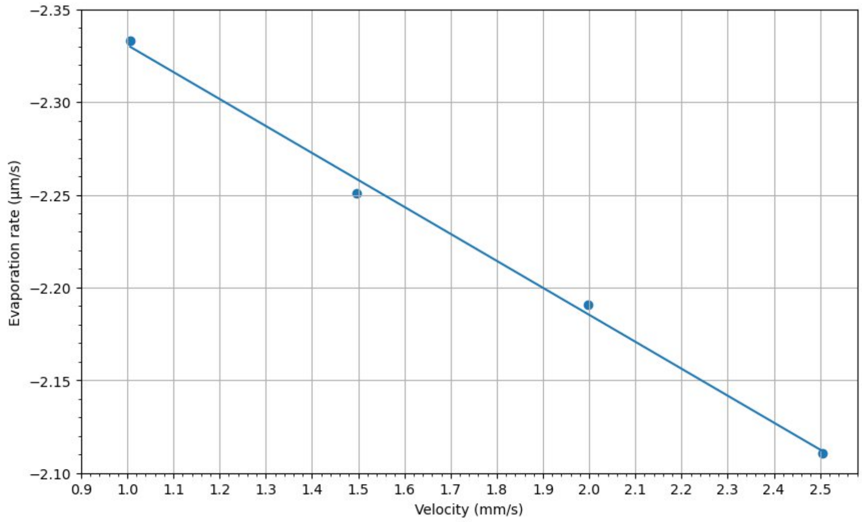


Figure 4.14: Dependence of the pulling velocity with evaporation rate.

## 4.5. Study of the evaporation dynamics

To study evaporation dynamics, the Step-Index MMF-tip sensor temporal graph was selected for both water and IPA, focusing on the same portion as presented in the first part of this chapter. Their corresponding FFT spectra is depicted in Figure 4.15.

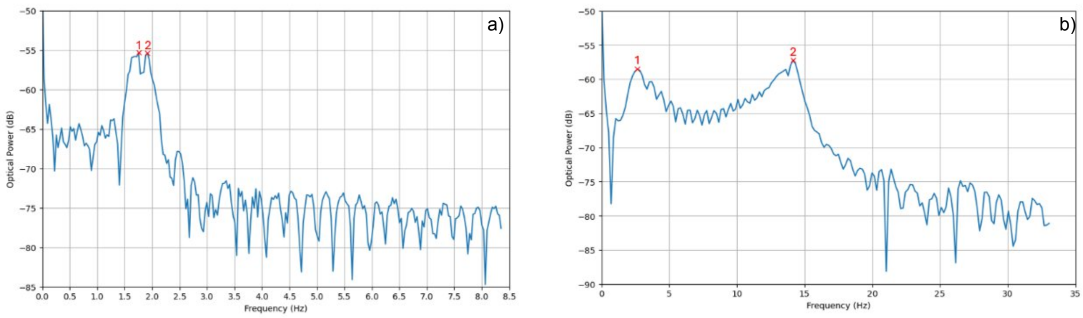


Figure 4.15: FFT of the data from the step-index MMF-tip sensor submerged in a) water and b) IPA. In each spectrum, two well defined peaks are identified in red.

By examining FFT spectra, clear differences between water and IPA can be observed. In Figure 4.15a), the spectrum, resultant from the MMF-tip sensor submerged in water, presents a narrow cluster of peaks within a small frequency range, with the major peak located at approximately 2 Hz. In contrast, the FFT spectrum in Figure 4.15b), resultant from the MMF-tip sensor submerged in IPA, displays a broader range of peaks, which may be interpreted as fluctuations in the evaporation frequency, along with two prominent peaks characteristic of this liquid.

Therefore, peak (1) from Figure 4.15a) appears at 1.7535 Hz. Using Equation (4.3) and the refractive indices $n_{water}$ = 1.3348 RIU and $n_{IPA}$ = 1.3755 RIU, the corresponding evaporation rate is −1.0037 µm/s. Peak (2) from Figure 4.15a)is located at 1.9128 Hz, yielding an evaporation rate of −1.0949 µm/s. Applying the same method to the two major peaks found in Figure 4.15b), peak (1) is at 2.6516 Hz and corresponds to an evaporation rate of −1.4728 µm/s; while peak (2), at 14.1420 Hz, corresponds to an evaporation rate of −7.8550 µm/s.

To determine the instantaneous evaporation rate, Equation (4.7) was applied. Prior to this, the Hilbert transform was performed on the selected portion of the graph. The resulting plot also includes evaporation rates calculated via the FFT. For both plots, the frequency associated with the major peak, especially in the case of IPA, corresponds to the region where the data is most densely concentrated.

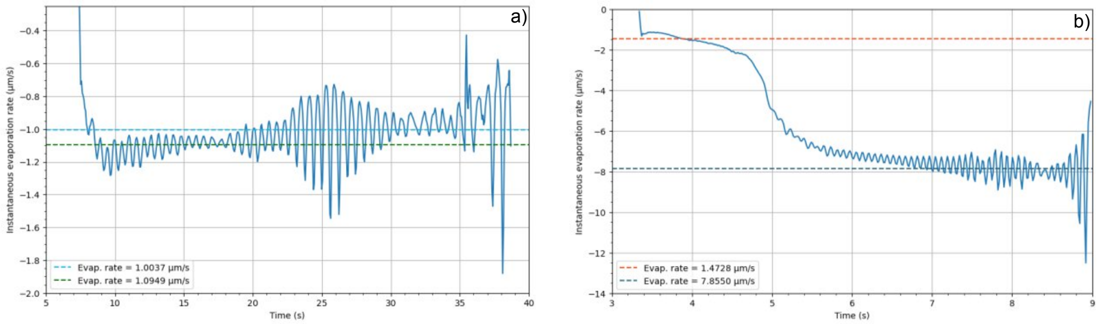


Figure 4.16: Instantaneous evaporation rate of the a) water and b) IPA droplets.

Using Equation (4.9), it is possible to estimate both the initial droplet thickness and initial mass. First, the mean value of the instantaneous evaporation rates was determined, resulting in −1.0212 µm/s for water and −7.8550 µm/s for IPA. The total evaporation time was defined as the interval from the first major peak, marking the beginning of the cavity, until the end of the cavity remnants. Based on this, the initial droplet thickness was calculated to be 39.52 µm for water and 41.23 µm for IPA.

To calculate the initial mass, the density values for water and IPA at room temperature (25 °C) were used: $9.9713 \times 10^{-7}$ µg/µm³ for water [112] and $7.808 \times 10^{-7}$ µg/µm³ for IPA [113]. Based on these values, the resulting initial mass was 0.1289 µg for water and 0.1147 µg for IPA.

## 4.6. Concluding remarks

In this chapter, several fiber sensors were evaluated: SMF, Step-Index MMF, and microstructured fiber. To determine the most suitable sensor, the FFT graph was analyzed by separating signal and noise peaks. For each signal peak, the intensity difference in dB between it and each noise peak was measured. The median of these differences was calculated, and the mean of all medians, one per signal peak, was determined. The resulting data is presented in Table 4.1.

Based on these values, the Step-Index MMF proved to be the most effective for distinguishing between different liquids. It provided the greatest separation between signal and noise, clearly visible in the graphs, and allowed for precise identification of major peaks along with minor deviations. The microstructured fiber-tip sensor performed well for water detection, showing three major peaks, including one matching the dominant water peak. However, it was less effective for IPA, as its spectrum did not resemble those of the other two sensors, making it difficult to identify major peaks. Additionally, it exhibited the smallest difference between signal and noise peaks.

| Sensors | WATER (dB) | IPA (dB) |
|---|---|---|
| **SMF** | 13.9 | 12.7 |
| **STEP-INDEX** | 17.8 | 17.4 |
| **Microstructured** | 19.4 | 10.8 |

Table 4.1: Values of the calculated separation between signal and noise peaks for each sensor head used for both water and IPA.

In the second section, a study was conducted to evaluate how pulling velocity influences evaporation time and evaporation rate. It was confirmed that higher pulling velocities lead to shorter evaporation times and higher evaporation rates. Specifically, evaporation time decreased at a rate of −6.0 $s^2/\mathrm{mm}$, while the evaporation rate increased at 0.145 μm/mm.

Subsequently, a comprehensive evaporation analysis was performed using data from the Step-Index MMF. Two evaporation rates were obtained via the FFT method for each liquid: −1.0037 μm/s and −1.0949 μm/s for water, and −1.4728 μm/s and −7.8550 μm/s for IPA. Instantaneous evaporation rates were also calculated, revealing that the most intense peak in the FFT corresponds to the most pronounced evaporation rate.

Finally, an approximation of the initial droplet thickness and mass was provided. For water, the thickness was 39.52 μm and the mass was 0.1289 μg; for IPA, the thickness was 41.23 μm and the mass was 0.1147 μg.

In summary, the Step-Index MMF was identified as the most effective sensor among those tested. It was confirmed that pulling velocity inversely affects evaporation time and directly increases evaporation rate. A complete study of evaporation dynamics was successfully carried out.

# 5. New microstructured fiber simulations

## 5.1. Introduction

A microstructured fiber is a novel design of optical fiber introduced by Russell in 1996 [31]. This fiber is characterized by the presence of longitudinal holes that extend along its entire length. Microstructured fibers are classified based on the mechanism by which light propagates through them.

The first type guides light via TIR. In this configuration, the fiber has a solid core (Figure 5.1a) surrounded by air holes. Compared to conventional fibers, this structure offers a higher effective index contrast, enhancing light confinement. Two key parameters used to analyze this fiber type are the hole diameter, *d*, and the pitch, Λ, which is the distance between the centers of two adjacent holes.

The second type guides light through a photonic bandgap mechanism (Figure 5.1b). This fiber features a hollow core, with pure silica or silica containing smaller holes forming the cladding. This arrangement forces light to propagate through a lower-index medium [114,115].

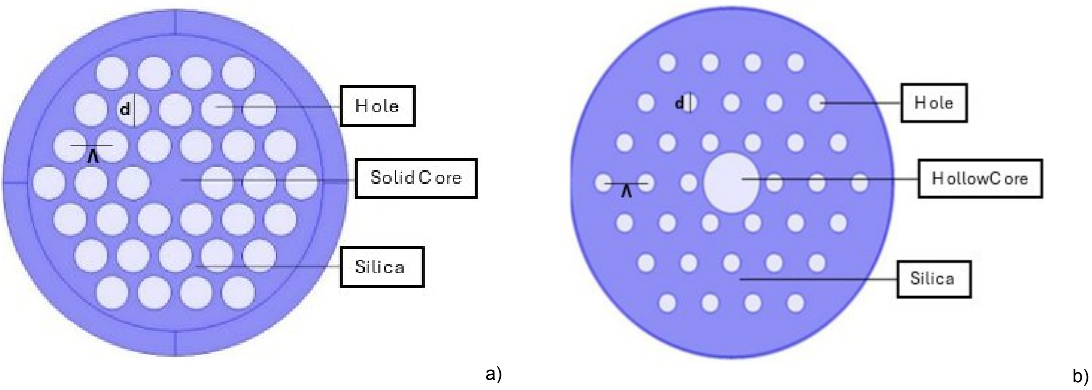


Figure 5.1: a) Solid core and b) hollow core.

In this chapter, several simulations were conducted on a novel rectangular-shaped solid-core microstructured fiber designed for high modal area applications. The simulations were performed using the commercial software COMSOL Multiphysics 6.2. Initially, modal analysis was carried out on a fiber. To project the best fiber configuration of core width and pitch and performance with wavelength. There were calculated modes for several configurations calculating modal area and confinement loss.

## 5.2. Modeling and simulation

To calculate propagation modes, the first step is to look at Maxwell's equations [116]:

$$\nabla \cdot \mathrm{E} = \frac{\rho}{\epsilon_0} \tag{5.1}$$

$$\nabla \cdot \mathrm{B} = 0 \tag{5.2}$$

$$\nabla \times E = -\frac{\partial H}{\partial t} \tag{5.3}$$

$$\nabla \times B = \mu_0\, \varepsilon_0\, J + \mu_0\, \varepsilon_0\, \frac{\partial E}{\partial t} \tag{5.4}$$

In these equations, E represents the electric field, which can be defined as $(P - D)/_{\epsilon_0}$, where *D* is the dielectric displacement and *P* is the polarization vector. The polarization vector is composed of two components: linear and non-linear. Here, $\varepsilon_0$ denotes the vacuum permittivity. *B* is the magnetic induction, defined as $B = \mu_0 H$, where *H* is the magnetic field and $\mu_0$ is the vacuum permeability. Additionally, $\rho$ represents the charge density, and $J$ is the current density [115].

Considering a medium free of electrical charges and currents, and neglecting non-linear polarization, equations Equation (5.3) and Equation (5.4) can be reformulated in terms of the magnetic field rather than magnetic induction. The resulting equations are:

$$\nabla \times E = -i\omega\mu_0 H = 0 \tag{5.5}$$

$$\nabla \times H + i\omega\epsilon E = 0 \tag{5.6}$$

where $\omega$ is the angular frequency and $\varepsilon$ is a general permittivity, resultant from the multiplication of vacuum permittivity and relative permittivity [115]. Using Equations (5.5) and (5.6), it's possible to obtain the following equation [115]:

$$\nabla \times \left( \frac{1}{n^2(\lambda,p)} \times H(\lambda,p) \right) = k_0^2 H(\lambda,p) \tag{5.7}$$

where $k_0$ is the vacuum wavenumber and *n* is the refractive index [115]. To solve Equation (5.7), it's possible to describe the magnetic field in the form: $H$ = $(x,y)$exp($i\beta z$). This method enables the calculation of the guided modes and their properties. $\beta$ is the propagation constant, and it allows obtaining the effective refractive index for each mode $n_{eff}$ = $\beta k_0$ [115].

Each mode presents a certain parameter named effective modal area, i.e., is the effective area of the core for each mode and it is given by the following formula [114]:

$$A_{effect} = \frac{\left(\int\int dxdy\,|E(x,y)^2\,|\right)^2}{\int\int dxdy\,\left|E\,(x,y)\right|^4} \quad (5.8)$$

Another important parameter when considering microstructured fibers, is the confinement loss. This parameter rises from the fact that the cladding equivalent is made of a finite number of air hole layers, some light tends to escape from these air hole layers and go outside, this behavior is more prevalent to higher order modes, since they tend to be less confined at the core. Confinement loss is the total loss in this leakage. This parameter is dependent on the imaginary part of the effective RI, as presented in the following formula [114]:

$$C.F = \frac{40\,\pi}{ln\,(10)\,\lambda}\beth\left(n_{eff}\right) \quad (5.9)$$

To solve Equation (5.7) and obtain the modal profiles as well as the modal effective area for each mode, the commercial simulation software COMSOL Multiphysics was employed [117].

COMSOL Multiphysics is a versatile simulation platform that enables the modeling and design of materials and processes across various domains, including structural mechanics, heat transfer, acoustics, electromagnetic fields, and chemical reactions. It relies on the numerical analysis of physical differential equations using the finite element method (FEM).

FEM is a computational technique that transforms complex partial differential equations into a system of geometric equations that are more tractable. In essence, a material with a complex geometry is divided into many small subdomains called finite elements, a process known as meshing. For each finite element, an ansatz (a trial solution) is defined, considering the boundary conditions of the entire system. The resulting matrix system is constructed to incorporate the influence of neighboring elements. While the solution within each element carries a certain error relative to the true solution, iterative refinements are performed to minimize the total error across the entire domain [118].

## 5.3. Fiber tailoring and modal results

The simulated fiber features a large, rectangular-shaped core and belongs to the microstructured fiber category. The fiber was modeled using COMSOL's drawing tools, with the step-by-step process detailed in the Appendix. The overall fiber diameter is

125 µm, and all holes have a uniform diameter of 8 µm. The pitch, Λ, was tailored to ensure a 1 µm spacing between hole borders, resulting in Λ = 9 µm. The physical area of the core, calculated by multiplying its height and width, is 246.52 µm². The simulation was performed at a wavelength of 1.55 µm. The corresponding Figure 5.2 illustrates both a) the schematic of the fiber and b) the mesh result.


Figure 5.2: a) Drawing of simulated microstructured fiber and b) the mesh result.

Following the simulation, several modes were identified. For simplicity and to focus on the most meaningful results, only modes with purely real effective refractive index were considered. Under this criterion, seven modes were selected and are presented in Table 5.1. The table reveals that multiple modes share the same effective RI, indicating modal degeneracy or symmetry in the fiber structure.

Table 5.1: Table with the several obtained modes and their effective RI.

| | | | | |
|---|---|---|---|---|
| **Fundamental mode** | **1.4383** | | | |
| | 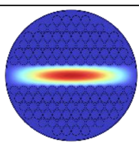 | 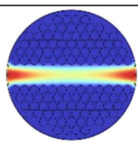 | 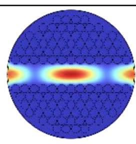 | 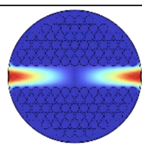 |
| **First mode** | **1.4382** | | | |
| | 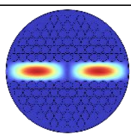 | 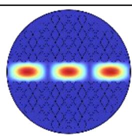 | 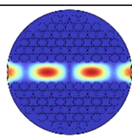 | |
| **Second mode** | **1.4380** | | | |
| | 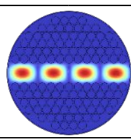 | | | |

## 5.4. Fiber shape tunning

To identify the optimal parameters for using this fiber as a sensor, a series of simulations were conducted by varying the core width and the d/Λ ratio across multiple wavelengths ranging from 1 µm to 1.95 µm, in increments of 0.5 µm. The core width was tested at three values: 15 µm, 20 µm, and 25 µm. The d/Λ ratios considered were 0.8888, 0.8, 0.7, and 0.6. Although several modes were obtained, a confined low-order mode was consistently present in all simulations, as shown in Figure 5.3. This mode was used as a reference for comparing different fiber configurations.

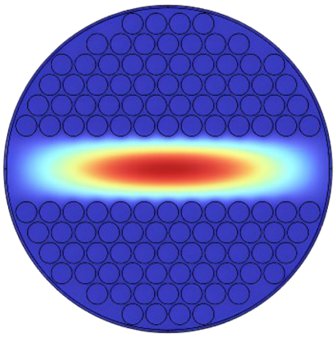

Figure 5.3: Studied confined mode presented for core = 25 $\mu m$ and d/Λ =0.8888.

The first analysis focused on how the effective refractive index varied with wavelength, as shown in Figure 5.4. As expected, the graph demonstrates that the effective RI decreases with increasing wavelength.

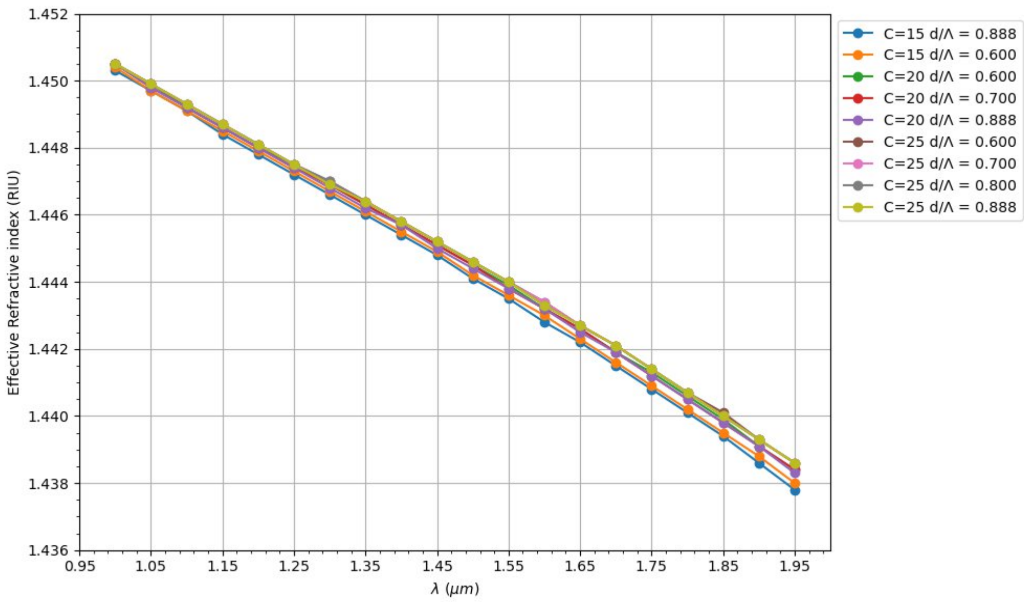


Figure 5.4: Effective RI changes as a function of wavelength for the simulated mode presented in Figure 5.3.

Using Equation (5.8) directly in COMSOL, the effective modal area for this mode was calculated across several fiber configurations, as shown in the plot Figure 5.5. For all analyzed configurations, the modal area increases linearly with wavelength. From a sensing perspective, a larger modal area is advantageous, as it indicates greater interaction between the guided mode and the analyte.

The figure presents three distinct data sets corresponding to different core widths. As expected, the larger the core, the greater the modal area, reinforcing the importance of core geometry in optimizing sensor performance.

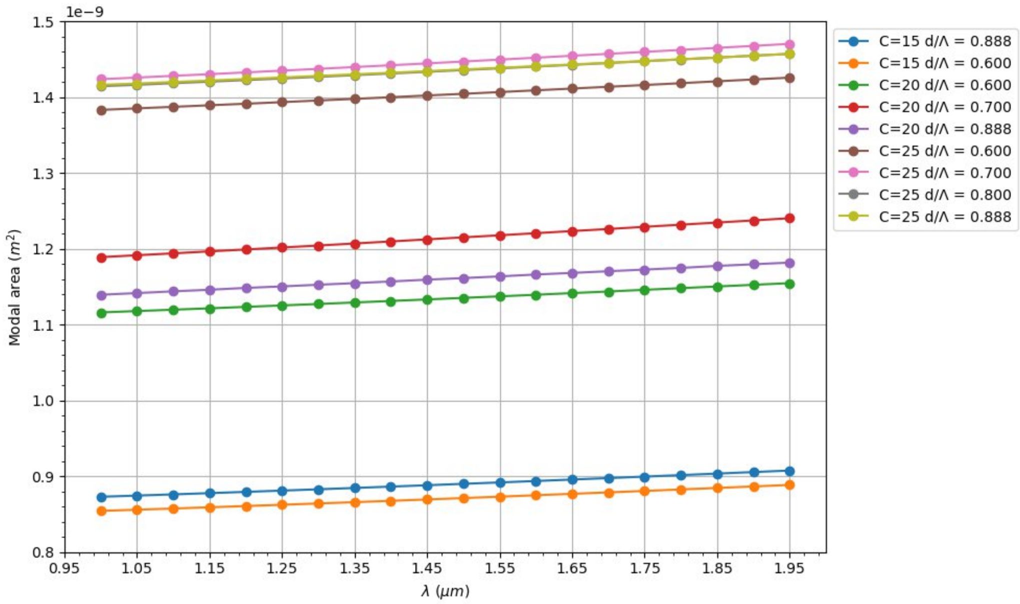


Figure 5.5: Effective modal area as a function of wavelength for the mode presented in Figure 5.3.

Another parameter analyzed was the confinement loss, calculated using Equation (5.9). This metric quantifies how much light is “lost” during propagation through the fiber. For the selected mode, confinement loss was computed across various configurations, with the results presented in Figure 5.6.

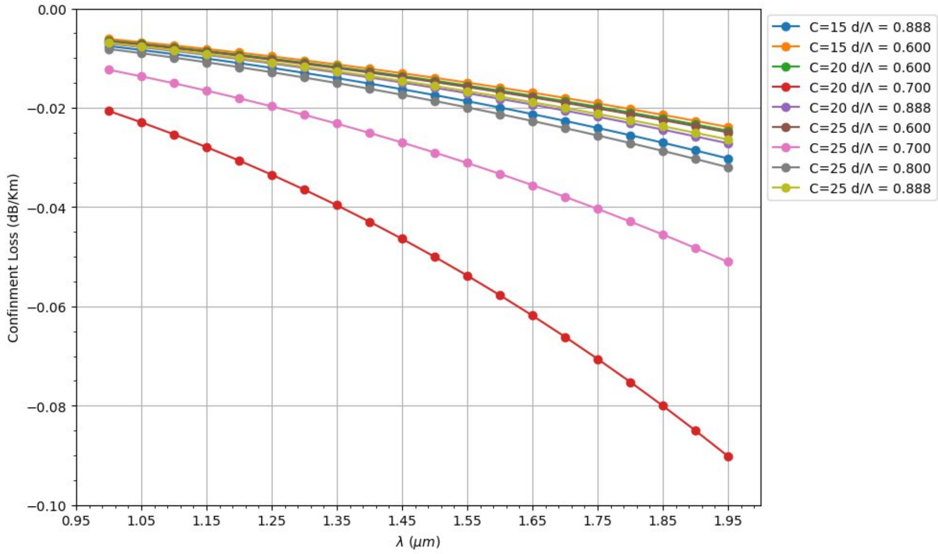


Figure 5.6: Confinement loss as a function of wavelength for the mode studied and for different fiber configurations.

Interestingly, higher propagation loss may indicate increased interaction between the guided light and the surrounding analyte, potentially leading to more accurate sensing results. This reinforces the idea that, in certain sensing applications, controlled loss can be beneficial when it enhances sensitivity.

By analyzing the results from Figure 5.7, the configuration with core width c = 25 μm and d/Λ = 0.7 (Figure 5.7c) appears to be the most suitable for using this fiber as a refractometric sensor. This setup offers a favorable balance between modal area and confinement loss, maximizing interaction with the analyte while maintaining stable mode propagation.

An additional set of analyses was performed. Although the reference mode was not present in all fiber configurations, the most similar mode in each case was selected for comparison. The general behavior of these analogous modes is presented in Figure 5.6.

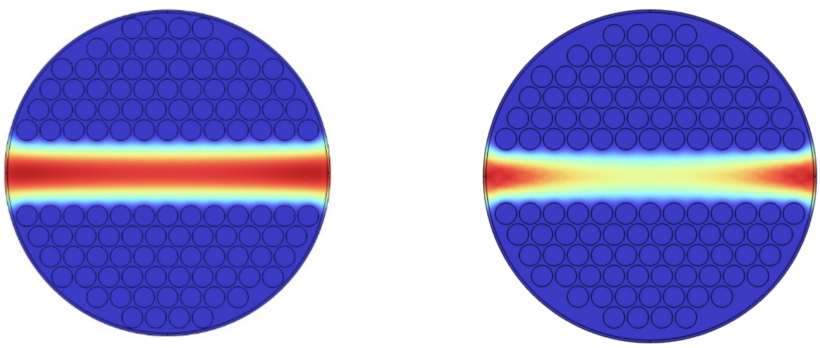

(a) (b)

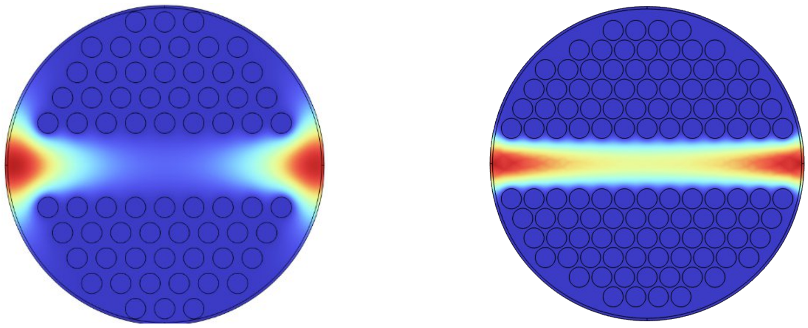

(c) (d)

Figure 5.7: Second studied mode for core = 25 $\mu m$ and a) d/Λ = 0.8888, b) d/Λ = 0.8000, c) d/Λ = 0.7000, and d) d/Λ = 0.6000.

The effective modal area as a function of wavelength, shown in Figure 5.8, does not exhibit three distinct groups as seen in the previous example. This is because the modes analyzed here are different across configurations. Nonetheless, the configuration with core width = 25 µm and d/Λ = 0.7 continues to present the largest modal area.

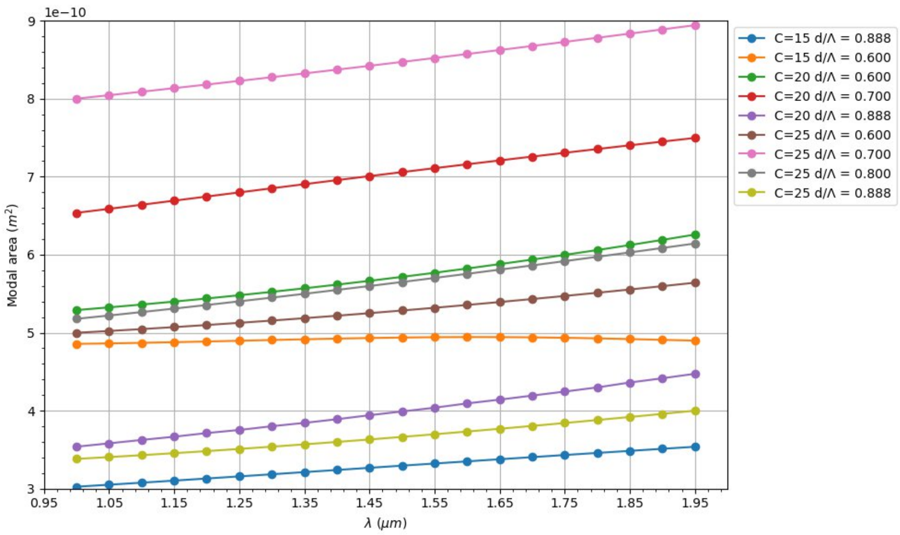


Figure 5.8: Effective modal area as function of wavelength for the modes studied and for different fiber configurations.

The confinement loss was also calculated, as shown in Figure 5.9. The selected configuration, core width of 25 µm and d/Λ = 0.7, demonstrates stronger confinement compared to most other setups. However, it ranks as the fourth least confined overall.

This suggests that while the mode remains well-guided within the fiber, there are configurations with even lower loss. Nonetheless, the balance between modal area and confinement makes this configuration a strong candidate for sensing applications.

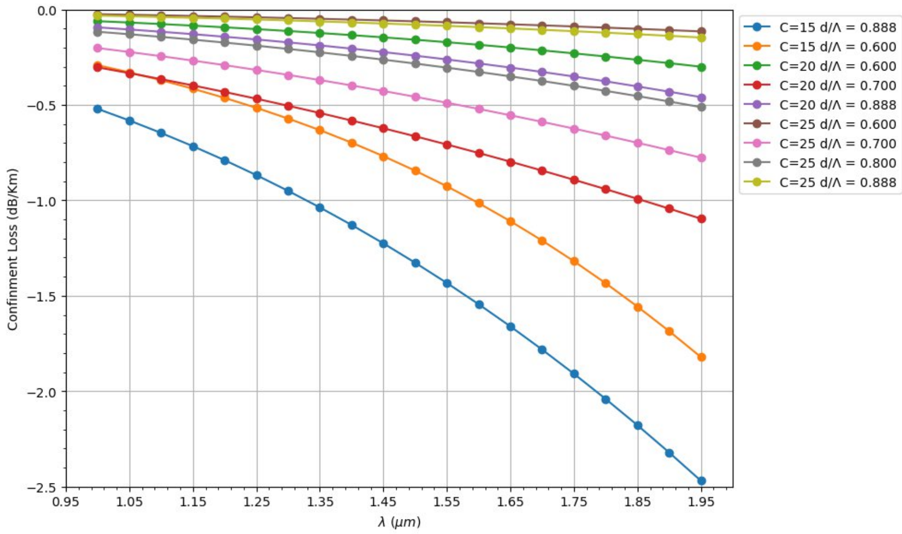


Figure 5.9: Effective modal area as function of wavelength for the modes for several fiber configurations.

## 5.5. Concluding remarks

In this chapter, modal simulations of a solid-core, large-modal-area microstructured fiber were conducted. The initial simulations used a 20 μm core with a d/Λ ratio of 0.8888. Several modes were identified, and a subset of lower-order modes was presented. The next phase focused on optimizing fiber design. Three core widths: 15 μm, 20 μm, and 25 μm, were tested across four d/Λ ratios: 0.6, 0.7, 0.8, and 0.8888. A particular mode was consistently observed across all simulations. For this mode, both the effective modal area and the confinement loss were calculated. The results showed that increasing the core width leads to a larger modal area, making the 25 μm core the most favorable. Additionally, a d/Λ ratio of 0.7 emerged as the optimal configuration. To validate this choice, another mode or its closest equivalent was analyzed, characterized by strong electric field intensity near the fiber boundary. The results confirmed that this alternative mode exhibited similar behavior, reinforcing the selection of the 25 μm core and d/Λ = 0.7 as the most effective configuration.

# 6. Fano-like FBG

## 6.1. Introduction

FBGs were first introduced in 1974 by Kenneth Hill and his team [119]. Since their inception, FBGs have found applications across multiple domains, including structural health monitoring in civil engineering [120], aerospace systems operating in harsh environments [121], and environmental sensing [122].

Throughout their evolution, various advancements have been made to enhance the sensing capabilities of FBGs. These include improvements in grating inscription techniques and the development of novel packaging strategies to shield the sensors from external influences [123–125].

In this chapter, a new FBG architecture is investigated. The grating is physically sliced, resulting in a reduced pitch. This structural modification induces a Fano-like reflection spectrum. The sensor head was first evaluated for its temperature sensitivity. Subsequently, with temperature held constant, the sensor's response to changes in external RI. Finally, the same methodology described in Chapter 4 was applied to characterize the sensor head for evaporation dynamics, enabling the study of droplet behavior during evaporation.

## 6.2. FBG concepts

In its simplest form, an FBG is an optical fiber with a periodic modulation of the RI along a specific section. Each variation in RI acts as a weak mirror, reflecting a portion of the incident light. This back reflected light has a wavelength centered around the average period of the grating, while other wavelengths pass through unaffected [126]. This physical description leads to the formulation of the fundamental equation for FBG, as presented in [126]:

$$\lambda_B = 2 n_e \Lambda \tag{6.1}$$

where $\lambda_B$ is the Bragg wavelength, $n_e$ is the effective refractive index and $\Lambda$ is the period of the grating [126].

When the FBG is subjected to variations in strain and temperature, it induces changes in both the effective RI of the fiber core and the grating period. These changes result in a shift in the reflected wavelength [127]. To quantify the peak wavelength shift caused by these two parameters, one can differentiate Equation (6.1) with respect to strain and temperature, yielding the following expression as presented in [128]:

$$\lambda_B = 2n_e\Lambda \quad (6.2)$$

$$\Delta\lambda_B = 2\left(\Lambda\frac{\partial n_e}{\partial l} + n_e\frac{\partial \Lambda}{\partial l}\right)\Delta l + 2\left(\Lambda\frac{\partial n_e}{\partial T} + n_e\frac{\partial \Lambda}{\partial l}\right)\Delta T = \quad (6.3)$$

$$= 2\, n_e\Lambda([1 - (\frac{n_e^2}{2})(P_{12} - \nu(P_{11} + P_{12}))]\varepsilon + [\alpha_f + \frac{\frac{dn_e}{dT}}{n_e}]\,\Delta T)$$

$$\lambda_B = (K_T\Delta T + K_\epsilon\epsilon) \quad (6.4)$$

$P_{11}$ and $P_{12}$ are the photo-elastic coefficients, $v$ is the optical fiber Poisson ratio, $K_\varepsilon$ is the strain sensitivity, which is given by: $K_\varepsilon = \frac{\frac{\Delta\lambda_B}{\lambda_B}}{\Delta\varepsilon} = 1 - P_e$, $P_e$ is the effective photo-elastic coefficient given by: $P_e = \left(\frac{n_e^2}{2}\right)(P_{12} - \nu\,(P_{11} + P_{12}))$; $K_T$ is the temperature sensitivity of the grating, given by: $K_T = \frac{\frac{\Delta\lambda_B}{\lambda_B}}{\Delta T} = \alpha_f + \xi$, where $\alpha_f$ is the thermal expansion coefficient and $\zeta$ is thermos-optical coefficient [128].

Considering constant temperature, only strain, the change of the peak is given by [127]:

$$\frac{\Delta\lambda_B}{\lambda_B} = (1 - P_e)\,\varepsilon = K_\varepsilon\cdot\varepsilon \quad (6.5)$$

As shown in Equation (6.5), it is possible to maintain a constant temperature and analyze strain effects. However, it is not feasible to isolate temperature measurements while stabilizing strain, which leads to cross sensitivity. A common approach to mitigate this issue involves using two FBG sensors exposed to the same temperature and strain conditions. These sensors must be configured such that they possess different temperatures and strain sensitivity coefficients. This setup results in a system of two equations, like those in Equation (6.4), with two unknowns, allowing for the simultaneous determination of strain and temperature effects [126].

## 6.3. Sliced FBG

Sliced Fiber Bragg Grating (SFBG) is a newel architecture of FBG where a regular grating is sliced, resulting that the last grating pitch is lower than others [129]. Resonance can be broadly defined as the phenomenon where an external frequency, applied to an oscillator, closely matches the system's natural frequency, resulting in a large amplitude of oscillation with minimal applied force [130].

A notable example of resonance in optics is the Fano resonance. Initial results emerged in 1935 for a limiting case [131], but the full theoretical description was introduced by Ugo Fano in 1961 [132].

This resonance is modeled using two weakly coupled oscillators. To visualize it, consider two pendulums: one is driven by an external force and exhibits high damping, while the other has low damping and oscillates near its natural frequency. The pendulums are connected by springs. The externally imposed frequency on the first pendulum interacts with the natural frequency of the second, producing a range of behaviors: resonance, antiresonance, or intermediate states [133].

In optical terms, Fano-like resonance is described as the interference between a continuous signal and a discrete resonance. In the pendulum analogy, the discrete signal corresponds to the driven pendulum, while the continuous signal represents the second pendulum [133]. This interference manifests in the absorption spectrum and can also be observed in transmission and scattering spectrum. The characteristic asymmetric line shape of this resonance is described by the Fano formula [134]:

$$\sigma(E) = N^2 \frac{(q+\Omega)^2}{1+\Omega^2} \tag{6.6}$$

*E* is the energy, *N* represents 2sin($\delta$)), being $\delta$ the phase shift in the continuum, *q* is the Fano parameter equal to cot($\delta$) and Ω is the dimensionless frequency used for fine tuning and is presented as $2\frac{E-E_0}{\Gamma}$ where Γ is the resonance width and $E_0$ the resonance energy, it also may be presented as $\frac{\omega-\omega_0}{\gamma}$, $\omega$ is the frequency of the discrete spectrum and $\omega_0$ of the resonance and $\gamma$ the damping [133-135].

Figure 6.1a) illustrates the dependence of the Fano parameter *q* on the phase shift of the continuum spectrum. In the same graph, colored crosses mark specific points that correspond to distinct resonance behaviors. These points are further explored in Figure 6.1b), which presents the normalized transmission spectra for the same *q* values, using matching colors.

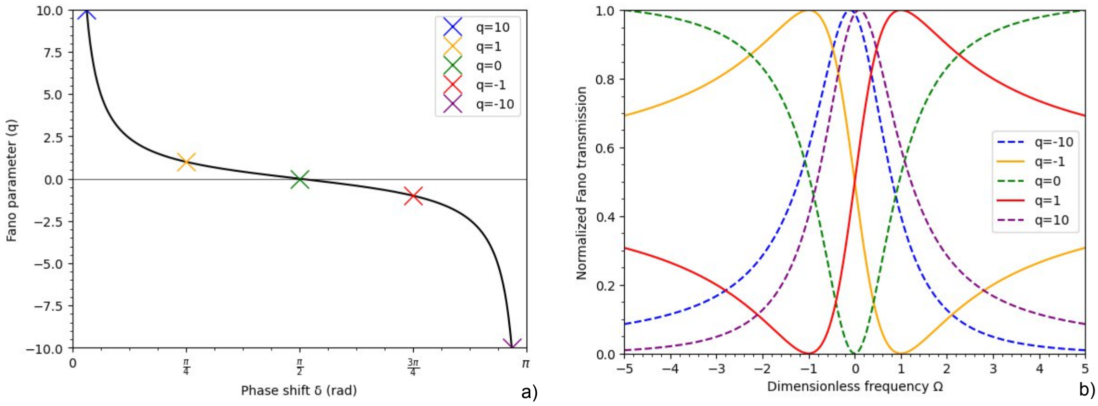


Figure 6.1: a) Dependence of the Fano parameter *q* on the phase shift of the continuum spectrum. In the same graph, colored crosses mark specific points values for *q*, namely, −10, −1, 0, 1, 10, that correspond to distinct resonance behaviors. b) Normalized transmission spectra for the same *q* values and with matching colors. Adapted from [133,135].

At $q$ = 10 and $q$ = –10, the transmission spectra exhibit a Lorentzian shape, indicating the absence of Fano windows, i.e., no coupling between the discrete and continuum states. At $q$ = 1, a classic Fano profile emerges, where the natural frequency equals –$q$. The spectrum first shows a transmission peak followed by a dip, signifying a point of maximum reflectance. For $q$ = 0, the behavior resembles a quasi-Lorentzian shape, corresponding to a natural frequency at zero but with no effective coupling to the discrete state. Finally, at $q$ = –1, the behavior mirrors the case of $q$ = 1, but with the roles reversed: the spectrum begins with a reflectance minimum followed by a maximum, corresponding to a natural frequency at $\omega_0$ = q [133,135].

### 6.3.1. Experimental apparatus and methodology

The experiment includes three different stages: the first is the effects of temperature on the wavelength, the second effects of the RI on reflected power and last is the evaporation dynamics study. The schematic of the experimental setup is shown in Figure 6.2.

To conduct this experiment, a broadband source was used and connected to the input port of an optical circulator (Thorlabs, 6015-3). The second port of the circulator was connected to the SFBG to be read in reflection, while the third port was linked to an optical spectrum analyzer (OSA, Yokogawa AQ6370C).

For the temperature analysis, a Peltier cooler (PLT) with variable voltage control was placed near the fiber tip to induce thermal changes. Temperature was monitored using a K-type digital thermometer.

For the remaining parts of the experiment, the same mechanical setup described in Chapters 3 and 4 was employed to move the sensor head vertically. Several sucrose solutions were used for RI analysis, and a mixture of water and IPA was applied for the evaporation study.

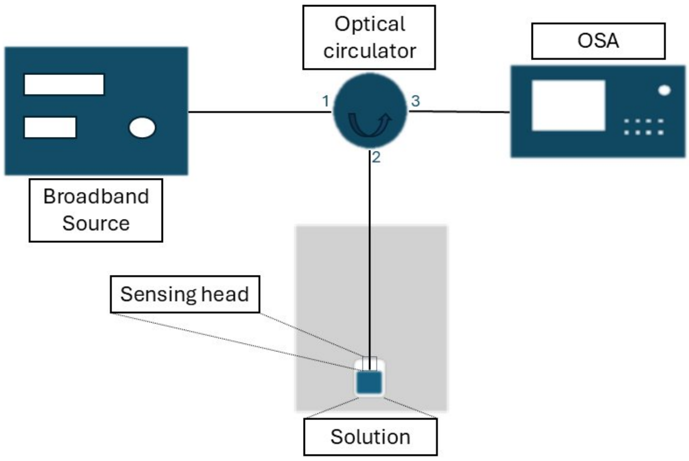


Figure 6.2: Experimental setup used for the Fano-like FBG experiment.

In the first part of the experiment, the OSA was configured with a resolution of 0.5 nm, and a total of 5001 data points. The voltage applied to the PLT was incremented by 0.5 °C after each measurement, resulting in the following temperature values: 26.0, 26.6, 27.1, 27.5, 28.0, 28.5, 29.0, 29.5, and 30.0 °C.

In the second part, the OSA settings remained unchanged. A series of sucrose solutions with varying refractive indices were used. Prior to each measurement, the RI of the solution was verified using an Abbe refractometer (ATAGO DR-A1) to minimize the influence of external temperature fluctuations.

For the evaporation analysis, the OSA was set to a fixed span centered at 1550 nm, positioned at the midpoint of the slope between the minimum and maximum of the Fano-like spectrum. The resolution was adjusted to the minimum available scale, and averaging was set to 2. In practice, the sweep duration was first measured using a chronometer. The fiber was then immersed in the solution and subsequently raised to just above the liquid surface to capture the evaporation power change.

After carefully cutting the fiber as close as possible to the center of the FBG region, it was successfully spliced to an SMF and integrated with the rest of the experimental setup. This process resulted in the final sensor head configuration, as shown in Figure 6.3.

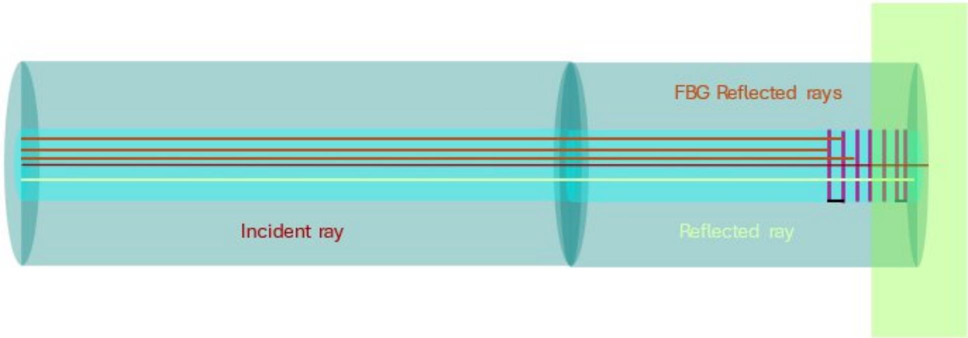


Figure 6.3: Schematic of the SFBG sensor.

Fano resonance in this sensor configuration arises from the interference between a continuum signal, originating from Fresnel reflections at the fiber tip, and a discrete signal, generated by reflections from the FBG region. A more practical interpretation considers the spectral peak as resulting from the grating response, while the trough is attributed to the Fresnel reflection at the fiber tip.

The resulting spectrum for this sensor head is shown in Figure 6.4. It clearly displays a trough followed by a peak, characteristic of a Fano resonance with $q \approx 1$. This asymmetric line shape confirms the presence of interference between the discrete and continuum components, validating the sensor's design and its potential for refractometric applications.

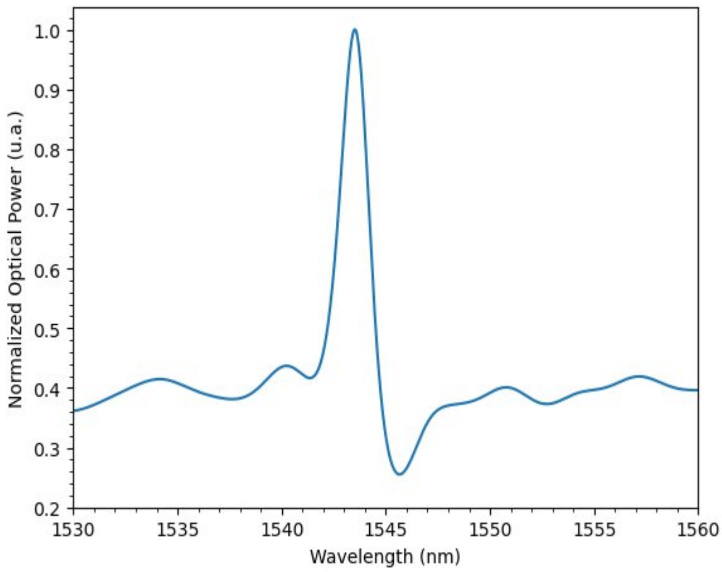


Figure 6.4: Fano-like normalized spectrum obtained after slicing the FBG.

### 6.3.2. Sensitivity to temperature

Like traditional FBG sensors, the SFBG configuration also exhibits sensitivity to ambient temperature, making it a strong candidate for temperature variation sensing. As shown in Figure 6.5a), the peak wavelength, corresponding to the FBG region of the spectrum, shifts consistently with changes in temperature. The measured sensitivity for this sensor is 16.9±0.5 pm/ºC, with a determination coefficient of $R^2$=0.9936, indicating excellent linearity and reliability in temperature response.

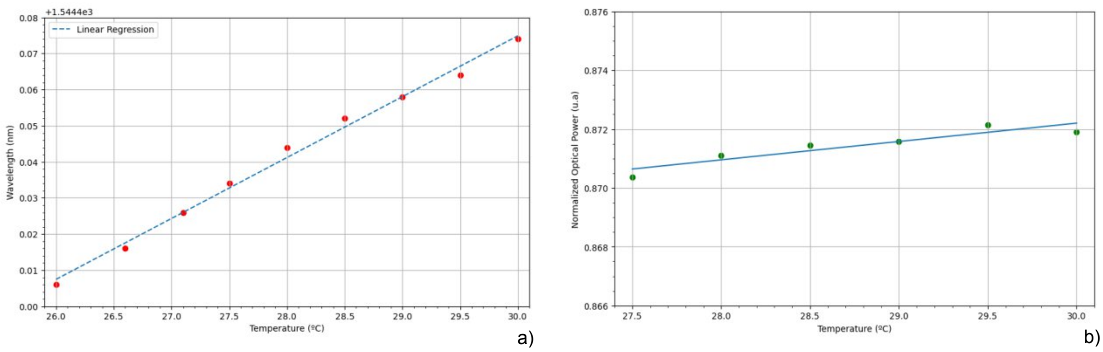


Figure 6.5: a) Bragg wavelength and b) optical power changes with temperature variation.

Furthering the analysis, variations in the normalized intensity of the trough were also observed as temperature changed. For each spectrum, the difference between the peak and trough intensities was evaluated, and the resulting values are plotted in Figure 6.5b) as a function of temperature. The graph displays a moderately increasing trend, and the calculated sensitivity was 0.6±0.1 ºC$^{-1}$, with a coefficient of determination $R^2$=0.8495.

The relatively low $R^2$ value is attributed to the higher susceptibility of this measurement to noise and external fluctuations. With a larger dataset and improved control over experimental conditions, a more robust regression is expected.

### 6.3.3. Sensitivity to RI of the external medium

Due to its fiber tip configuration, the SFBG can be employed as a refractometer OFS. To evaluate this capability, the fiber tip was placed in contact with various mixtures of water and sucrose. As in the previous part of the experiment, the shift in the Bragg peak was monitored for each spectrum. The resulting values, plotted as a function of RI, are presented in Figure 6.6.

It is evident that, like a conventional Bragg grating, the peak wavelength is not sensitive to changes in RI of the external medium. The sample variance $s^2$ calculated for these data points is 0.00108, confirming the residual sensitivity of the Bragg peak to RI variations.

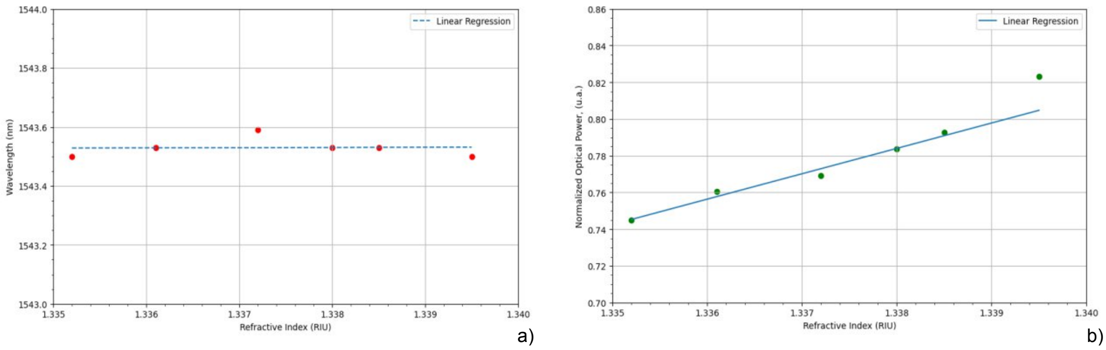


Figure 6.6: a) Bragg wavelength and b) optical power changes with the RI variation of the external medium.

As the wavelength remains insensitive to variations in the external RI, the trough, originating from Fresnel reflections, is not. Based on this, the difference in normalized optical power between the peak and the valley was measured for each spectrum. The corresponding values for each RI are presented in Figure 6.6b).

The graph reveals a clear increasing trend in the optical power difference with rising RI. A linear regression was performed, excluding the final data point, and the resulting sensitivity was 14 ± 1 $RIU^{-1}$ with a coefficient of determination $R^2$ = 0.9829. This strong correlation highlights the potential of the trough intensity as a reliable refractometric sensing parameter.

### 6.3.4. Evaporation dynamics evaluation

Continuing with the thematic focus of this dissertation, additional studies were conducted to evaluate the behavior of this sensor as an evaporation sensor. In this configuration, a liquid droplet is placed in contact with the sliced grating. This interaction changes the nature of the continuum signal.

After dipping the SFBG fiber tip in a liquid and upping the fiber, the evaporation power changes in time, as presented in Figure 6.7, it was possible to obtain a temporal response like the one achieved with the SMF-tip sensor. This graph is divided into four parts: the first region, in orange, is when the fiber tip is submerged in the liquid optical and the optical power significantly lowers due to the RI increase of the surrounding medium; the pink region is for the visible FFPI cavity formation as the liquid droplet is present at the fiber tip; purple for the residual water that remains at the fiber tip and the FP cavity starts to disappear. Finally, the second orange part where fiber tip loses the liquid droplet and it gets in full contact with air.

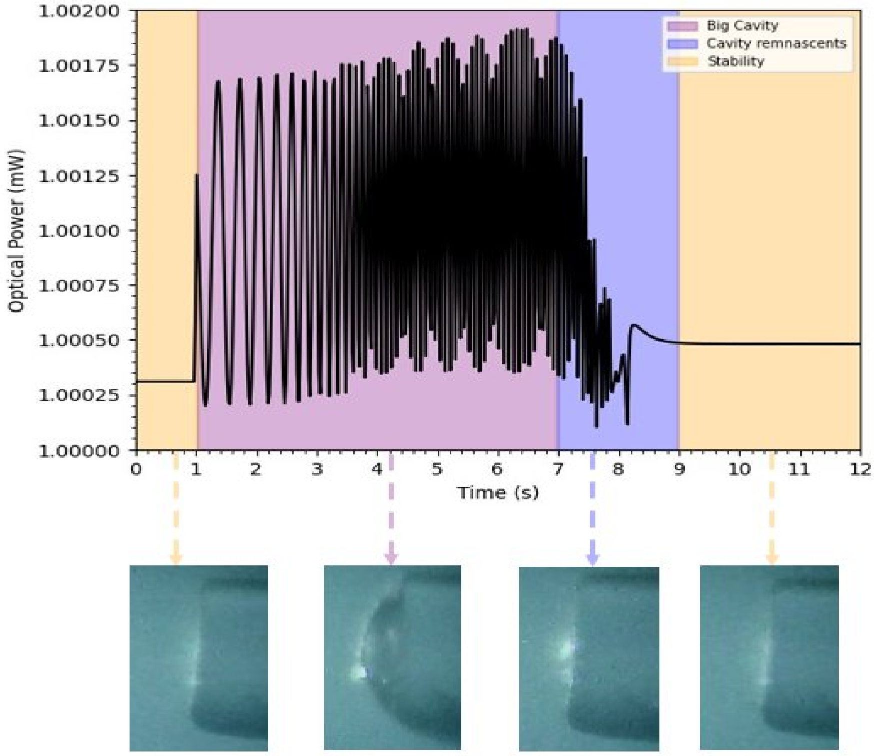


Figure 6.7: Reflected power variation of the SFBG fiber-tip sensor in the liquid solution, divided into four zones: orange is when the fiber tip is submerged in the liquid optical and the optical power significantly lowers due to the RI increase of the surrounding medium; the pink region is for the visible FP cavity formation as the liquid droplet is present at the fiber tip; purple for the residual water that remains at the fiber tip and the FP cavity starts to disappear. Finally, the second orange part where the fiber tip loses the liquid droplet and it gets in full contact with air.

A FFT was performed from the first major peak in the large cavity region to the end of that zone, with results presented in Figure 6.8. Two types of points are highlighted: signal points, located between the two green vertical lines, with the most prominent ones marked by the lines, and noise peaks, indicated by red crosses.

To evaluate the sensor’s quality, the difference in dB between each signal point and all identified noise peaks was calculated. For each signal point, the median of these differences was determined, and then the mean value of the two resulting medians was computed. The final value obtained was 20.1101, indicating a strong signal-to-noise contrast in the evaporation response.

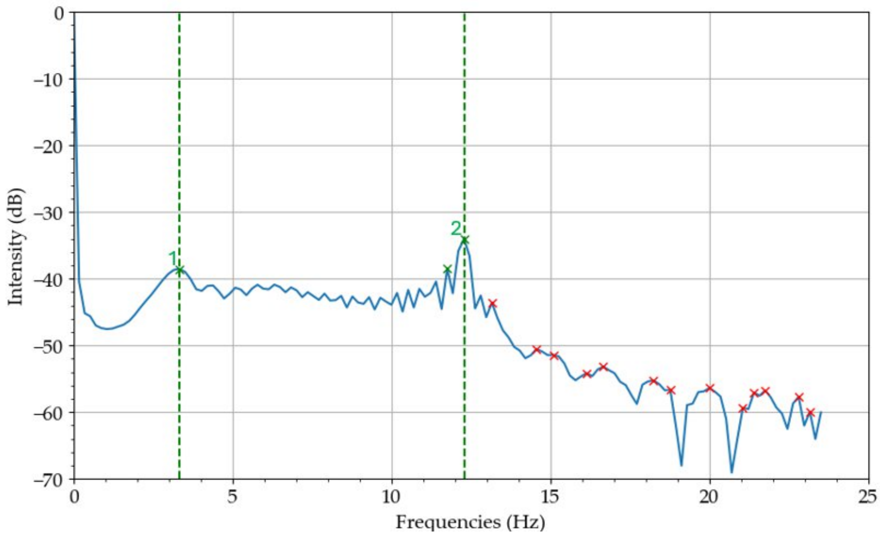


Figure 6.8: FFT obtained from the reflected spectrum of the SFBG-tip sensor. Noise peaks are marked with red crosses and major signal peaks are with green crosses and vertical green lines.

Figure 6.8 may indicate that the mixture is, in fact, composed of water and IPA, given its similarities with the graphs presented in Chapter 4. By analyzing the frequencies associated with the two peaks marked by the green lines and applying Equation (4.3), it is possible to estimate the evaporation rates: the first peak corresponds to $-1.9337 \times 10^{-6}$ m/s, and the second to $-7.1241 \times 10^{-6}$ m/s.

Furthering the analysis, the Hilbert formula was used to calculate the instantaneous evaporation rate, as shown in Figure 6.9. Observing the plot, these two methods appear to validate each other, since the second and more intense peak aligns closely with the region where the instantaneous evaporation rate persists longer.

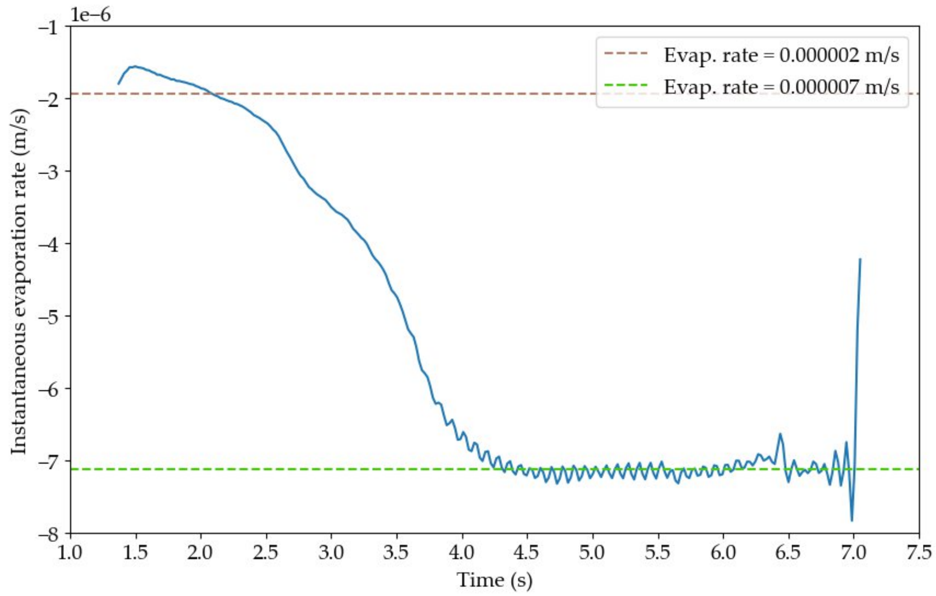


Figure 6.9: Obtained plot of the instantaneous in $m$/s with the two calculated evaporation rates from the FFT.

Lastly, to estimate the initial thickness of the droplet, the mean value of all instantaneous evaporation rates was calculated and multiplied by the total evaporation time. This time interval was defined from the beginning of the purple region to the final peak of the blue region in Figure 6.7, resulting in a duration of 7.24 seconds. Based on this, the calculated thickness is $-3.8336 \times 10^{-5}$ m.

## 6.4. Concluding remarks

To summarize, this chapter explored a novel type of FBG, created by slicing the grating and forming a non-uniform final grating pitch. Analysis of the reflection spectrum revealed a Fano-like profile with $q$ = 1.

The first part of the study examined the sensor's response to external temperature variations. The Bragg peak wavelength shift was measured, yielding a sensitivity of 16.9 ± 0.5 pm/ºC. Additionally, the intensity difference between the peak and valley was analyzed, resulting in a sensitivity of 0.0006 ± 0.0001 $ºC^{-1}$. These results confirm the sensor's viability for temperature monitoring.

The second part focused on the sensor's performance as a refractometric device. With temperature stabilized, the Bragg peak remained constant across different RI values, with a sample variance of 0.00108. However, the intensity difference between the peak and trough exhibited a clear increasing trend with RI, leading to a sensitivity of $14 \pm 1\ \mathrm{RIU}^{-1}$.

The final section assessed the sensor's capability to monitor evaporation dynamics. The optical power remained stable and resembled that of a SMF. A FFT analysis revealed characteristics typical of IPA or a water-based mixture, with an "error value" of 20.1 dB. Evaporation rates associated with the two major peaks were calculated as $-1.9337 \times 10^{-6}$ m/s and $-7.1241 \times 10^{-6}$ m/s. Using the Hilbert transform, the instantaneous evaporation rate was plotted, and an approximate initial droplet thickness of $-3.8336 \times 10^{-5} m$ was determined.

To conclude, this chapter introduced the SFBG and demonstrated its potential as both a temperature and RI sensor. In both cases, further testing across a broader range of values is necessary to define its operational limits and identify regions of optimal performance.

# 7. Final conclusions and future work

In its early stages, this work focused primarily on the characterization of refractive index fiber-tip sensors. As the research progressed, new challenges emerged, most notably the evaluation of a novel sensing head, the SFBG, which provided an alternative framework for comparison with the previously investigated configurations.

Even though its validation was limited to the low RI regime, normalized values were reported in Table 7.1 to enable a methodologically consistent comparison, accounting for the distinct analytical approach inherent to this configuration.

It may therefore be inferred that, although the SFBG does not attain the highest sensitivity among the sensor heads examined, it nonetheless exhibited superior performance when compared with the reference configuration previously analyzed. Within the range investigated, the Step-Index MMF continues to constitute the most sensitive device. However, the SFBG should not be disregarded, as its intrinsically more straightforward data interpretation significantly enhances its suitability for automated processing, thereby reinforcing its potential as a viable candidate for real-world applications.

| Sensors | Low RI range ($RIU^{-1}$) |
|---|---|
| **STEP-INDEX** | 12.00 ± 0.5 |
| **GRADED-INDEX** | 21.00 ± 4.0 |
| **Microstructured** | 23.00 ± 7.0 |
| **FBG** | 9.50 ± 0.2 |
| **SFBG** | 14.00 ± 1.0 |

Table 7.1: Values for sensitivity, low range RI, for all analyzed sensor heads.

Furthermore, the investigation of evaporation dynamics was motivated by the broader need for material characterization, as well as by the pursuit of a preliminary framework to evaluate measurement repeatability. Initial experiments were carried out using SMF, after which other fiber types were tested with the aim of identifying the configuration that offered the most robust performance. Although the SFBG was later subjected to an equivalent experimental procedure, the direct comparison of results was precluded by variations in the liquid mixture employed, thereby introducing an inherent limitation to the analysis.

Nevertheless, this constraint also underscores the importance of standardizing experimental conditions for future studies, as such consistency is essential for ensuring the validity of comparative assessments. In addition, the subsequent opportunity to simulate a novel microstructured fiber geometry provided a pathway for further exploration, highlighting the potential for structural optimization in advancing sensor performance and paving the way for the development of next-generation optical fiber sensing platforms. With respect to future work, several research directions can be envisaged, namely:

- Fabrication of the newly designed microstructured fiber in collaboration with Jena, Germany.
- Characterization of this fiber with respect to a range of physical parameters.
- Extended investigation of the SFBG over broader temperature ranges, to achieve a comprehensive characterization.
- Further analysis of the SFBG in terms of RI response and exploration of potential applications of the SFBG as a sensing element.
- Application of thin films to further enhance sensing capabilities.

# Appendix A: Study of FBG fringes

Recall Section 3, Figure 3.21, presents the analyzed spectra of the FBG to the measurements of distinct RI mixtures. It's possible to see interference patterns at the left and right parts of the Bragg's peak. To analyze the left side of the spectrum, the windows between 1545 and 1549 nm were chosen and the peaks for each spectrum were determined, Figure A.1a) presents the interference spectrum of the FBG left side, and Figure A.1b) shows the peaks coordinates for all RI mixtures.

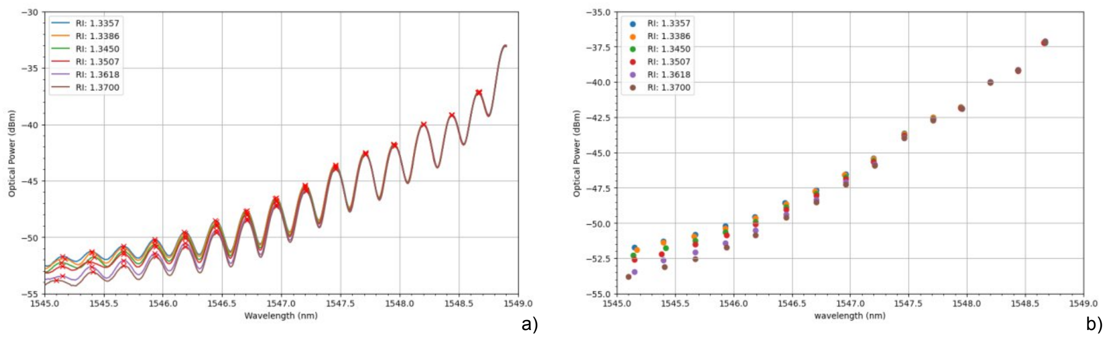


Figure A.1: a) Left side of the spectra with red crosses indicating the peaks positions; b) plot of the peak coordinates for all mixtures.

Points presented in Figure A.1a) have 15 different groups by wavelength, for each of these groups, the sample variance ($s^2$) and the sample standard deviation ($s$) were calculated. Table presents these values, but it was calculated the mean wavelength for each group to better associate the graph line with Figures A.1a) and A.1b).

Table A.1: Left-side peaks sample variance and standard deviation.

| ***Wavelength (nm)*** | $s^2$ | $s$ |
|---|---|---|
| *1545.14* | 0.7082 | 0.8416 |
| *1545.40* | 0.5133 | 0.7164 |
| *1545.67* | 0.4556 | 0.6750 |
| *1545.93* | 0.3506 | 0.5921 |
| *1546.19* | 0.2525 | 0.5025 |
| *1546.45* | 0.1766 | 0.4202 |
| *1546.71* | 0.1216 | 0.3487 |
| *1546.96* | 0.0857 | 0.2928 |
| *1547.20* | 0.0475 | 0.2179 |
| *1547.46* | 0.0187 | 0.1367 |
| *1547.71* | 0.0066 | 0.0812 |

| | | |
|---|---|---|
| *1547.95* | 0.0040 | 0.0631 |
| *1548.20* | 0.0004 | 0.0211 |
| *1548.44* | 0.0005 | 0.0232 |
| *1548.67* | 0.0019 | 0.0438 |

Looking at the values, it’s possible to see that as the wavelength gets bigger the lower gets the $s^2$ and $s$ apart from the last point.

Now to verify the right part of the spectra the same procedure as the previous case was carried out. First, the spectral window was set between 1550 nm and 1555 nm and the peaks were verified Figure A.2a), in this image there are two peaks not identified between 1551 and 1551.4 because the function used to detect peaks, find_peaks from scipy.signal, was not accurate no detect then without detecting noise in other peaks.

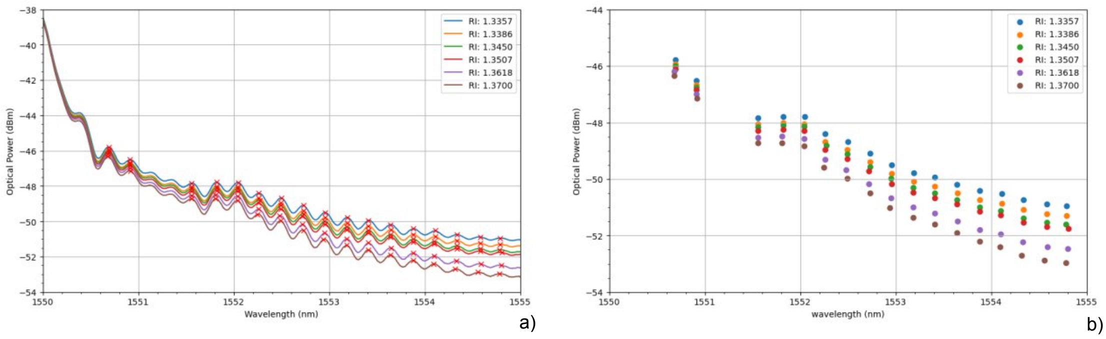


Figure A.2: a) Right side of the spectra with red crosses indicating the peaks positions b) Right side of the spectra plot of the peaks coordinates for all mixtures.

In Figure A.2b) represents the peaks identified. Visually peaks go wider in difference of optical power as the wavelength furthers away from the peak’s wavelength. To analyze this, for points in a certain peak the sample variance and standard deviation of reflected optical power were calculated, and the values are presented in Table A.2.

Table A.2: Right-side peaks sample variance and standard deviation

| ***Wavelength (nm)*** | $s^2$ | $s$ |
|---|---|---|
| *1550.69* | 0.0373 | 0.1931 |
| *1550.91* | 0.0514 | 0.2268 |
| *1551.56* | 0.1036 | 0.3219 |
| *1551.82* | 0.1129 | 0.3360 |
| *1552.04* | 0.1367 | 0.3697 |
| *1552.26* | 0.1870 | 0.4324 |
| *1552.49* | 0.2260 | 0.4754 |
| *1552.73* | 0.2649 | 0.5147 |
| *1552.95* | 0.3171 | 0.5632 |

| | | |
|---|---|---|
| *1553.18* | 0.3418 | 0.5846 |
| *1553.41* | 0.3827 | 0.6186 |
| *1553.64* | 0.4110 | 0.6411 |
| *1553.88* | 0.4511 | 0.6716 |
| *1554.10* | 0.4865 | 0.6975 |
| *1554.34* | 0.5316 | 0.7291 |
| *1554.58* | 0.5515 | 0.7426 |
| *1554.79* | 0.5618 | 0.7496 |

Table A.2 verifies that both $s^2$ and $s$ increase as the wavelength furthers away from the Bragg's peak. For further analysis, the left side of the spectra is more sensible to changes, since its biggest variance is higher than the biggest from the left-side, 0.7082 and 0.5618, indicating that optical power are more disperse indicating a better sensing capability.

# Appendix B: Second measurement

This appendix has the purpose of looking for how the microstructured fiber-tip sensor holds its values after doing measurements, and after doing one step of measurements of all the mixtures.

Values obtained from the measurements with the OPM (Figure B.1a)), in this graph the hysteresis acts a little different from the graded index, here there is an alternation between higher optical power between the first try (blue) and the second try (orange). It's possible to see that the exponential regression for the second set is higher in optical power values than the first try.

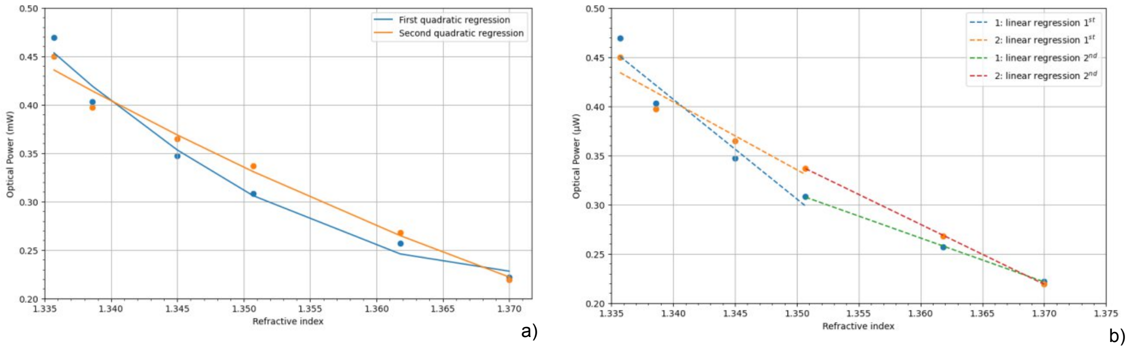


Figure B.1: a) Quadratic regression for both datasets; b) linear regressions for high and low ranges, and for both datasets.

| *SI Range* | Sensitivity (µW/RIU) | $R^2$ |
|---|---|---|
| *1.3357-1.3507 - First* | 10.00 ± 2.00 | 0.9425 |
| *1.3357-1.3507 - Second* | 7.00 ± 2.00 | 0.9996 |
| *1.3507-1.3700 - First* | 4.46 ± 0.09 | 0.9135 |
| *1.3507-1.3700 - Second* | 6.09 ± 0.09 | 0.9998 |

Table B.1: Representation of the obtained sensitivities for both sets of data, obtained with the OPM.

Comparing values between the first and the second try, it's possible to see that this sensor loses sensitivity at the second try for the lower range of RI and has bigger sensitivity for the higher RI range.

Analyzing spectra, Figure B.2, it's also possible to see hysteresis effects on this sensor. In the regions between 1550 and 1560 nm, it's possible to see that spectra, minus the two higher ones, are closer to each other on the second graph than on the first one, noticing loss of sensitivity in that selected region, the same effect is also noticeable in the peak between 1560 and 1565 nm.

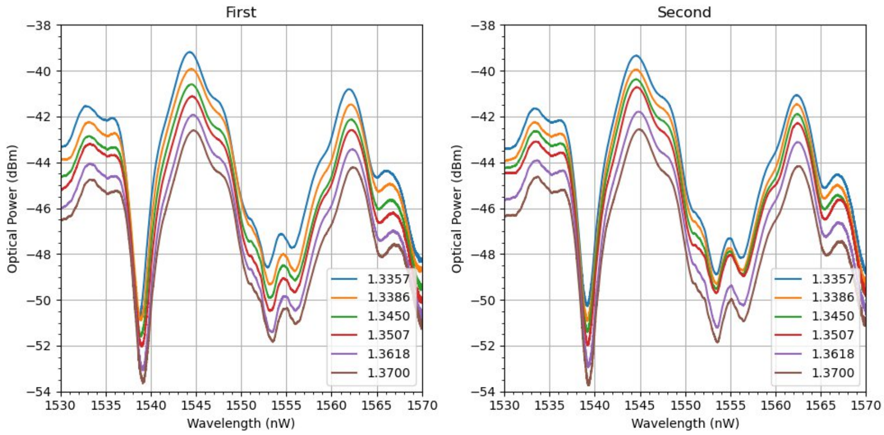


Figure B.2: Microstructured fiber-tip spectrum for both experiments.

This fiber has high tendency for hysteresis, because the analyte infiltrates in the holes and it gives more are for analyte remnants to stay in the fiber.

# Appendix C: Simulation routine

In this Appendix is provided the step by step of to do simulations using COMSOL Multiphysics.

**Modal analysis**

To open the app and select the study:

- Open the App.
- Choose Modal Wizard.
- In “Select Space Dimension” window choose the icon that says 2D.
- In the “Select Physics” window choose “Electromagnetic Waves, Frequency Domain (ewfd)” and click the button “Add” followed by the button “Study” at the bottom.
- In the “Select Study” window go to “Preset Studies for Selected Physics Interfaces” and choose “Mode Analysis” and click the button “Done” at the bottom.

After this, COMSOL interface is shown, and the next step is to build the first simulation geometry:

- In “Global Definitions” go to “Parameters 1”.
- Define the fiber’s diameter as 125[um], the hole diameter as 8[um], Λ as 9[um], the width from the center of the core to the center of the first row of holes as 14[um], set Perfectly Matched Layer (PML) as 1[um], the wavelength of the light as 1.55[um] and the silica refractive index as 1.4443.
- To construct the fiber is to right click in “Geometry 1” of “Component 1” and draw circles plus creating arrays and copies.
- Once the fiber is drawn, right click in “Component 1 - Materials” and select “Add Materials from Library”.
- A window appears at the right side of the screen and search for “Air” choose the one in the “Built-in” option.
- Select the domains that are associated with the holes.
- Choose another material, but write “Silica Glass” and choose, again, the one from “Built-in”.
- Once chosen, select the domains associated with silica and change the real refractive index from 1.45 to 1.4443.

- In “Parameter 1 - Definitions” right click and choose “Perfectly Matched Layers” choose the domains associated with PML zones.
- Once in this window go to “Geometry” and change from Cartesian to Cylindrical.

The geometry is made; the next step is to make the mesh:

- In the “Mesh” window select Physics-controlled mesh and in “element size” choose Coarser.
- Click “Build All”.

Setting COMSOL to calculate the effective mode area:

- In “Component 1 - Definitions” right click and choose “Nonlocal Couplings” and “Integration”.
- In this window got to “Selection” and choose All domains.
- Right click again in “Component 1 - Definitions” and choose “Variables 1” to create a variable associated with the effective modal area.
- Put the following formula: intop1(abs(Ez)^2)^2 / intop1(abs(Ez)^4).

Now, to make the study:

- Right click in “Study 1” and choose “Parametric Sweep”.
- In the “Parametric Sweep” window click the “+” icon and below the “Parameter name” choose the variable associated with wavelength.
- Select the “Range” icon, put 1 as start, o.o5 as step and 1.95 as stop and click “Add”.
- Bellow “Parameter unit” change from m to um.
- In “Step 1 - Mode Analysis” in “Mode analysis frequency” change 1 to the name of your wavelength variable.
- In “Desired number of modes” put 150.
- In “Search for modes around shift” put 1.4443.
- Click the “Compute” button.

The simulation starts to obtain the calculated values:

- Go to “Results - Derived Values” and right click.
- Choose “Global Evaluation”.
- In this window select the second solution (parametric sweep one).
- Bellow “Expression” put imag(ewfd.neff) and it should appear 1 bellow “Unit”.
- Then put the name of the effective modal area variable and it should appear m^2 bellow “Unit”

# References

[1] Sabri, N., Aljunid, S. A., Salim, M. S., & Fouad, S. (2015). Fiber optic sensors: Short review and applications. In F. L. Gaol, K. Shrivastava, & J. Akhtar (Eds.), *Recent trends in physics of material science and technology* (pp. 299–311). Springer Singapore. https://doi.org/10.1007/978-981-287-128-2_19

[2] Ghatak, A., & Thyagarajan, K. (1998). *An introduction to fiber optics*. Cambridge University Press. https://books.google.pt/books?id=pG34VZMiI7IC

[3] Ujah, E., Lai, M., & Slaughter, G. (2023). Ultrasensitive tapered optical fiber refractive index glucose sensor. *Scientific Reports, 13*(1), 4495. https://doi.org/10.1038/s41598-023-31127-4

[4] Tazawa, H., Kanie, T., & Katayama, M. (2007). Fiber-optic coupler based refractive index sensor and its application to biosensing. *Applied Physics Letters, 91*(11). https://doi.org/10.1063/1.2785137

[5] Homola, J. (2008). Surface plasmon resonance sensors for detection of chemical and biological species. *Chemical Reviews, 108*(2), 462–493. https://doi.org/10.1021/cr068107d

[6] Bohren, C., & Huffman, D. (2008). *Absorption and scattering of light by small particles*. Wiley. https://books.google.pt/books?id=ib3EMXXIRXUC

[7] Kneipp, K., Kneipp, H., Itzkan, I., Dasari, R. R., & Feld, M. S. (1999). Ultrasensitive chemical analysis by Raman spectroscopy. *Chemical Reviews, 99*(10), 2957–2976. https://doi.org/10.1021/cr980133r

[8] Kryukov, A., Levashov, V., & Sazhin, S. (2004). Evaporation of diesel fuel droplets: Kinetic versus hydrodynamic models. *International Journal of Heat and Mass Transfer, 47*(12), 2541–2549. https://doi.org/10.1016/j.ijheatmasstransfer.2004.01.004

[9] Soltman, D., & Subramanian, V. (2008). Inkjet-printed line morphologies and temperature control of the coffee ring effect. *Langmuir, 24*(5), 2224–2231. https://doi.org/10.1021/la7026847

[10] Park, J., & Moon, J. (2006). Control of colloidal particle deposit patterns within picoliter droplets ejected by ink-jet printing. *Langmuir, 22*(8), 3506–3513. https://doi.org/10.1021/la053450j

[11] Dugas, V., Broutin, J., & Souteyrand, E. (2005). Droplet evaporation study applied to DNA chip manufacturing. *Langmuir, 21*(20), 9130–9136. https://doi.org/10.1021/la050764y

[12] Hari Govindha, A., Katre, P., Balusamy, S., Banerjee, S., & Sahu, K. C.

(2022). Counter-intuitive evaporation in nanofluids droplets due to stick-slip nature. *Langmuir, 38*(49), 15361–15371. https://doi.org/10.1021/acs.langmuir.2c02590

[13] Deegan, R. D., Bakajin, O., Dupont, T. F., Huber, G., Nagel, S. R., & Witten, T. A. (1997). Capillary flow as the cause of ring stains from dried liquid drops. *Nature, 389*(6653), 827–829. https://doi.org/10.1038/39827

[14] Balusamy, S., Banerjee, S., & Sahu, K. C. (2024). Intricate evaporation dynamics in different multi-droplet configurations. *arXiv preprint arXiv:2408.06649*. https://doi.org/10.48550/arXiv.2408.06649

[15] Euclid, Optics.

[16] al-Farisi, K. al-D. H. ibn A. ibn H. (1309). *Al-Basa'ir fi 'ilm al-Manazir*.

[17] Theodoric of Freiberg. (ca. 1304). *De iride et radialibus impressionibus*

[18] Babinet, J. (1842). Note on the transmission of light by sinuous canals. *Comptes Rendus de l'Académie des Sciences, 15*, 802

[19] Colladon, D. (1842). On the reflections of a ray of light inside a parabolic liquid stream. *Comptes Rendus de l'Académie des Sciences, 15*, 800.

[20] Tyndall, J. (1854). On some phenomena connected with the motion of liquids. *Proceedings of the Royal Institution, 1*, 446–448

[21] Wheeler, W. (1881, September 20). *Apparatus for lighting dwellings or other structures.* https://shorturl.at/KuYxD

[22] Ballato, J., & Dragic, P. (2016). Glass: The carrier of light–A brief history of optical fiber. *International Journal of Applied Glass Science, 7*(4), 413–422. https://doi.org/10.1111/ijag.12239

[23] Stolen, R., Bjorkholm, J., & Ahkin, A. (1974). Phase-matched three-wave mixing in silica fiber optical waveguides. *Applied Physics Letters, 24*, 308–310. https://doi.org/10.1063/1.1655195

[24] Stone, C. B. J. (1973). Neodymium-doped silica lasers in end-pumped fiber geometry. *Applied Physics Letters, 23*(7), 388–389. https://doi.org/10.1063/1.1654929

[25] Hill, K. O., Johnson, D. C., Kawasaki, B. S., & MacDonald, R. I. (1978). cw three-wave mixing in single-mode optical fibers. *Journal of Applied Physics, 49*(10), 5098–5106. https://doi.org/10.1063/1.324456

[26] Ramaswamy, V., Kaminow, I. P., Kaiser, P., & French, W. G. (1978). Single polarization optical fibers: Exposed cladding technique. *Applied Physics Letters, 33*(9), 814–816. https://doi.org/10.1063/1.90538

[27] Hill, K. O., Fujii, Y., Johnson, D. C., & Kawasaki, B. S. (1978). Photosensitivity

in optical fiber waveguides: Application to reflection filter fabrication. *Applied Physics Letters, 32*(10), 647–649. https://doi.org/10.1063/1.89881

[28] Meltz, G., Morey, W. W., & Glenn, W. H. (1989). Formation of Bragg gratings in optical fibers by a transverse holographic method. *Optics Letters, 14*(15), 823–825. https://doi.org/10.1364/OL.14.000823

[29] Birks, T., Roberts, P., Russell, P., Atkin, D., & Shepherd, T. (1995). Full 2-D photonic bandgaps in silica/air structures. *Electronics Letters, 31*(22), 1941–1943. https://doi.org/10.1049/el:19951306

[30] Cregan, R. F., Mangan, B. J., Knight, J. C., Birks, T. A., Russell, P. S. J., Roberts, P. J., & Allan, D. C. (1999). Single-mode photonic band gap guidance of light in air. *Science, 285*(5433), 1537–1539. https://doi.org/10.1126/science.285.5433.1537

[31] Knight, J. C., Birks, T. A., Russell, P. S. J., & Atkin, D. M. (1996). All-silica single-mode optical fiber with photonic crystal cladding. *Optics Letters, 21*(19), 1547–1549. https://doi.org/10.1364/OL.21.001547

[32] Ranka, J. K., Windeler, R. S., & Stentz, A. J. (2000). Visible continuum generation in air–silica microstructure optical fibers with anomalous dispersion at 800 nm. *Optics Letters, 25*(1), 25–27. https://doi.org/10.1364/OL.25.000025

[33] Martin, L. (2014). *Lockheed Martin demonstrates 30 kW weapons-grade fiber laser*. https://shorturl.at/LxC5k

[34] National Research Council. (2013). *Optics and photonics: Essential technologies for our nation*. National Academies Press. https://shorturl.at/Lpag8

[35] Keiser, G. (2010). *Optical fiber communications*. McGraw-Hill. https://books.google.pt/books?id=T8UgkgAACAAJ

[36] Kostovski, G., Stoddart, P. R., & Mitchell, A. (2014). The optical fiber tip: An inherently light-coupled microscopic platform for micro- and nanotechnologies. *Advanced Materials, 26*(23), 3798–3820. https://doi.org/10.1002/adma.201304605

[37] Paiva, J. S., Jorge, P. A., Rosa, C. C., & Cunha, J. P. (2018). Optical fiber tips for biological applications: From light confinement, biosensing to bioparticles manipulation. *Biochimica et Biophysica Acta (BBA) - General Subjects, 1862*(5), 1209–1246. https://doi.org/10.1016/j.bbagen.2018.02.008

[38] Vaiano, P., Consales, M., Ricciardi, A., Crescitelli, A., Esposito, A., Cusano, A., & Cutolo, A. (2016). Lab on fiber technology for biological sensing applications. *Laser & Photonics Reviews, 10*(6), 922–961.

https://doi.org/10.1002/lpor.201600111

[39] Smartoptics. (2022). *What is an optical fiber?* https://smartoptics.com/knowledgebank-post/what-is-an-optical-fiber

[40] GOPhotonics. (2022). *What is the numerical aperture of an optical fiber*. What is the Numerical Aperture (NA) of an Optical Fiber? - GoPhotonics.com

[41] Thorlabs. (2025). *NewGroupPage9 – Object Group 949*. https://www.thorlabs.com/newgrouppage9.cfm?objectgroup_id=949

[42] Thorlabs. (2025). *Object Group 362*. https://www.thorlabs.com/newgrouppage9.cfm?objectgroup_id=362

[43] Thorlabs. (2025). *Thorlabs catalog page 1100*. https://www.thorlabs.com/catalogPages/1100.pdf

[44] Zhang, T., Zheng, Y., Wang, C., Zhengming, M., Liu, Y., & Lin, J. (2017). A review of photonic crystal fiber sensor applications for different physical quantities. *Applied Spectroscopy Reviews, 53*, Article e1376681. https://doi.org/10.1080/05704928.2017.1376681

[45] Javaid, M., Haleem, A., Rab, S., Pratap Singh, R., & Suman, R. (2021). Sensors for daily life: A review. *Sensors International, 2*, 100121. https://doi.org/10.1016/j.sintl.2021.100121

[46] Monolithic Power Systems. (2024). *Sensor output types*. https://www.monolithicpower.com/en/learning/mpscholar/sensors/basics-of-sensor-operation/sensor-output-types

[47] Eid, M. M. A. (2022). Optical fiber sensors: Review of technology and applications. *Indonesian Journal of Electrical Engineering and Computer Science, 25*(2), 1038–1046. https://doi.org/10.11591/ijeecs.v25.i2.pp1038-1046

[48] Radhakrishnan, R., Suni, I. I., Bever, C. S., & Hammock, B. D. (2014). Impedance biosensors: Applications to sustainability and remaining technical challenges. *ACS Sustainable Chemistry & Engineering, 2*(7), 1649–1655. https://doi.org/10.1021/sc500106y

[49] Bharti, K., & Sadhu, K. K. (2022). Syntheses of metal oxide-gold nanocomposites for biological applications. *Results in Chemistry, 4*, 100288. https://doi.org/10.1016/j.rechem.2022.100288

[50] Mohammad-Rezaei, R., & Golmohammadpour, M. (2020). Controlled electrodeposition of Au-copper oxide nanocomposite on a renewable carbon ceramic electrode for sensitive determination of NADH in serum samples. *Electroanalysis, 32*(3), 606–612. https://doi.org/10.1002/elan.201900592

[51] Pérez-Ràfols, C., Serrano, N., Díaz-Cruz, J. M., Ariño, C., & Esteban, M. (2017). A chemically-bound glutathione sensor bioinspired by the defense of organisms against heavy metal contamination: Optimization of the immobilization conditions. *Chemosensors, 5*(2), Article 12. https://doi.org/10.3390/chemosensors5020012

[52] Kazuma, E., & Tatsuma, T. (2014). Localized surface plasmon resonance sensors based on wavelength-tunable spectral dips. *Nanoscale, 6*(4), 2397–2405. https://doi.org/10.1039/C3NR05846H

[53] Zhang, F., Li, B., Zhang, X., Guo, P., Guo, L., & Gong, X. (2024). A highly sensitive fiber tip temperature sensor based on enhanced Fresnel reflection induced by modified materials. *Ceramics International, 50*. https://doi.org/10.1016/j.ceramint.2024.02.131

[54] Ma, J., Zhou, Y., Bai, X., Chen, K., & Guan, B.-O. (2019). High-sensitivity and fast response fiber-tip Fabry-Pérot hydrogen sensor with suspended palladium-decorated graphene. *Royal Society of Chemistry*. https://doi.org/10.1039/C9NR04274A

[55] Wu, L., Zhang, Y., Wang, Y., Li, Y., Liu, Y., & Zhang, H. (2023). MXene sensors based on optical and electrical sensing signals: From biological, chemical, and physical sensing to emerging intelligent and bionic devices. *PhotoniX, 4*(1), Article 15. https://doi.org/10.1186/s43074-023-00091-7

[56] Yadav, P. K., & Srivastava, R. (2018). Optical fiber sensor: Review and applications. *Semantic Scholar*. https://api.semanticscholar.org/CorpusID:244101774

[57] Zhang, Y., Xue, L., Wang, T., Yang, L., Zhu, B., & Zhang, Q. (2013). High performance temperature sensing of single mode-multimode-single mode fiber with thermos-optic polymer as cladding of multimode fiber segment. *IEEE Sensors Journal, 14*(4), 1143–1147. 10.1109/JSEN.2013.2293536

[58] Tian, K., Zhang, Y., Liu, B., Wang, Y., Li, J., & Zhao, Y. (2017). A curvature sensor based on twisted single-mode–multimode single-mode hybrid optical fiber structure. *Journal of Lightwave Technology, 35*(9), 1725–1731. https://opg.optica.org/jlt/abstract.cfm?URI=jlt-35-9-1725

[59] Wang, P., Liu, B., Tian, K., Zhang, Y., Li, J., & Zhao, Y. (2019). Temperature-insensitive refractometer based on an RI-modulated singlemode-multimode-singlemode fibre structure. *Optics Express, 27*(10), 13754–13764. https://doi.org/10.1364/OE.27.013754

[60] Hou, Y.-F., Li, J., Fan, R., Yang, J., & Zhang, X. (2020). Simultaneous

measurement of pressure and temperature in seawater with PDMS sealed microfiber Mach–Zehnder interferometer. *Journal of Lightwave Technology, 38*(22), 6412–6421. https://doi.org/10.1109/JLT.2020.3012716

[61] Wu, Y., Zhang, Y., Liu, B., Tian, K., Li, J., & Zhao, Y. (2018). Highly sensitive force sensor based on balloon-like interferometer. *Optics & Laser Technology, 103*, 17–21. https://doi.org/10.1016/j.optlastec.2018.01.008

[62] Zhou, X., Li, X., Li, S., An, G.-W., & Cheng, T. (2018). Magnetic field sensing based on SPR optical fiber sensor interacting with magnetic fluid. *IEEE Transactions on Instrumentation and Measurement, 68*(1), 234–239. 10.1109/TIM.2018.2834222

[63] Yang, X., Zhang, Y., Liu, B., Tian, K., Li, J., & Zhao, Y. (2015). Textile fiber optic microbend sensor used for heartbeat and respiration monitoring. *IEEE Sensors Journal, 15*(2), 757–761. https://doi.org/10.1109/JSEN.2014.2353640

[64] Lee, B. H., Kim, Y., Kim, J., Jeong, Y., & Her, S. (2012). Interferometric fiber optic sensors. *Sensors, 12*(3), 2467–2486. https://doi.org/10.3390/s120302467

[65] Li, J. (2020). A review: Development of novel fiber-optic platforms for bulk and surface refractive index sensing applications. *Sensors and Actuators Reports, 2*(1), 100018. https://doi.org/10.1016/j.snr.2020.100018

[66] Elsherif, M., Moreddu, R., Hassan, M. U., Yetisen, A. K., & Butt, H. (2022). Optical fiber sensors: Working principle, applications, and limitations. *Advanced Photonics Research, 3*(11), 2100371. https://doi.org/10.1002/adpr.202100371

[67] Brientin, A., Leduc, D., Gaillard, V., Girard, M., & Lupi, C. (2021). Numerical and experimental study of a multimode optical fiber sensor based on Fresnel reflection at the fiber tip for refractive index measurement. *Optics & Laser Technology, 143*, 107315. https://doi.org/10.1016/j.optlastec.2021.107315

[68] Zibaii, M. I., Kazemi, A., Latifi, H., Azar, M. K., Hosseini, S. M., & Ghezelaiagh, M. H. (2010). Measuring bacterial growth by refractive index tapered fiber optic biosensor. *Journal of Photochemistry and Photobiology B: Biology, 101*(3), 313–320. 10.1016/j.jphotobiol.2010.07.017

[69] Mansor, M., Harun, S. W., Ahmad, H., Nor, R. M., & Shabaneh, A. (2020). Taper biosensor in fiber ring laser cavity for protein detection. *Optics & Laser Technology, 125*, 106033. https://doi.org/10.1016/j.optlastec.2019.106033

[70] Stewart, W. (Ed.). (1985). IOOC-ECOC '85: 5th International Conference on Integrated Optics and Optical Fibre Communication; 11th European

Conference on Optical Communication: Venezia, Italy, October 1–4, 1985: Technical Digest. Genova, Italy: Istituto Internazionale Delle Communicazioni. IOOC-ECOC '85 : 5th International Conference on Integrated Optics and Optical Fibre Communication : 11th European Conference on Optical Communication : Venezia, Italy, October 1-4, 1985 : technical digest | WorldCat.org

[71] Kashyap, R. (2009). *Fiber Bragg gratings*. Academic Press. https://books.google.pt/books?id=qTWe5aHi8doC

[72] Kreuzer, M. (2006). *Strain measurement with fiber Bragg grating sensors* (Vol. 12, S2338-1.0 e). HBM. https://shorturl.at/9vxhZ

[73] James, S. W., & Tatam, R. P. (2003). Optical fibre long-period grating sensors: Characteristics and application. *Measurement Science and Technology, 14*(5), R49. 10.1088/0957-0233/14/5/201:

[74] Hira, U., & Ahmad, M. N. (2024). Optical fiber sensors. In S. W. Harun (Ed.), *Optical technologies for advancing communication, sensing, and computing systems* (Chap. 3). IntechOpen. https://doi.org/10.5772/intechopen.1007081

[75] Lee, B.-H., Eom, J.-B., Park, K.-S., Park, S.-J., & Ju, M.-J. (2010). Specialty fiber coupler: Fabrications and applications. *Journal of the Optical Society of Korea, 14*(4), 326–332. https://doi.org/10.3807/JOSK.2010.14.4.326

[76] Grattan, K. T., & Meggitt, B. T. (1995). *Optical fiber sensor technology* (Vol.1) https://shorturl.at/U9GBY

[77] Sirkis, J., Brennan, D., Putman, M., Berkoff, T., Kersey, A., & Friebele, E. (1993). In-line fiber etalon for strain measurement. *Optics Letters, 18*(22), 1973–1975. https://doi.org/10.1364/OL.18.001973

[78] Tsai, W.-H., & Lin, C.-J. (2001). A novel structure for the intrinsic Fabry–Perot fiber-optic temperature sensor. *Journal of Lightwave Technology, 19*(5), 682–686. 10.1109/50.923481

[79] Koo, K., LeBlanc, M., Tsai, T., & Vohra, S. (2002). Fiber-chirped grating Fabry–Perot sensor with multiple-wavelength-addressable free-spectral ranges. *IEEE Photonics Technology Letters, 10*(7), 1006–1008.

[80] Santos, J. S., Raimundo Jr, I. M., Cordeiro, C. M., Biazoli, C. R., Gouveia, C. A., & Jorge, P. A. (2014). Characterisation of a Nafion film by optical fibre Fabry–Perot interferometry for humidity sensing. *Sensors and Actuators B: Chemical, 196*, 99–105. https://doi.org/10.1016/j.snb.2014.01.101

[81] Wang, J.-N., & Tang, J.-L. (2012). Photonic crystal fiber Mach–Zehnder interferometer for refractive index sensing. *Sensors, 12*(3), 2983–2995.

https://doi.org/10.3390/s120302983

[82] Fu, H., Zhang, Y., Liu, B., Tian, K., Li, J., & Zhao, Y. (2008). Pressure sensor realized with polarization-maintaining photonic crystal fiber-based Sagnac interferometer. *Applied Optics, 47*(15), 2835–2839. https://doi.org/10.1364/AO.47.002835

[83] Caucheteur, C., Guo, T., & Albert, J. (2015). Review of plasmonic fiber optic biochemical sensors: Improving the limit of detection. *Analytical and Bioanalytical Chemistry, 407*(14), 3883–3897. 10.1007/s00216-014-8411-6

[84] Li, J. (2020). A review: Development of novel fiber-optic platforms for bulk and surface refractive index sensing applications. *Sensors and Actuators Reports, 2*(1), 100018. https://doi.org/10.1016/j.snr.2020.100018

[85] Yu, H., Zhang, Y., Liu, B., Tian, K., Li, J., & Zhao, Y. (2014). Solution concentration and refractive index sensing based on polymer microfiber knot resonator. *Applied Physics Express, 7*(2), 022501. 10.7567/APEX.7.022501

[86] Zhang, W., Tuerdahong, N., Zhu, L., Dong, M., & Lou, X. (2019). Temperature and refractive index measurement using an optical fiber sensor featuring PCF-FP and FBG inscribed by femtosecond laser. *Optik, 194*, 163095. https://doi.org/10.1016/j.ijleo.2019.163095

[87] Tsai, C.-W., & Yu, C.-P. (2019). Highly sensitive Fabry–Pérot refractive index sensor by using a polished pyramidal fiber. In *2019 24th OptoElectronics and Communications Conference (OECC) and 2019 International Conference on Photonics in Switching and Computing (PSC)* (pp. 1–3). IEEE. https://doi.org/10.23919/PS.2019.8818149

[88] Alonso-Murias, M. d. C., Velázquez-González, J. S., & Monzón-Hernández, D. (2019). SPR fiber tip sensor for the simultaneous measurement of refractive index, temperature, and level of a liquid. *Journal of Lightwave Technology, 37*(18), 4808–4814. https://doi.org/10.1109/JLT.2019.2921302

[89] Tai, Y.-H., Tsai, P.-C., Ho, Y.-L., Delaunay, J.-J., & Wei, P.-K. (2019). Combination of an axicon fiber tip and a camera device into a sensitive refractive index sensor. *Sensors, 19*(22), 4911. https://doi.org/10.3390/s19224911

[90] Yang, H., Li, Y., & Li, X. (2022). Intensity-modulated refractive index sensor based on the side modes of fiber Bragg grating. *Optics Communications, 505*, 127319. https://doi.org/10.1016/j.optcom.2021.127319

[91] Jain, S., Choudhary, K., & Kumar, S. (2022). Photonic crystal fiber-based

SPR sensor for broad range of refractive index sensing applications. *Optical Fiber Technology, 73*, 103030. https://doi.org/10.1016/j.yofte.2022.103030

[92] Andres, A. C., Barroso, J., Martín-Palma, R. J., García, I., Zubia, J., & Arrizabalaga, O. (2022). Biosensing platform on optical fibre tip for lysozyme detection. In M. T. Canva, A. Giannetti, H. Altug, & J. Moreau (Eds.), *Biophotonics in Point-of-Care II* (p. 1214506). SPIE. https://doi.org/10.1117/12.2620647

[93] Meng, Y.-Q., Dong, X., Xie, Y.-H., Wu, C., Li, J., & Guan, B.-O. (2022). Fiber-tip refractive index sensor based on Bragg grating written in an exposed-core side-hole fiber. In *Proceedings of the Asia Communications and Photonics Conference (ACP)* (pp. 340–342). IEEE. https://doi.org/10.1109/ACP55869.2022.10088473

[94] Patiño-Jurado, B., Gaviria-Calderón, A., Botero-Cadavid, J. F., & Garcia Sucerquia, J. (2023). Intensity-modulated refractive index sensor based on optical fiber with slanted end. *Optics & Laser Technology, 157*, 108700. http://dx.doi.org/10.2139/ssrn.4108004

[95] Zhu, C., & Huang, J. (2023). Multiplexed optical fiber tip refractive index sensor interrogated by microwave photonics. *Optics and Lasers in Engineering, 163*, 107477. https://doi.org/10.1016/j.optlaseng.2023.107477

[96] Soares, L., Cunha, C., Novais, S., Ferreira, A., Frazão, O., & Silva, S. (2023). Refractive index measurements of ethanol–water binary liquid solutions using a graded index fiber tip sensor. *IEEE Sensors Letters, 7*(9), 1–4. https://doi.org/10.1109/LSENS.2023.3303079

[97] Halendy, M., & Ertman, S. (2023). Whispering-gallery mode micro-ring resonator integrated with a single-core fiber tip for refractive index sensing. *Sensors, 23*(23), 9424. https://doi.org/10.3390/s23239424

[98] Huang, Y., Pu, X., Qian, H., & others. (2024). Optical fiber surface plasmon resonance sensor using electroless-plated gold film for thrombin detection. *Analytical and Bioanalytical Chemistry, 416*, 1469–1483. https://doi.org/10.1007/s00216-024-05150-x

[99] Preter, E., Donlagic, D., Artel, V., Katims, R. A., Sukenik, C. N., & Zadok, A. (2014). Analysis of organic solvents and liquid mixtures using a fiber-tip evaporation sensor. In J. M. López-Higuera, J. D. C. Jones, M. López-Amo, & J. L. Santos (Eds.), *Proceedings of the 23rd International Conference on Optical Fibre Sensors* (p. 91574). SPIE. https://doi.org/10.1117/12.2059371

[100] Innocenzi, P., Malfatti, L., Costacurta, S., Kidchob, T., Piccinini, M., & Marcelli,

A. (2008). Evaporation of ethanol and ethanol–water mixtures studied by time-resolved infrared spectroscopy. *The Journal of Physical Chemistry A, 112*(29), 6512–6516. https://doi.org/10.1021/jp7111395

[101] Kita, Y., et al. (2018). Quantifying vapor transfer into evaporating ethanol droplets in a humid atmosphere. *Physical Chemistry Chemical Physics, 20*, 19430–19440. https://doi.org/10.1039/C8CP02521E

[102] You, D.-W., Seon, Y.-S., Jang, Y., Bang, J., Oh, J.-S., & Jung, K.-W. (2020). A portable gas chromatograph for real-time monitoring of aromatic volatile organic compounds in air samples. *Journal of Chromatography A, 1625*, 461267. https://doi.org/10.1016/j.chroma.2020.461267

[103] Langford, V. S., Graves, I., & McEwan, M. J. (2014). Rapid monitoring of volatile organic compounds: A comparison between gas chromatography/mass spectrometry and selected ion flow tube mass spectrometry. *Rapid Communications in Mass Spectrometry, 28*(1), 10–18. https://doi.org/10.1002/rcm.6747

[104] Sefiane, K., Tadrist, L., & Douglas, M. (2003). Experimental study of evaporating water–ethanol mixture sessile drop: Influence of concentration. *International Journal of Heat and Mass Transfer, 46*(23), 4527–4534. https://doi.org/10.1016/S0017-9310(03)00267-9

[105] Brutin, D., & Starov, V. (2018). Recent advances in droplet wetting and evaporation. *Chemical Society Reviews, 47*, 558–585. https://doi.org/10.1039/C6CS00902F

[106] Liu, C., Bonaccurso, E., & Butt, H. J. (2008). Evaporation of sessile water–ethanol drops in a controlled environment. *Physical Chemistry Chemical Physics, 10*, 7150–7157. https://doi.org/10.1039/B808258H

[107] Khan, S., Le Calvé, S., & Newport, D. (2020). A review of optical interferometry techniques for VOC detection. *Sensors and Actuators A: Physical, 302*, 111782. https://doi.org/10.1016/j.sna.2019.111782

[108] Lim, O.-R., & Ahn, T.-J. (2019). Fiber-optic measurement of liquid evaporation dynamics using signal processing. *Journal of Lightwave Technology, 37*(19), 4967–4975. https://doi.org/10.1109/JLT.2019.2926480

[109] Gomes, A. D., et al. (2016). Acetone evaporation and water vapor detection using a caterpillar-like microstructured fiber. *Microwave and Optical Technology Letters, 58*(3), 679–683. https://doi.org/10.1002/mop.29644

[110] Silva, S. O., et al. (2014). Detection of evaporation process of acetone with a microstructured fiber in a reflective configuration. *Optical Engineering, 53*(8),

080501. https://doi.org/10.1117/1.OE.53.8.080501

[111] Moura, J. P., et al. (2014). Evaporation of volatile compounds in suspended-core fibers. *Optics Letters, 39*(13), 3868–3871. https://doi.org/10.1364/OL.39.003868

[112] Valves Instruments Plus Ltd. (n.d.). *Density of liquid water from 0°C to 100°C*. https://www.vip-ltd.co.uk/Expansion/Density_Of_Water_Tables.pdf

[113] Measurement Canada. (2016). *Volume correction factors—Isopropyl alcohol (anhydrous)*. https://ised-isde.canada.ca/site/measurementcanada/en/laws-and-requirements/volume-correction-factors-isopropyl-alcohol-anhydrous

[114] Abdelaziz, I., Ademgil, H., AbdelMalek, F., Haxha, S., Gorman, T., & Bouchriha, H. (2010). Design of a large effective mode area photonic crystal fiber with modified rings. *Optics Communications, 283*(24), 5218–5223. https://doi.org/10.1016/j.optcom.2010.08.005

[115] Rodrigues, S. M., Facão, M., & Ferreira, M. F. S. (2020). Modelling and simulation methods for microstructured optical fibers. *Fiber and Integrated Optics, 39*(5–6), 215–239. https://doi.org/10.1080/01468030.2020.1843203

[116] D. J. Griffiths, Introduction to electrodynamics. Pearson, 2014. https://books.google.pt/books?id=J9ygBwAAQBAJ

[117] COMSOL. (2025). *COMSOL – Software for multiphysics simulation*. https://www.comsol.com/

[118] Seshu, P. (2003). *Textbook of finite element analysis* (10th printing, January 2012). PHI Learning Private Limited. https://shorturl.at/SDXsm

[119] Hill, K. (1974). Aperiodic distributed-parameter waveguides for integrated optics. *Applied Optics, 13*(8), 1853–1856. https://doi.org/10.1364/AO.13.001853

[120] Braunfelds, J., Senkans, U., Skels, P., Janeliukstis, R., Salgals, T., Redka, D., Lyashuk, I., Porins, J., Spolitis, S., Haritonovs, V., et al. (2021). FBG-based sensing for structural health monitoring of road infrastructure. *Journal of Sensors, 2021*(1), 8850368. https://doi.org/10.1155/2021/8850368

[121] Rovera, A., Tancau, A., Boetti, N., Dalla Vedova, M. D. L., Maggiore, P., & Janner, D. (2023). Fiber optic sensors for harsh and high radiation environments in aerospace applications. *Sensors, 23*(5), 2512. https://doi.org/10.3390/s23052512

[122] Lo Presti, D., Cimini, S., Massaroni, C., D'Amato, R., Caponero, M. A., De Gara, L., & Schena, E. (2021). Plant wearable sensors based on FBG technology for growth and microclimate monitoring. *Sensors, 21*(19), 6327.

https://doi.org/10.3390/s21196327

[123] Riza, M. A., Go, Y. I., Harun, S. W., & Maier, R. R. (2020). FBG sensors for environmental and biochemical applications—A review. *IEEE Sensors Journal, 20*(14), 7614–7627. 10.1109/JSEN.2020.2982446

[124] Rodrigues, C., Félix, C., Lage, A., & Figueiras, J. (2010). Development of a long-term monitoring system based on FBG sensors applied to concrete bridges. *Engineering Structures, 32*(8), 1993–2002. https://doi.org/10.1016/j.engstruct.2010.03.016

[125] Dalla Vedova, M. D. L., Berri, P. C., Maggiore, P., & Quattrocchi, G. (2020). *Design and development of innovative FBG-based fiber optic sensors for aerospace applications*. In *Journal of Physics: Conference Series* (Vol.. https://doi.org/10.1088/1742-6596/1589/1/012012

[126] Santos, J. L., & Farahi, F. (Eds.). (2014). *Handbook of optical sensors* (1st ed.). CRC Press. https://doi.org/10.1201/b17641

[127] Liu, H.-L., Zhu, Z.-W., Zheng, Y., Liu, B., & Xiao, F. (2018). Experimental study on an FBG strain sensor. *Optical Fiber Technology, 40*, 144–151. https://doi.org/10.1016/j.yofte.2017.09.003

[128] Othonos, A. (1997). Fiber Bragg gratings. *Review of Scientific Instruments, 68*(12), 4309–4341. https://doi.org/10.1063/1.1148382

[129] Robalinho, P., Piaia, V., Soares, L., Novais, S., Ribeiro, A. L., Silva, S., & Frazão, O. (2024). Phase-shifted fiber Bragg grating by selective pitch slicing. *Sensors, 24*(21), 6898. https://doi.org/10.3390/s24216898

[130] French, A. P. (1971). Vibrations and waves. In The M.I.T. Introductory Physics Series. W. W. Norton & Company. https://books.google.pt/books?id=RqE26vDmd5wC

[131] Fano, U. (1935). Sullo spettro di assorbimento dei gas nobili presso il limite dello spettro d'arco. *Il Nuovo Cimento, 12*(3), 154–161. https://doi.org/10.1007/BF02958288

[132] Fano, U. (1961). Effects of configuration interaction on intensities and phase shifts. *Physical Review, 124*(6), 1866–1878. https://doi.org/10.1103/PhysRev.124.1866

[133] Limonov, M. F., Rybin, M. V., Poddubny, A. N., & Kivshar, Y. S. (2017). Fano resonances in photonics. *Nature Photonics, 11*(9), 543–554. https://doi.org/10.1038/nphoton.2017.142

[134] Connerade, J. P., & Lane, A. M. (1988). Interacting resonances in atomic spectroscopy. *Reports on Progress in Physics, 51*(11), 1439–1478.

https://doi.org/10.1088/0034-4885/51/11/002

[135] Bekele, D., Yu, Y., Yvind, K., & Mork, J. (2019). In-plane photonic crystal devices using Fano resonances. *Laser & Photonics Reviews, 13*(12), Article 1900054. https://doi.org/10.1002/lpor.201900054